Effect of Rolling Induced Anisotropy on Fatigue Crack Initiation and Short Crack Propagation in Al 2024-T351

by

Admir Makaš

A Thesis Presented in Partial Fulfillment
of the Requirements for the Degree
Master of Science

Approved June 2011 by the
Graduate Supervisory Committee:

Pedro Peralta, Chair
Karl Sieradzki
Joseph Davidson

ARIZONA STATE UNIVERSITY

August 2011

ABSTRACT

A full understanding of material behavior is important for the prediction of residual useful life of aerospace structures via computational modeling. In particular, the influence of rolling-induced anisotropy on fatigue properties has not been studied extensively and it is likely to have a meaningful effect. In this work, fatigue behavior of a wrought Al alloy (2024-T351) is studied using notched uniaxial samples with load axes along either the longitudinal or transverse direction, and center notched biaxial samples (cruciforms) with a uniaxial stress state of equivalent amplitude about the bore. Local composition and crystallography were quantified before testing using Energy Dispersive Spectroscopy and Electron Backscattering Diffraction. Interrupted fatigue testing at stresses close to yielding was performed on the samples to nucleate and propagate short cracks and nucleation sites were located and characterized using standard optical and Scanning Electron Microscopy.

Results show that crack nucleation occurred due to fractured particles for longitudinal dogbone/cruciform samples; while transverse samples nucleated cracks by debonded and fractured particles. Change in crack nucleation mechanism is attributed to dimensional change of particles with respect to the material axes caused by global anisotropy. Crack nucleation from debonding reduced life till matrix fracture because debonded particles are sharper and generate matrix cracks sooner than their fractured counterparts. Longitudinal samples experienced multisite

crack initiation because of reduced cross sectional areas of particles parallel to the loading direction. Conversely the favorable orientation of particles in transverse samples reduced instances of particle fracture eliminating multisite cracking and leading to increased fatigue life. Cyclic tests of cruciform samples showed that crack growth favors longitudinal and transverse directions with few instances of crack growth 45 degrees (diagonal) to the rolling direction. The diagonal crack growth is attributed to stronger influences of local anisotropy on crack nucleation. It was observed that majority of the time crack nucleation is governed by the mixed influences of global and local anisotropies.

Measurements of crystal directions parallel to the load on main crack paths revealed directions clustered near the {110} planes and high index directions. This trend is attributed to environmental effects as a result of cyclic testing in air.

DEDICATION

I would like to especially dedicate this publication to my wife and love of my life Christi Makaš for the love, support and understanding given throughout the arduous course of graduate school.

I would also like to dedicate this report to my parents Nedžad and Ferida Makaš for they have sacrificed much so that I can enjoy the liberties of following my passions and dreams.

ACKNOWLEDGMENTS

I would first and foremost like to thank my advisor, Dr. Pedro Peralta for all the advice and guidance given throughout the duration of this study and for helping me further my knowledge in the broad fields of solid mechanics and material science. I would also like to thank the members of my committee for all their advice and comments.

I would like to thank the three undergraduate students Jackie Avallone, Ross MacKinnon and Ikshwaku Itodaria for helping me prepare and test samples. Special thanks to Dr. Dallas Kingsbury for help and guidance in the use of the uniaxial and biaxial servo-hydraulic frames.

I would like to thank Mr. Martin Johnson and Mr. Dennis Golabiewski for fabrication of all the samples and tools needed for this project.

Lastly I would like to thank Mr. Sisouk “Si” Phrasavath and Dr. Zhenquan Liu at the Center for High Resolution Electron Microscopy at Arizona State University for useful guide and use of their electron microscopes.

This research was supported by the Department of Defense (DoD) MURI Air Force Office of Scientific Research Grant Number FA95550-06-1-0309, Program Manager Dr. Davis Stargel.

TABLE OF CONTENTS

Page

LIST OF TABLES

LIST OF FIGURES

CHAPTER 1

INTRODUCTION

Study herein pertains to the understanding of fatigue behavior in rolled Al 2024-T351 plate. Due to the rolling step during material procurement the material microstructure and second phase particles are elongated and flattened in different material directions. Figure 1.1 shows a typical grain structure in rolled aluminum plates along with material directions defined.

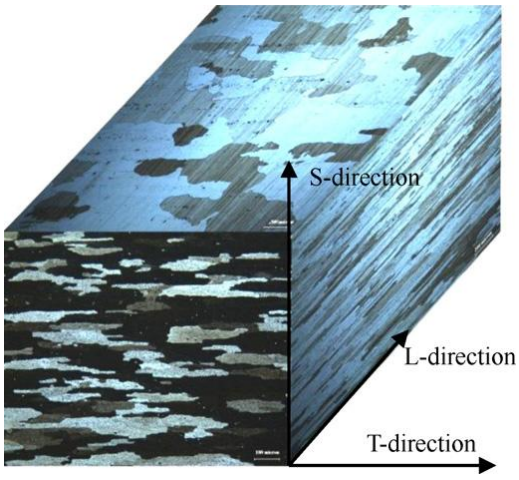

Figure 1.1: Typical grain structure of rolled aluminum plates (Zheng et.al., 2011).

In the figure, L, T and S correspond to longitudinal, transverse and short directions, respectively. The grains and second phase particles are elongated along the L direction and flattened in the S direction. Because of the rolling, material becomes anisotropic, possessing different mechanical properties in each of the material directions. The rolling induced anisotropy also affects the fatigue properties of the alloy and the

goal of the research presented here is to study the effects of anisotropy on fatigue performance in the L and T directions.

Until about the mid 1960's most of the research related to fatigue was concerned with studies of pure one-phase metals such as aluminum and copper and their solid solutions. For these cases, it was discovered that fatigue cracks originated from persistent slip bands (PSB) that were formed by continuous irreversible slip caused by cyclic loading (Suresh, 1998, Li, 2006, Choi, 2005). Initially similar beliefs were held for commercially available metal alloys that contained a large variety of trace elements as well as one or more secondary phases. In one of the earliest studies, Grosskreutz and Shaw compared early fatigue properties of high purity (1100-0) and commercially pure aluminum (2024-T4) alloys. The study was performed under the assumption that both alloys would have comparable crack initiation mechanisms. However, to the researchers' surprise the commercially available aluminum alloy showed no instance of fatigue crack nucleation due to PSB's. Rather the nucleation sites originated from constituent particles formed by the trace elements present in the alloy (Grosskreutz and Shaw, 1965). Since that time numerous studies have been performed on commercially available aluminum alloys. Numerous crack nucleation phenomena have been observed, mostly originating at or near the constituent particles. While the majority of studies pointed to fractured particles as the nucleating sites of fatigue cracks (Bowles and Schijve, 1973; Pearson, 1975; Tanaka and Mura,

1982; Akiniwa and Tanaka, 1988, Payne et. al., 2010), others reported crack initiation to take place due to debonded particles and dislocation pile-ups on the inclusion matrix interface (Grosskreutz and Shaw, 1965; Grosskreutz and Shaw, 1968, Tanaka and Mura, 1982; Kung and Fine, 1979).

Most of these early studies did not take into account effects of material anisotropy due to rolling on the fatigue performance. Eventually a limited number of studies were performed with the intention of studying the effects of anisotropy on the crack nucleation and initial propagation regimes. A study performed by Morris and coworkers first suggested that material anisotropy significantly affects alloy fatigue performance (Morris et. al., 1976). Since that time additional studies were performed on anisotropy effects on fatigue properties (Zabett and Plumtree, 1995; DeBartolo and Hillberry, 1998; Zhai, 2006). They all concluded that anisotropy of the rolled alloys impacts fatigue performance in either deleterious or positive manner.

In the present time numerous attempts have been made to model fatigue response of rolled aluminum alloys based on stochastic methodologies. However, most of the research performed is concerned with only the rolling direction of the material (Magnusen et. al., 1997; Laz and Hillberry, 1997; Maymon, 2004). While some studies have measured particle properties in all three planes of the rolled aluminum plate, no actual cyclic testing in other material directions (besides the rolling

direction) seems to have been performed (Brockenbrough et. al., 1993; Liao et. al., 2008; Liao, 2009). The underlying assumption seems to be that crack nucleation properties will be equivalent in all planes and that only the statistical distribution of particle dimensions is necessary to fully evaluate the crack nucleation and early propagation properties. It will be seen throughout this report that mechanisms of crack nucleation are also affected by the overall and local anisotropies and not only the particle shape and size distributions.

The work presented here will describe experimental work on uniaxial and biaxial samples performed to elucidate fatigue properties of Al 2024-T351 in longitudinal (L) and transverse (TL) directions, with emphasis on the effects of overall anisotropy induced by rolling and local anisotropy produced by crystal orientation of individual grains on crack nucleation. Fatigue tests shall be carried out on uniaxial samples in L and TL directions and compared to the particle and grain morphology in the subject material orientations in order to shed more light on the interactions between particles and matrix. With the use of biaxial (cruciforms) samples, the roles and interactions of local (individual grain orientations) and global (sheet rolling step) anisotropies will be explored by the use of a bore in the middle of the sample. The uniaxial stress state about the bore will be of equal amplitude allowing for probing of weakest crystal directions and the impact of global anisotropy on crack nucleating locations

CHAPTER 2

LITERATURE REVIEW

Fatigue plays an important role in design, implementation and evaluation of many engineering structures. The process of fatigue can be divided into two stages, crack nucleation and crack propagation (Grosskreutz and Shaw, 1965; Li, 2006). The crack nucleation stage depends on the alloy under study and can be caused by either persistent slip bands (PSB's) for pure metals or inclusions for commercial aluminum alloys (Li, 2006). The crack propagation regime can be classified into 3 classes; short cracks, physically short cracks and long cracks (Suresh, 1998, Lankford 1982; Lankford 1985; Xue et. al., 2007). Short fatigue cracks are considered "small" with respect to some microstructural length scale such as the grain size. Physically short cracks are considered small when their sizes range 0.5-1.0 mm or are small with respect to the plastic zone encompassing the crack tip. Finally, long cracks are such that the plastic zone ahead of the crack tip is small compared to the crack size; moreover, long cracks cease to grow along preferential crystallographic planes, which is one of the main properties of short fatigue cracks. (Suresh, 1998; Li, 2006; Lankford, 1982; Lankford 1985; Newman and Edwards, 1988; Xue et. al., 2007). Work presented here will deal predominantly with the crack initiation and propagation of short fatigue cracks and further elaboration shall be carried out on the crack nucleation and propagation phenomena in the subsequent sections. The study of

short crack nucleation and propagation behavior is of significant importance in the aerospace industry. In this industry, unremitting weight saving initiatives, aimed at reducing operating costs, compel designers and engineers to fabricate aerospace parts near their design limits. Due to the unpredictable nature of short fatigue crack growth it is of fundamental importance to fully characterize the performance of the chosen alloy in order to avert catastrophic failures. Furthermore, characterization of short crack behavior enables designers to specify inspection criteria since short fatigue cracks are very difficult if not impossible to detect using conventional non-destructive evaluation techniques used in the field. Extensive studies have been presented in the literature on short crack nucleation and propagation in aluminum alloys (Grosskreutz and Shaw, 1965; Zurek et. al., 1982; Morris et. al., 1976; Lankford, 1982) just to name a few. However, studies of the effects of anisotropy both at the local and macroscopic levels, on short fatigue crack initiation and propagation are sparse and more research is warranted to understand the anisotropy effect on short fatigue crack behavior. Anisotropy induced in wrought aluminum alloys stem from the rolling step during the fabrication (Bowles and Schijve, 1973; Staley, 1978). The rolling step acts to elongate the grains in the stretch direction, break up and elongate the second phase particles, and introduce a crystallographic texture in the worked material.

This research aims at characterizing the effects of anisotropy on the nucleation and propagation of short fatigue cracks in 2024-T351

aluminum alloy. Moreover, an attempt is made to quantify those crystallographic directions parallel to the stress direction which initiate fatigue cracks.

The following sections of this chapter will focus on reviewing the work published in the literature on characterizing failure causing modes and mechanisms in various aerospace grade aluminum alloys along with any proposed theoretical models used to predict the short crack growth behavior. Various stochastic models along with the effects of grain boundary misorientations will also be reviewed. Majority of the emphasis is placed on rolled aluminum alloys.

2.1 Short Fatigue Crack Nucleation and Propagation Mechanics

One of the earliest studies on fatigue crack nucleation and propagation in commercial aluminum alloys was done by Grosskreutz and Shaw (1965). They observed that fatigue fracture occurs in a sequential pattern, outlined as follows.

- Crack nucleation site
- Crack nucleation time (fraction of total time)
- Crack nucleation mechanism
- Crack growth rate
- Crack growth mechanism as determined by
    - Crack tip studies
    - Fracture surface studies

Their study compared fatigue crack initiation and propagation mechanisms between 1100-0 high purity (99%) and 2024-T4 commercial purity aluminum alloys. Studies on both alloys were done using notched dogbone samples. Slip bands in the 1100-0 aluminum alloy were

responsible for crack nucleation. Slip bands progressed into fissures that coalesced to form the primary fatigue crack. For the 2024-T4 aluminum alloy it was discovered that constituent particles were at the crack nucleating sites (Grosskreutz and Shaw, 1965). At lower stresses, only one crack would nucleate and propagate across the notch face, but at higher stresses multiple nucleation sites were reported. Nucleation of cracks at inclusions was credited to dislocation pileups at the inclusion/matrix interface although this was not directly observed. Fractography results indicated that crack growth across the crack front in both 1100-0 and 2024-T4 was heterogeneous and consisted of ripple formation, ductile tearing and cleavage fracture (Grosskreutz and Shaw, 1965).

A following study by Grosskreutz and Shaw (1968) aimed at determining if slip bands were responsible for the nucleation of fatigue cracks at inclusion interfaces. They also investigated the role, if any, of metallurgical stability of the precipitate structure in crack nucleation. Studies were performed on 2024-T4 notched dog bones at various stress amplitudes. Through optical microscopy and transmission electron/scanning electron microscopy (TEM/SEM), concentrated slip and higher dislocation densities were observed around the inclusion/matrix interface. However, a study of the crack nucleation sites at inclusion interfaces did not correlate concentrated slip with the nucleated crack (Grosskreutz and Shaw, 1968). The study also determined that density of

dislocations at the inclusion/matrix interface is an order of magnitude lower compared to pure metals. This finding seems to contradict the previous assertion made in the 1965 study that dislocation pileups at inclusions were responsible for crack nucleation. Further studies of micrographs did not reveal any reversions or overaging of the precipitate structure due to fatigue, which indicates a robust metallurgical stability. Moreover, the reduced dislocation densities can be attributed to the precipitate structure, which inhibits the dislocation motion. Crack nucleation was observed to take place at the inclusion/matrix interface by an as of yet undetermined mechanism. The authors also postulated crack nucleation due to fractured inclusions by either rolling or cycling, though no fractured inclusions were observed (Grosskreutz and Shaw, 1968). The authors hypothesized that a reduction in impurity elements such as Fe and Si could increase fatigue resistance of the alloy.

In addition to the intrinsic mechanisms discussed above, work done by Schijve and Jacobs (1965) studied the effects of notch and size effect on the fatigue behavior of short fatigue cracks. It should be pointed out though that microscopes used for observation in their work could not detect cracks until they reached 100 μm in length. They used three types of samples; unnotched, small notched and large notched, which were cut from 2024-T3 aluminum alloy (Schijve and Jacobs, 1965). The stress concentrations for small and large samples were equal. The authors contend that fatigue cracks initiate due to slip at the free surface away

from the inclusions. However, this assumption contradicts the direct observations by Grosskreutz and Shaw, who documented crack initiation at inclusion/matrix interfaces and not due to cyclic slip. The study concluded that larger notched specimens showed lower fatigue strength with respect to the small notched specimens. The result indicates a stochastic variable in the size effect. When the larger volume of material is exposed to high stress there is also an increase in the total number of weak spots under high stress which increases the probability of crack nucleation (Schijve and Jacobs, 1965).

Due to breakdown of large inclusions in smaller particle clusters during the rolling step. A paper by Bowles and Schijve (1973) tried to determine if cracked inclusions and inclusion clusters were more common as crack nucleation sites versus more isolated inclusions. They also evaluated if inclusions can be fractured/debonded by 4-5 % strain, which is readily applied to rolled aluminum alloys, and if these pre-cracked inclusions nucleated cracks (Bowles and Schijve, 1973). Material used for this study was 2024-T3 aluminum alloy plate by means of notched dogbones. Post pre-stretch analysis indicated fractured and debonded inclusions (albeit only a few instances were found). The fracture occurred due to the brittle nature of the particles induced by the presence of iron. The debonding was contributed to weak cohesion at the matrix/inclusion interface (Bowles and Schijve, 1973). Fatigue tests of the pre-strained material indicate that cracks can nucleate due to voids created by

debonded particles. Additional testing on material that was not pre-stretched indicates crack nucleation due to inclusions also. Authors observed that crack growth directions were noticeably influenced by inclusions ahead of the crack tip (Bowles and Schijve, 1973).

In a similar study to that done by Grosskreutz and Shaw (1965), Pearson (1975) studied crack nucleation and small fatigue crack propagation in a Al-Cu-Mg alloy designated BS L65 and a Al-Zn-Mg-Cu alloy designated DTD 5050. Notched specimens were tested in bending at various stress amplitudes and R-ratios. The top surface of the notch was evaluated with an optical microscope to document cracks. With this technique cracks were initially detected at approximately 0.025 mm long. While Grosskreutz and Shaw observed crack nucleation to occur due to debonding between matrix/particle interfaces, results of this study indicated that fractured inclusions also initiated cracks into the matrix (Pearson, 1975). A Linear elastic fracture mechanics (LEFM) approach was used for analysis of results. No corrections for large plastic zones were incorporated since it was discovered the plastic zone size was about 1/12 of the crack size even in the short crack regime. The crack growth rate of short cracks was calculated to be 1.27e-6 mm per cycle. This growth rate is substantially higher than extrapolated values from the crack growth data of long cracks (Pearson, 1975). In the equation $da/dN=A(\Delta K)^n$, n for cracks in the 0.025 mm regime was estimated to be equal to 1. However, these results contradict findings in steel which

predict n=7.5 for short fatigue cracks (Yokobori et. al., 1971). Once crack length reached 0.127 mm, the crack started to behave like a long crack with n=4 (Pearson, 1975).

Staley (1978) evaluated effects of microstructural features thst control strength, fracture toughness and resistance to fatigue crack growth in aluminum alloys. Microstructural features studied were inclusions, dispersoids and precipitates. It was observed that coarse constituent particles either fracture or separate from the aluminum matrix. Inclusion initiated cracks act to reduce the energy necessary for crack propagation effectively reducing fatigue crack growth resistance and fracture toughness. Overloads imposed on intermediate stress intensity values under monotonic loading can serve to retard the growth of the main crack by inducing microcracks at the inclusions. These microcracks thus decrease the stress intensity at the main crack tip (Staley, 1978).

Precipitates influence fatigue crack growth by imposed resistance to degradation of the Al alloy strength properties due to loading and environmental effects. Resistance to degradation is increased by either an increase in the Cu content or higher levels of precipitation (Staley, 1978).

In similar study to that of Grosskreutz and Shaw (1965) and Pearson (1975), Kung and Fine (1979) performed work on 2024-T4 and 2124-T4 aluminum alloys in an attempt to better understand the role of microstructure on initiation of fatigue cracks. The 2124 alloy is a higher purity version of 2024 with reduced Fe, Si and Cu content which

minimizes the density of constituent particles. As a result, 2124 possessed larger grain size that measured to be 45 μm in the transverse direction compared to 20 μm for the 2024 alloy. Both materials were tested under high and intermediate stress amplitudes along the rolling direction. At high stresses, fatigue cracks in 2024-T4 and 2124-T4 initiated at coarse slip bands. However, at intermediate stresses all of the observed cracks in 2024-T4 and 50% of cracks in 2124 were formed at inclusion sites. The study found no evidence that fractured or separated inclusions initiated cracks into the matrix. Rather cracks were observed to initiate where slip bands impinged onto the inclusions. They also observed microcracks being parallel to the slip planes, which suggests stage 1 crack growth (Kung and Fine, 1979). These findings stand in direct contradiction to results published by (Grosskreutz and Shaw, 1968; Morris, 1976; Pearson 1975; Bowles and Schijve, 1973) who observed crack initiation due to fractured and separated inclusions. The reduced Fe, Si and Cu in the 2124 alloys did little to increase the fatigue crack initiation resistance, which was attributed to the larger grain size. It was also observed that grain boundaries tended to retard or terminate microcrack growth (Kung and Fine, 1979).

A study performed by Lankford (1982) aimed at specifically determining metallurgical factors that govern the nucleation and propagation of short fatigue cracks. Notched specimens made of 7075-T6 aluminum alloy loaded in the rolling direction were used to study short and

long fatigue cracks (Langford, 1982). Fractography analysis indicated half penny shaped small cracks. Moreover, a severely tortuous crack path was observed near the grain boundaries where the direction of crack growth jogged left and right trying to accommodate the misorientation between the first and second grain (Lankford, 1982). This scenario indicated that crack growth was hindered by the grain boundary or rather by the misorientation between the two neighboring grains. This observation was independently correlated by the realization that a da/dN minima occurred at a length between 15-50 μm. The average grain depth normal to the surface was measured at 18 μm. Lankford deduced that certain favorably oriented grains accumulated large amounts of plastic strain as a result of microstrain accretion due to cyclic loading. The increased deformation in the grain causes an inclusion to fracture or separate from the matrix which leads to microcrack growth into the matrix (Lankford, 1982). The bulk plasticity in the grain controls the rate of short crack growth initially and not the crack tip plasticity as described by LEFM. Hammouda and Miller (1979) suggested that crack growth is controlled by the total plastic shear displacement at a crack tip given by

$$\Phi_t = \Phi_p + \Phi_e \quad (2.1)$$

When cracks are long compared to the microstructure $\Phi_t \approx \Phi_e$ and LEFM controls the crack growth (Hammouda and Miller 1979). On the other hand when $\Phi_t \approx \Phi_p$ it implies that crack is very short and $\Phi_e$is negligible because ΔK is very small. This phenomenon is represented in Figure 2.1.

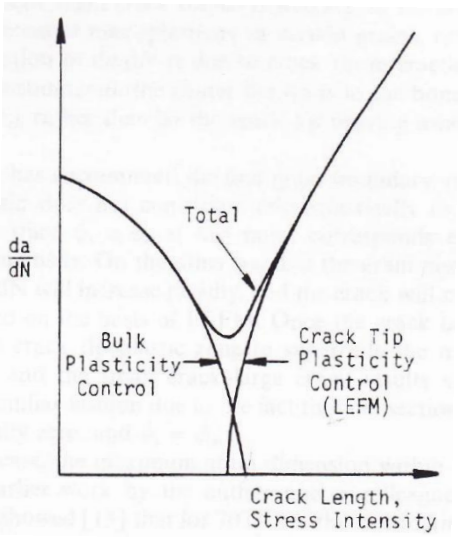

Figure 2.1: Schematic shows regions that are influenced by bulk plasticity and crack tip plasticity (Lankford, 1982).

Once the crack reaches the grain boundary either of two things can happen. If the second grain is oriented favorably with respect to the first and bulk plasticity is present in the second grain, the crack will simply continue growing into the second grain. If the second grain is not favorably oriented, the crack will either slow down or completely arrest. The crack arrest occurs due to lack of bulk plasticity which reduces the Φ_p contribution to Φ_t. Since the crack is short and ΔK is below ΔK_{th} the crack areas to grow. Short cracks become long cracks when the crack tip plasticity becomes larger that the grain size (Lankford, 1982).

In another study by Lankford (1985), an attempt was made to discern and define the criteria that define the short crack regime. The paper used short fatigue crack data generated in other publications for various materials including steel, titanium, aluminum and nickel base superalloys. For all the steels and the superalloy the crack growth of short

cracks either corresponded or was slower than the long crack growth rates. In the titanium and aluminum alloys, the short cracks experienced faster growth rates compared to those of long cracks (Lankford, 1985). Table 2.1 summarizes material performance along with the factors suggested for definition of the short fatigue crack regime.

Table 2.1: Summary of test results and suggested factors for small crack growth regime (Lankford, 1985).

Materials	$\frac{da^{sc}}{dN} > \frac{da^{lc}}{dN}$	$\frac{a}{M}$	$\frac{r_p}{a}$	$\frac{r_p^{min}}{M}$
Q + T 4130 steel [2]	No	>1	0.06	>1
Q + T 4340 steel [3]	No	>1	0.15	≥ 1
Q + T low carbon steel [4]	No	>1	0.06	≥ 1
IN 100 nickel-base superalloy [5]	No	>1	0.24	>1
IMI 685 Ti [6]	Yes	$\ll 1$	0.05	$\ll 1$
Ti–6Al–4V [7]	Yes	>1	0.11	<1
Ti–8Al [8]	Yes	$\lesssim 1$	0.26	<1
7075–T651 Al [9]	Yes	$\lesssim 1$	0.8	<1
DTD 5050 Al [10]	Yes	$\lesssim 1$	0.8	<1
3% Si steel [11]	Yes	<1	0.18	$\ll 1$
Al–bronze [12]	Yes	$\lesssim 1$	0.3	<1

The first column notes if short crack growth da^{sc}/dN is greater than long crack growth da^{lc}/dN. The second column refers to the question of whether short cracks grow fast only if the crack size is on the order of or smaller than some microstructural parameter like the grain size. The third column refers to a parameter (r_p/a) that suggests rapid short crack growth corresponds to the breakdown of LEFM. Lastly, the forth parameter (r_p^{min}/M) suggests that short cracks act differently than long cracks when the plastic zone is bounded by the microstructural parameter. Two parameters found to best describe the short fatigue crack regime are those given in columns 3 and 4. For (r_p^{min}/M), it can be seen that when (r_p^{min}/M)<1, the short crack growth rate is higher than corresponding long

crack rates. For column 3, the values of (r_p/a) vary greatly but a limiting value of (r_p/a)≤0.05 can be used to determine when LEFM analysis on crack growth data should be used (Lankford, 1985). The value of 0.05 was determined assuming (r_p^{min}/M)≈1.

Studies done up to this point in time clearly identified constituent particles as weak spots responsible for fatigue crack initiation in rolled Al alloys. Therefore, Tanaka and Mura (1982) extended a dislocation dipole accumulation model to predict the fatigue strength reduction in alloys containing inclusions. Crack initiation occurs when the self strain energy of dislocation dipoles accumulated at the inclusion sites reaches a critical level. Three crack initiating mechanisms at inclusions were considered: crack initiation due to a debonded inclusion, crack initiation due to fractured inclusions and initiation due to slip bands emanating from an uncracked inclusion.

For the case of a separated inclusion from the matrix the energy U_1 due to dislocations caused by loading is given by

$$U_1 = \frac{\tau\gamma_1^T}{2} - \frac{k\gamma_1^L}{2} + \frac{\pi a^2 \tau_1^2}{\mu} \quad (2.2)$$

Where μ is the shear modulus, k is the friction stress of dislocations, a is the inclusion radius, $\gamma_1^T$is the sum of displacements due to notch and slip bands and $\gamma_1^L$is displacement caused by slip. γ_1^T and $\gamma_1^L$are given by rather complex expressions which will not be included for sake of brevity. To calculate the increment of self energy ΔU_1 in each load reversal, τ_1 and k

are replaced by $\Delta\tau$ and 2k. The value of ΔU_1 is then used in equation 1.3 to obtain the crack initiation condition

$$2n_c\Delta U = 4lW_s \quad (2.3)$$

where n_c is number of cycles to initiate the crack, W_s is the specific fracture energy and l is the length of the slip band (Tanaka and Mura, 1982).

For the case of crack initiation due to the fracture of the inclusion, the energy stored in the inclusion that is generated by Orowan dislocation loops trapped at the inclusion/matrix interface is given by

$$U_1 = \frac{\mu'}{\mu'+\mu}\left(\frac{h+l}{h}\right)^2 \frac{\pi a^2}{2\mu}(\tau_1 - k)^2 \quad (2.4)$$

Where μ' is the shear modulus of the inclusion, l is the semi-major axis of the slip band zone and h is the semi-minor axis of the slip zone. A similar method for the calculation of increment of strain energy is used as for the case of debonded inclusion. Substituting the results of equation 2.4 into equation 2.3 yields

$$n_c = \frac{\mu'+\mu}{\mu'}\left(\frac{h}{h+l}\right)^2 \frac{4\mu W_I}{(\Delta\tau-2k)^2}\frac{1}{a} \quad (2.5)$$

This estimates the number of cycles till the crack initiates due to fractured inclusions (Tanaka and Mura, 1982).

For the last case of crack initiation due to slip bands emanating from the inclusion, the problem of dislocation pile up along the slip band needs to be addressed. Strain energy due to the dislocation pile up is expressed as

$$U_1 = -\frac{1}{2}\int_{-l}^{l} \tau_1^D(x)\Phi_1(x)dx \quad (2.6)$$

where τ_1^D is the shear stress generated due to dislocation pile up and $\Phi_1$is the displacement due to a dislocation pile up produced by the presence of the inclusion. The expression for the dislocation generated stress and displacement is complex and will be omitted for sake of brevity. The increment in strain energy is calculated in the same manner as above and results substituted into equation (2.3) (Tanaka and Mura, 1982). Predictions for the second and third cases agree well with the experimental results of Morris et. al. (1976) and Kung and Fine (1979).

Akiniwa and Tanaka (1988) used 2024-T3 aluminum alloy for the study of crack growth rates during fatigue testing. Crack behavior was observed from the onset of damage to crack lengths of 3 mm. The crack mainly initiated at inclusions and grew along preferentially oriented slip planes while the crack was still in the microstructurally short crack regime i.e., < 100 μm. The crack in this regime experienced large scatter in the crack growth. Scatter in the crack growth data was primarily attributed to the grain boundary interactions, which caused the crack to temporarily stop before continuing to grow. Well bonded inclusions were also observed to slow down the short crack propagation (Akiniwa and Tanaka, 1988). Scatter in crack growth reduced when the crack length reached 100 μm. While the crack still grew at higher rates than those predicted by Paris' Law, the crack growth changed from stage 1 to stage 2 (non-crystallographic) regime. Upon reaching a crack length of 500 μm or a crack growth rate of 1X10e^{-8} m cycles^{-1}, the crack obeyed the Paris law

(Akiniwa and Tanaka, 1988). At this time the calculated plastic zone size was on the order of the grain size, which agrees with observations by Lankford (Lankford, 1982). The study concluded that overall crack propagation rates were higher when compared to average growth rates, giving non-conservative estimates for crack lengths (Akiniwa and Tanaka, 1988).

Under the Advisory Group for Aerospace Research and Development (AGARD) initiative, considerable effort was made by numerous research institutions across multiple nations to study short fatigue crack effects. The short fatigue crack effect is defined by the ability of short cracks to grow at substantially higher rates and very low ΔK values (below ΔK_{th}) with respect to large cracks (Newman and Edwards, 1988). 2024-T3 aluminum alloy was tested under various stress intensities, R ratios, and loading conditions. Load conditions used were constant amplitude loading, Gaussian loading and actual flight time load (FALSTAFF) histories. Cracks initiated at inclusion that debonded or fractured and at particle clusters. For all R ratios cracks grew below ΔK_{th}. However, the small crack effect was more pronounced for negative R ratios where small crack grew faster than long cracks at stress intensities greater than ΔK_{th}. For Gaussian and FALSTAFF loading a similar effect of short cracks was also observed. For R≥0, small cracks grew at similar rates or slower than long cracks at stress intensities greater than ΔK_{th} (Newman and Edwards, 1988). A crack closure model used for crack

growth predictions of short cracks tended to under predict and over predict crack growth rates for negative and positive R ratios, respectively. For Gaussian and FALSTAFF loading conditions the model results were comparable to the observed experimental data (Newman and Edwards, 1988).

Brockenbrough and coworkers (1993), performed an extensive study on 7050-T7451 aluminum alloy. Aluminum plates of various thicknesses and purity were used to determine microstructural features that govern the crack initiation regime and subsequent failure of the part. Microstructural features mainly identified as culprits for crack nucleation were porosity and iron bearing inclusions. Due to the reported stochastic nature of fatigue performance in rolled aluminum alloys, the goal was to characterize the equivalent initial flaw sizes (EIFS) of defects responsible for the fatigue failure. It was observed that failure was due mainly to large inclusions/porosity and a lognormal density function was used to quantify their distribution. It was the hope to use the defect density functions in conjunction with a deterministic model to predict statistical distribution of fatigue lives for this alloy (Brockenbrough et. al., 1993). The study also reported variance in inclusion sizes with respect to the through thickness position. Larger inclusions/porosity were observed in the middle of the plates used for the fatigue study. This has been attributed to the inability of cold working to break up inclusions deeper in the material that are formed during the casting process (Brockenbrough et. al., 1993). While the

method used exerts considerable effort to characterize the distributions of crack initiating flaws, the procedure in itself does not attempt to model the mechanism of crack nucleation and propagation in early stages.

Work presented by Patton et. al. (1998) aimed at utilizing fatigue performance data gathered from 7010 alloy to predict number of cycles to failure as a function of loading conditions and microstructural features. Interrupted fatigue tests revealed that the majority of crack nucleating sites contained iron bearing particles (Al_7Cu_2Fe). Chemical etching revealed both intragranular and intergranular crack growth. Electron backscatter diffraction (EBSD) analysis of grains containing the small crack revealed a twisted cubic texture present. This texture corresponds to grain orientations for which the two largest Schmid factors are equivalent. To verify the influence of inclusions on the slip systems and critical resolved shear stresses (CRSS) Eshelby's theory was used. The computed stress tensor $\boldsymbol{\sigma_M}$ in the vicinity of the inclusion was used to calculate the CRSS. Similar results were obtained as previously, i.e., indicated two slip systems possessing highest equivalent CRSS's (Patton et. al., 1998).

A model was derived in (Patton et. al., 1998) for calculation of the number of cycles till failure incorporated crack deflection due to crack growth alternating between intragranular and intergranular growth. An energetic model was proposed as given below.

$$F(\theta) = -G + 2\gamma_p + 2\gamma_s \text{; intragranular crack growth} \quad (2.7)$$

$$F(\theta) = -G + 2\gamma_p + 2\gamma_s - \gamma_{gb} \text{; intergranular crack growth} \quad (2.8)$$

where G is the elastic energy released by unit area of crack growth, γ_p is the plasticity dissipated energy, γ_s is the energy dissipated to create new surface and γ_{gb} is the amount by which γ_s is reduced due to grain boundary presence. Θ_o is used as the governing parameter that controls the separation between intergranular and intragranular growth. When θ, which is the angle between crack plane and the grain boundary, is less than θ_o, then intergranular growth occurs otherwise intragranular growth is present. The number of cycles till failure is subsequently derived based on the amount of crack growth spent in the intergranular and intragranular growth. The expression is

$$Nr = \frac{1}{\pi B\{(1-R)\sigma_{max}\}^2\{fr\chi_t+(1-fr)\alpha_t\}} \ln\left[\left(\frac{\sigma_r}{\sigma_{max}}\right)^2\right] + \left(\frac{\sigma_r}{\sigma_{max}}\right)^2 \quad (2.9)$$

where χ_t and α_t are fractions of intergranular and intragranular growth (Patton et. al., 1998). Even though the model fits the experimental results well, the fact that the model showed no dependency on the grain misorientations is concerning especially since the model predicts the crack growth from the onset of damage. Moreover, work by Lankford (1982) indicates that crack growth in aluminum alloys can show crystallographic tendencies even when the crack is 10 grains long (Lankford, 1982).

Study performed by Merati (2004) aimed at correlating material microstructural properties to fatigue performance of 2024-T3 aluminum alloy. The author introduced a concept of Initial Discontinuity State (IDS), which characterizes microstructural features responsible for crack

initiation. This is a concept similar to the one introduced by Brockenbrough and coworkers in a 1993 paper called Equivalent Initial Flaw Size (EIFS) where 7050 aluminum was used for identification of crack nucleating flaws prior to fatigue testing. Merati argues that the IDS concept is more generic and applies to various structural geometries, loading conditions, stress states and failure modes, while the EIFS concept is constrained to only apply to specific part geometries, loading conditions, stress states and failure modes (Merati, 2004). Inclusion geometry features were characterized on the short-transverse (ST), longitudinal-transverse (LT) and longitudinal-short (LS) planes and fitted with a two parameter Weibull density function (Merati, 2004). Even though all three planes were characterized, all the samples were tested in the longitudinal direction, which exposed only the inclusion cross sections on the LS plane to the tensile loading. As a result of this loading orientation the majority of crack nucleation occurred at fractured iron bearing particles, which was confirmed with energy dispersion spectroscopy (EDS) analysis. Post fracture analysis revealed cracks generally initiated at the largest inclusions. Even though this trend was observed, no correlation between fatigue life and inclusion size was evident. Therefore, the author concluded that other microstructural features such as the grain size and high angle boundaries govern the propagation of short cracks (Merati, 2004).

In a study similar to the one described above, Merati and Eastaugh (2007) used the concepts behind IDS to characterize the failure initiating microstructural features for 7000 series alloys. While the study used both new and old variants of 7075 and 7079 aluminum alloys, only the results for the uncoated 7075-T6 specimens shall be discussed here as they pertain directly to the subject study. As with the 2024-T3 alloy used in the 2004 study, inclusion geometry and size was characterized on the ST, LT and LS planes. Large coarse particles were associated to iron bearing particles via the EDS analysis (Merati and Eastaugh, 2007). Similar hour glass specimens were used for fatigue testing as was the case for the 2024-T3 alloy. However, the 7075-T6 alloy was loaded in the transverse direction. Post fracture analysis revealed that out of thirteen samples tested only three failed due to large iron bearing inclusions. The remainder was presumed to have failed due to surface roughness. It is interesting to note that in a earlier study performed by Merati and coworkers on 7075-T6 alloy that all cracks initiated at iron bearing inclusions (Merati et. al., 2001). The main difference between these studies is the loading direction. Samples in the newer study were loaded in the transverse direction where as in the previous study samples were loaded in the longitudinal direction. It is difficult not to attribute the difference in the observed failure mechanisms to the effects of rolling induced anisotropy rather than the surface finish since the samples in the current study were polished before testing.

The objective of the work performed by Xue and coworkers (2007) on 7075-T651 aluminum alloy was to evaluate the mechanisms of fatigue in three critical stages. The stages comprise of damage incubation site, microstructurally short crack (MSC)/ physically short crack (PSC) growth and long crack growth. Hourglass fatigue samples were tested with the rolling direction parallel to the load. The size and shape distributions of inclusions and grains were calculated. Fractographic analysis confirmed the presence of iron bearing inclusions at the crack nucleating sites. The MSC regime was marked by the inclined fracture surface which signified crack growth along preferential slip systems. While the PSC regime was still influenced by the microstructure, the crack growth observed was predominantly perpendicular to the load axis. The microstructural effect served to alter the crack propagation rate and growth direction of the PSC as was evidenced by change in striation patterns across grain boundaries (Xue et. al., 2007). Besides inclusions, rolling induced anisotropy was also observed to influence the sites of failure inducing cracks. This effect was discussed using Figure 2.2.

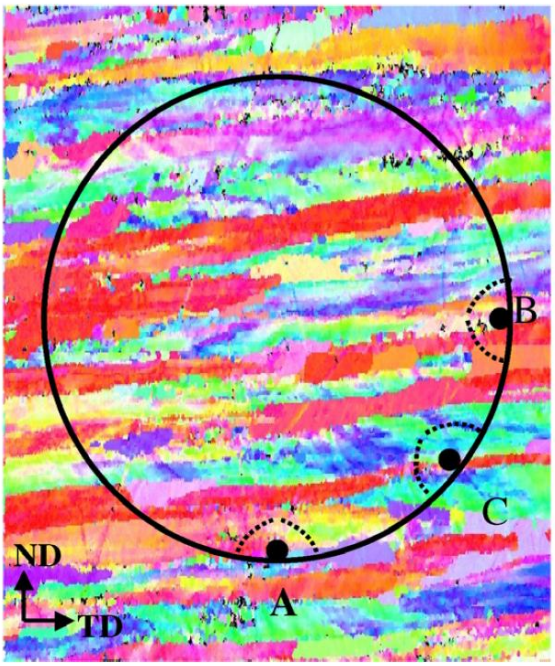

Figure 2.2: Schematic showing the effect of rolling induced anisotropy on crack nucleation sites (Xue et. al., 2007). Load is applied along the normal of the page.

Looking at three possible crack nucleating sites, location A has the highest probability of nucleating a failure inducing crack. Compared to positions B and C, a short crack in position A will encounter the lowest number of grain boundaries. Therefore, the likelihood of MSC being arrested in location A is significantly less with respect to locations B and C. Moreover examination of tested samples indicated a preference for failure causing cracks to initiate in locations similar to A (Xue et. al., 2007).

Weiland and coworkers (2009) performed a study to identify the role of inclusions on low cycle fatigue performance of 7075-T651 aluminum alloy. Analysis of material prior to testing showed no fractured inclusions due to the rolling step of the fabrication process. Post test analysis revealed that all primary cracks originated from fractured

inclusions. Larger inclusions tended to fracture while debonding was associated with small particles. Debonded particles outnumbered fractured ones three to one, however, no primary cracks originated due to debonding (Weiland et. al., 2009). As cycles increased, fractured particles and matrix cracks reached a saturation level. This trend was not observed with the debonded particles. It was observed that roughly 20% of fractured particles initiated cracks into the matrix (Weiland et. al., 2009). A crack nucleation site that propagated a crack into the matrix was chosen for serial sectioning and EBSD analysis in order to study the effect of inclusion geometry and grain orientation. Preliminary results indicate the crack growth in the matrix does not correspond to typical slip systems defined for an FCC crystal. Rather, the orientation of the cracked grains are $(110)[1\bar{1}0]$ and $(00\bar{1})[110]$. The crack was assumed to have formed under mode 2 conditions (shear stresses) since the crack orientation is 45 degrees with respect to the loading axis (Weiland et. al., 2009).

Similar study to the one above was performed by Payne and coworkers (2010) on 7075-T651 aluminum alloy. The purpose of the study was to develop detailed observations of the sequence of events that lead to a fatigue crack. Material was tested using notched dogbone samples loaded in the rolling direction. Unlike the study discussed above, pre test analysis of the alloy revealed fractured inclusions. In fact, 10% of inclusions analyzed were fractured prior to testing and only additional 2-3% fractured during testing (Payne et. al., 2010). Fatigue tests were

performed in the low cycle regime. Samples were evaluated throughout the testing process at a high frequency. Figure 1.3 below reveals some critical characteristics regarding damage evolution of this alloy.

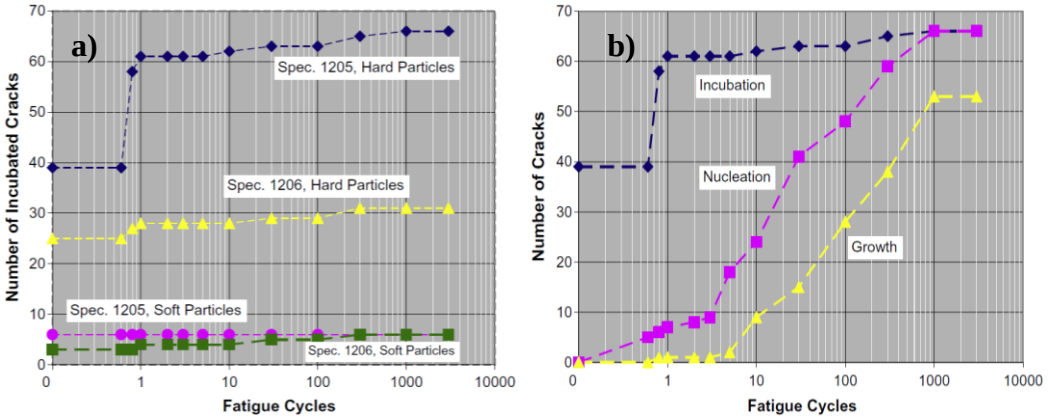

Figure 2.3: Plots showing the evolution of damage in 7075-T651 aluminum alloy. a) Figure showing incubation as a function of cycles. b) Figure showing all three stages as a function of cycles. Payne et al 2010.

The damage evolution was divided into three categories: incubation is the period of time it takes to fracture/debond an inclusion, nucleation is defined as the time at which first instances of cracking are observed in the matrix and growth is the time at which growth of the crack is observed in the matrix. As can be seen in Figure 2.3a, the bulk of broken particles were fractured prior to fatigue testing and the majority of additional particle fracture took place in the first loading cycle. Conversely, cycling did not cause additional softer particles to fail. Figure 2.3b indicated that no matrix cracks were observed prior to fatigue testing. Moreover, there seems to be a quiescent period between nucleation and growth as indicated by the Figure 2.3b. Small crack arrest was observed, this was attributed to unfavorable grain orientations and high angle boundaries (Payne et. al.,

2010). While the study claims to have performed EBSD analysis on the notch surfaces to characterize the grain orientations, no such discussion was found in the paper.

Work done by Zhang and coworkers (2010) dealt with quantifying the weakest links associated with the formation of fatigue induced damage. Material used for the study was A713 sand cast aluminum alloy that was fatigue tested in four point bending. Due to the absence of rolling, the material grains pose no preferential orientations. Moreover, the lack of rolling left in place porosity created during the solidification process. The majority of fatigue cracks nucleated at the porosity sites. Therefore, size and shape distribution of pores were quantified and a extreme value density function was fit to the distributions. However, post test analysis revealed that not all crack initiated at large pores. In reality, significant crack nucleation occurred at small pores and some cracks had no pore at the nucleation site at all (Zhang et. al., 2010). Although it could be posed that subsurface pores were responsible for the crack nucleation, the author dismisses this hypothesis, but does not give substantial argument for the reasoning. Since correlation between pore size and fatigue performance is poor, quantifying the number of fatigue cracks observed as a function of applied stress was accomplished. The plotted points were fitted with a Weibull density function. The authors define a new parameter called Strength Distribution of Fatigue Weakest Links (Zhai, 2006), which is calculated by taking the derivate of the fitted Weibull function. The newly

developed expression was more appropriate for evaluating fatigue performance since it counted the actual fatigue damage sites. The study proposed the use of two terms derived from the new expression as material properties, N_o and n which are the density of fatigue weak links and characteristic strength distribution, respectively. For good fatigue performance N_o should be small and n should be as large as possible (Zhang et. al., 2010).

Zheng and coworkers (2011) studied fatigue performance of 2524-T34 aluminum alloy using four point bending tests loaded in the rolling direction. 2524-T34 alloy is a new generation 2000 series alloy developed to replace the widely used 2024 alloy. Increased fatigue performance stems from lowering Fe and Si content along with modifying levels of Cu and Mg (Zheng et. al., 2011). Observations throughout the testing process revealed crack nucleation sites to occur at surface pits or constituent particles. The majority of crack initiating sites contained iron bearing inclusions but softer Al_2CuMg inclusions were found to nucleate cracks as well. Fatigue tests revealed a marked improvement in fatigue strength over the conventional 2024 alloy. Fatigue strength of 2524 at 10^7 cycles was estimated to be around 252 MPa compared to 140 MPa for 2024 aluminum alloy. Analysis of fracture surfaces showed short crack growth to occur along slip planes, which is consistent with general observations made on other Al-Cu-Mg alloys. Significant crack meandering and sharp change in crack direction revealed strong influence of grain boundaries on

early crack growth. Large twist angles between adjacent grains were proposed as main controlling factors influencing short crack growth that dictate whether cracks will proceed or arrest (Zheng et. al., 2011).

The collection of papers reviewed above deal extensively with crack initiation and propagation of short cracks. Mechanisms by which cracks nucleate during fatigue loading are extensive and include pores, cyclic slip, fractured particles, separated particles and slip bands emanating from inclusions. Moreover, different nucleating mechanisms were observed by different authors working on the same alloy variant (Grosskreutz and Shaw, 1968; Kung and Fine, 1979; Pearson 1975). The source of differing observations is difficult to pinpoint, they could be legitimate or simply an artifact of dissimilar testing and analysis methods. Whatever the case may be, the prevalent thought is that cracks nucleate due to fractured or debonded particles. The observation of fractured versus debonded particles also depends on the alloy variant studied. In the above literature no discussion on anisotropy effects on fatigue performance was offered. However hints suggesting the significance of anisotropy on material performance can be found. The most prevalent example comes from paper by Merati and Eastaugh (2007) where results from fatigue tests performed on 7075 aluminum in transverse direction did not match results from a previous study in which samples were loaded in the longitudinal direction. Although the authors attributed the difference to variability in the surface finish, it is far more likely that differences

observed were due to rolling induced anisotropy (Merati and Eastaugh, 2007). The following section will deal with studies that were aimed at quantifying the effects of anisotropy on fatigue performance.

2.2 Effect of Anisotropy on Fatigue Performance

Work done by Morris et. al. (1976) on 2219-T851 aluminum alloy aimed at understanding crack nucleation and propagation properties of small cracks as a function of stress amplitude, sample orientation and environmental effects. Specimens were tested in longitudinal and transverse directions, respectively. It was discovered that fractured inclusions governed crack initiation in longitudinal samples. Conversely, no crack nucleation due to inclusions was discovered in transverse samples. Rather, crack nucleation occurred at grain boundaries. As a result, lifetimes of transverse samples were twice the lifetimes of longitudinal samples (Morris et. al., 1976). At higher stress values $\sigma \geq 0.6\sigma_y$, multiple cracking in longitudinal samples was observed. The cracks then coalesced into a single failure inducing crack. The crack coalescence provided a means for small cracks to jump the grain boundaries, which reduced the life of the sample (Morris et. al., 1976). Increased humidity served to increase the mean crack length and reduce the number of crack initiation sites. This decrease in crack nucleation sites was credited to a weakened particle/matrix interface preventing fracture of inclusions (Morris et. al., 1976). While no detailed discussion on differing

crack nucleation mechanics was given, this paper serves as one of the first studies showing the significance of macroscopic anisotropy.

Zabett and Plumtree (1995) performed tests on 2024-T351 to investigate the effects of grain boundary spacing along different plate directions on fatigue performance. Tests were conducted on polished cylindrical samples loaded in the longitudinal (L), transverse (T) and short (S) directions. The reported grain sizes for the three directions were 350 µm, 110 µm and 38 µm in the L, T and S directions respectively. Fatigue testing at $\frac{\sigma}{\sigma_y}$=0.45 produced fatigue lives in the T direction of 236,000 cycles followed by S and L directions respectively at 143,000 and 127,000 cycles. Fractography analysis revealed iron rich inclusions as crack nucleating sites for the L samples. All of the initiating inclusions were fractured during the rolling process. For the T and S directions on the other hand the crack initiated in the matrix due to persistent slip band formation which is consistent with the results reported by Morris and coworkers (Zabett and Plumtree, 1995). While the S direction samples displayed no preference in crack nucleation sites, T samples predominantly initiated cracks in the largest grains (Zabett and Plumtree, 1995). Observation of crack growth rate versus crack length displayed higher incidence of crack retardation in the T and S samples compared to L samples. This was mainly due to multiple cracking which acts to speed up crack growth through coalescence in the L samples. Moreover, fractured inclusions on grain boundaries act as bypass mechanisms

preventing interactions between crack tip and the grain boundaries. Difference in fatigue lives between T and S samples were attributed to earlier onset of crack nucleation in the S samples, due to narrower slip bands found in smaller grains of the S direction compared to broader slip bands found in the larger grains of T samples. Furthermore, smaller grain boundary spacing in the crack depth direction in the T samples acted to retard the crack growth sooner compared to larger grain boundary spacing present in the S samples (Zabett and Plumtree, 1995).

A Study performed by DeBartolo and Hillberry (1998) addressed the effects of early crack coalescence due to particle clusters on fatigue performance of 2024-T3. The study used single edge notch specimens (SENT) similar to those used in the AGARD study. Samples were cut on LS, ST and LT planes. Furthermore, samples on the LT plane were cut perpendicular to the rolling direction (non-preferentially oriented samples) and parallel to the rolling direction (preferentially oriented samples). For the preferentially oriented samples the crack growth direction will be aligned along stretched inclusions and grains. This configuration exposed the crack path to an increased number of stringers produced by rolling. A model was also developed to predict the effect of crack coalescence due to particle clusters. Data for da/dN versus ΔK from the AGARD study were used for crack growth predictions and Newman's elastic solution for K was implemented assuming crack growth in the center of the notch.

$$K = S\sqrt{\frac{\pi a}{Q_{Fn}}}\left(\frac{a}{c}, \frac{a}{t}, \frac{c}{r}, \frac{c}{w}, \frac{r}{t}, \frac{r}{w}, \Phi\right) \quad 2.10$$

Where a, c, t, w, r and Φ are geometry variables. Crack interaction was modeled using Yokobori's equation (Stress Intensity Factor Handbook, 1987) found below

$$\Delta K_I = \frac{1}{2a}\sqrt{(d-a+b)(d-a-b)}\left(\frac{(d-a+b)E(k)}{(d-a-b)K(k)}\right)\Delta K_I \quad (2.11)$$

where E(k) and K(k) are elliptical integrals, a and b are crack lengths, d is the center to center separation between the cracks and k is a function of d, a and b. Predictions imply small reduction in fatigue lives initially as the separation between particles widens but then an increase in fatigue life is observed and levels off as separations between the coalescing particles reaches a millimeter in length (DeBartolo and Hillberry, 1998). Experimental results for the LS specimens showed single particles responsible for crack nucleation and propagation, no coalescence of cracks were observed on any LS specimens. Similar results were also attained for the ST specimens, however, one observation of crack coalescence was made but this sample had the longest fatigue life of all ST samples. Fatigue lives for all LT specimens were lower when compared to LS and ST specimens. Non preferentially oriented LT samples did not show any crack coalescence, showing similar results to LS and ST samples. However the preferentially oriented samples showed a large amount of early life coalescence in particle clusters. Life for the preferentially oriented samples is about 30% less than non-preferentially

oriented samples. This was attributed to the fact that many particles were oriented along the path of the crack as well as larger grains, which reduced the amount of grain boundaries the crack had to cross (DeBartolo and Hillberry, 1998). Interestingly enough, the authors did not observe any crack retardations due to the reduced grain thickness in the crack depth direction. While the grains on the surface were large, they were also quite thin in the crack depth direction and crack retardation would be expected due to bulk grains, which was a phenomenon reported in the previous study performed by Zabett and Plumtree (1995).

Zhai (2006) investigated fatigue performance of an 8090 aluminum alloy in LT, LS, ST and SL oriented samples using four point bending tests at various stress intensities. Experiments showed higher comparable fatigue lives for LT and LS samples and lower comparable fatigue lives for the SL and ST samples. Reduced fatigue strength in the SL and ST samples was attributed to segregated Li, Na and K in the grain boundaries. Since more grain boundaries are present in the S direction, increase in crack nucleating sites caused a decrease in fatigue life. This was confirmed by fractography, which indicated intergranular failure in the ST and SL samples. LT and LS samples experienced cleavage type fracture typically along {100} planes which was confirmed with EBSD (Zhai, 2006). While fatigue lives between LS, LT and SL, ST samples were similar, the number of cracks differed. Variance in the number of cracks in LS and LT samples is due to disparity in grain sizes on the

sample surfaces. Difference in the observed number of cracks in the SL and ST samples was attributed to differing lengths of grain boundaries between the samples. LS samples experienced more cracks due to increased number of grains and SL samples had a higher occurrence of cracks because of longer grain boundaries (Zhai, 2006). The Number of cracks as a function of stress level was fitted using a Weibull density function. Subsequently, taking a derivative of the expression gives rise to the equation below

$$n = CN_o \left(\frac{km}{\sigma_o}\right)\left(\frac{\sigma-\sigma_o}{\sigma_o}\right)^{m-1} e^{\left[-k\left(\frac{\sigma-\sigma_o}{\sigma_o}\right)^m\right]} \quad (2.12)$$

where n is the number of fatigue weakest links and N_o is the density of fatigue weakest links. While S-N data for LS, LT and SL, ST did not show any dissimilarities, the expression above shows a slight improvement between LT and LS where LT has slightly better fatigue performance due to lower crack count. A similar observation was made for SL and ST samples where ST shows a slight advantage over SL samples.

Morris and coworkers (1976) were among the first to recognize the importance of anisotropy in fatigue performance of rolled aluminum alloys. Zabett and Plumtree (1995) confirmed their findings on 2024-T351 by observing crack nucleation due to inclusions in the L samples while T and S samples failed due to persistent slip bands (Zabett and Plumtree, 1995). DeBartolo and Hillberry (1998) performed similar tests on 2024-T3 and discovered crack initiation in all three directions occurred at fractured or

debonded inclusions (DeBartolo and Hillberry, 1998). The 8090 aluminum alloy studied by Zhai (2006) revealed similar tendencies of varying fatigue performance with respect to directions tested. While the fracture mechanisms differed with respect to the 2000 series alloys, the conclusion is that anisotropy is a significant factor in rolled material fatigue performance (Zhai, 2006). While work by Zhai incorporated the use of EBSD to study the effect of grain morphology on fatigue crack performance, no such work could be found for 2000 series alloys that included anisotropy in their study. Moreover, it is believed that Zhai (2006) only obtained grain orientations for those grains which possessed cracks; therefore, not studying the full distribution of grain orientations that could be susceptible to fracture. Therefore, the aim of the current study is to not only account for the anisotropy effect, but to also perform a detailed analysis on crystallographic directions which are most susceptible to short crack propagation. Additionally, enough samples will be tested to give a statistical distribution of fatigue lives in various material directions that can be used for simulation purposes.

Two papers to be presented next do not deal explicitly with the propagation of short fatigue cracks. Rather the effect of anisotropy was evaluated on long crack growth. However, the effect of anisotropy in this regime of crack growth is still quite evident as will be seen below.

Effects of rolling induced anisotropy were studied by Wu and coworkers (1994) using compact tension (CT) specimens made of 8090

lithium aluminum alloy. The CT specimens were loaded parallel to the rolling direction and 15, 30, 45 degrees inclined to the rolling direction. Crack growth rates in the Paris regime (ΔK~15 MPa.m$^{1/2}$) for the LT and LT+15 degrees were about 5e^{-4} mm/cycle and about 1e^{-4} mm/cycle for the LT+30 and LT+45 degrees. The authors assert that differences in crack growth rates cannot be accounted for by roughness induced crack closure and that anisotropy is the primary culprit for varying crack growth rates (Wu et. al., 1994). Examination of fractured surfaces through the thickness revealed a crystallographic crack path. In fact, angles observed on the crack path strongly matched predicted values for angles of intersection formed by $(1\bar{1}1)$ and $(\bar{1}11)$ slip planes. The lowest crack growth rate was observed in the longitudinal (L) sample followed by L+15 degrees. The L+30 and L+45 degree samples had similar growth rates (Wu et. al., 1994). A modified transgranular fatigue crack growth model was developed to account for anisotropy and can be seen below.

$$\frac{da}{dN} = \frac{(\alpha_f - \alpha_r) cos^2\Phi}{12\pi V H \sigma_y^2 (1-R)} (\Delta K)^3 \quad (2.13)$$

The angle Φ is given by the load vector and normal of the slip plane. The added $cos^2\Phi$ accounts for the texture present in the alloy. If no texture is present Φ=0 and the expression reduces to the original one, which is simply equation 2.13 without the cos^{2}Φ term, however, when Φ≠0, growth rate reduces due to presence of anisotropy. The authors concluded that change in growth rates is more a function of anisotropy than roughness

induced crack closure. Moreover, negligible amounts of roughness induced crack closure were observed during testing (Wu et. al., 1994).

Similar work was done by Chen and Chaturvedi (2000) on 2195 lithium aluminum alloy. While work above focused more on the intermediate range of ΔK crack growth, present work dealt mainly with anisotropy influence on the near threshold crack growth. CT specimens with LT, LT+15º, LT+30º, LT+45º and LT+90º (TL) orientations were prepared. Standard load shedding techniques were used to determine ΔK_{th} values for different orientations. Reduction in ΔK_{th} values with increasing R-ratio was observed for all orientations with LT-45º yielding the lowest ΔK_{th} values of all tested directions. LT and TL orientation had the highest ΔK_{th} values with LT+15º and LT+30º falling in the middle. Dependence of ΔKth orientation was mainly attributed to macroscopic fatigue crack deflection caused by the crystallographic texture. LT+45º samples had the lowest crack deflection and TL samples gave the largest crack deflection angles. The increased deflection angle reduced the crack driving force K_I and produced a less damaging mixed mode crack growth. The effect of specimen orientation was less pronounced in higher crack growth rates and larger R ratios. Observed crack growth exhibited strong crystallographic nature. Angles created by the meandering crack path were 70.5 or 109.5 degrees, which correspond to crack growth along {111} planes. Similar trends were observed in the previous study for 8090 lithium aluminum alloy (Chen and Chaturvedi, 2000).

In section 2.1 many studies outlined recognized the statistical nature of the fatigue properties for rolled aluminum plates. Because constituent particles were identified as the main instigators of crack initiation some studies aimed to gather statistical distributions of particle sizes (Brockenbrough, 1993; Merati, 2004; Merati, 2007) in the future hopes of integrating the statistical data with a stochastic model to predict fatigue life distribution and crack propagation rates. This section will outline proposed models which aim to predict fatigue life distribution and crack propagation rates. Proposed models utilize microstructural data and correlate them to the fatigue performance of the aluminum alloy. The outlined stochastic models do not account for anisotropy and assume material loading in one direction.

2.3 Probabilistic Modeling

Results from a 1994 paper by Brockenbrough and coworkers (1993) were used in a paper published by Magnusen et. al.(1997), the material data on inclusions and porosity gathered in the above study were incorporated into crack growth and stochastic models to predict the fatigue life distribution of 7050-T7451 aluminum alloy. The model assumed initial damage (cracks) of the size of inclusion/porosity and cracks were grown from this initial condition. The study used a fracture mechanics model developed by Grandt et. al. (1984, 1986) for prediction of fatigue lives. The model also incorporated Newman-Raju stress intensity factor solution to describe the crack driving model (Magnusen et. al., 1997). Since the

model dealt with crack growth in the short crack regime, ΔK values obtained for long cracks were extrapolated back in linear fashion to obtain crack growth rates for short cracks. Once the model was constructed, Monte Carlo and Latin Hypercube sampling was implemented on the measured distribution of initial flaw sizes, locations and type to develop the fatigue life distributions for 7050 aluminum (Magnusen et. al., 1997). Although the predicted values matched experimental results well, it was determined in previously outlined studies (Lankford, 1982; Lankford, 1985; Newman and Edwards, 1988) that extrapolation of long crack results for the short crack regime is ill advised. One of the possible reasons for good correlation is that the experiments were all performed in tension-tension loading where the small crack effect is less pronounced than for the negative R ratios (Newman and Edwards, 1988).

A study similar to that of Magnusen et. al. (1997) was conducted by Laz and Hillberry (1997) for 2024-T3 aluminum alloy. The study aimed at predicting the fatigue life distribution based on the size and shape distribution of iron rich inclusions responsible for crack nucleation. The particle size and shape distributions were used in unison with a stochastic model that was implemented using the Monte Carlo method. To account for the short crack effect, the model incorporated the crack closure model developed by Newman that was previously used in the AGARD study. A three parameter lognormal density function was used to fit the inclusion size and shape distributions. The three parameters measured were the

inclusion area, length and width. The expression for the lognormal density function can be seen below

$$f(x) = \frac{1}{(x-\tau)\sigma\sqrt{2\pi}} e^{\left\{\frac{(ln(x-\tau)-\mu)^2}{2\sigma^2}\right\}} \quad (2.14)$$

where τ, σ and μ are the threshold, shape and scale parameters. Experimental results pointed out to large particles as crack nucleating sites, which belong to the upper tail of the distribution. The model successfully predicted the shortest experimental fatigue lives and their spread. However, instances occurred where the measured and predicted experimental lives were considerably different (Laz and Hillberry, 1997). This was attributed to the misorientations between adjacent grains which were not accounted for in the crack closure model.

Maymon (2004) used a unified approach for calculating crack growth rates in 2024-T351 aluminum alloy. The unified approach dictates that crack growth will occur only when two parameters are met, ΔK and K_{max}. The crack growth model developed based on the unified approach was incorporated with an EIFS distribution characterized by a Weibull density function. The crack growth model was numerically solved using a TK solver program by UTS. No crack growth was assumed if da/dN=1X10e-10 m/cycles and the flaw sizes were below 16.8 μm (Maymon, 2004). Definition of these limiting factors was vague and it appears that they were arbitrarily chosen. The simulation was carried out assuming an infinite plate with a hole in it. The initial crack sizes were

determined by the EIFS distribution given by the Weibull function. The model predicted a mean life of 47,215 cycles with a standard deviation of 12,363 (Maymon, 2004). The predicted results were not compared to any experimental ones so the accuracy of the model is difficult to assess. The model does not account for any microstructural effects due to texture and does not deal with the stochastic nature of the actual crack growth due to microstructural barriers.

A study done by Liao and coworkers (2008) aimed at using previously gathered distributions on size and shape of second phase particles and short crack modeling to predict distribution and mean of fatigue lives for 2024-T351. Work presented is a continuation of the IDS methodology previously discussed by Merati and Eastaugh (2007). Particle width and height distributions were fitted with a three parameter lognormal density function. Due to lack of crack growth data, short crack and long crack data from the AGARD study was incorporated (Liao et. al., 2008). It should be pointed out, though, that crack growth data gathered in the AGARD study were for 2024-T3 aluminum alloy where the alloy studied here is 2024-T351. No modification to data was mentioned in this paper to account for the differing tempers. A modified AGARD-NRC short crack growth model was used to simulate crack growth rates. ΔK values used for the simulation came either from the AGARD study or were extrapolated from existing da/dN-ΔK plots. The modified AGARD-NRC model gave reasonable life estimations but could not predict life scatter

and distribution. To accomplish this task, the AGARD-NRC model was incorporated into a Monte Carlo simulation. The stochastic model made predictions using either two or three random variable inputs. The first two random variables are particle width and height distributions. The third random variable is a ΔK_{IDS} value that accounted for variance in short crack growth due to grain boundary blocking (Liao et. al., 2008). Not a lot of detail was given on estimation of ΔK_{IDS} but it appears that it was numerically back calculated by fitting existing fatigue crack growth data. Monte Carlo simulations provided better estimates for fatigue life distribution and mean life when all three variables were incorporated. Moreover, by incorporating ΔK_{IDS}, instances where small inclusions cause shorter lives and large inclusions causing longer lives were captured (Liao et. al., 2008). While the model did use fracture mechanics principles to predict short crack growth, the model gave good predictions based on experimental results.

It is well known that only a small fraction of crack nucleating particles initiate cracks and a fewer still generate failure inducing cracks. A paper presented by Liao (2009) continues with the IDS philosophy and recommends further refinement in search of a statistical model for predicting fatigue life of 2024-T351. While IDS particle distributions are easily attainable, gathering statistical data on particles that nucleate primary cracks is cumbersome due to investment in experimental time and resources. Size and shape distributions of failure inducing particles are

considered fatigue subsets in this study and provide more accurate distribution of most critical inclusions. Therefore, stochastic models were proposed that allow for calculation of fatigue subsets based on IDS particle distribution data without the need for extensive testing (Liao, 2009). Distributions of particle size and shape were quantified on the ST, LT and LS planes. Weighted three parameter lognormal density function was used to fit the data since it gave the best fit in the upper and lower tails of the distribution.

The first model proposed was based on extreme value theory. When the IDS particle distribution follows a lognormal distribution, the extreme value of the largest particles (defined as a fatigue subset) is asymptotic to a Frechet distribution which is given below (Liao, 2009).

$$F_s(x) = e^{\left[-\left(\frac{a}{x-\tau}\right)^b\right]} \quad (2.15)$$

Expressions for a and b are omitted for sake of brevity but can be found in the subject paper. The extreme value model overestimates the fatigue subset distribution. This is mainly due to the fact that not all largest particles nucleate cracks. Only those particles among the largest that are located within a grain with favorable size and orientation do so. To account for the crystallographic effect, a critical density parameter D_{CP} was back calculated from the data in order to best fit the distribution to the experimental results. However, this defeats the purpose of the proposed solution because fatigue subsets are to be calculated by using only the

IDS particle distribution data with little or no experimental results to aid in fitting the predicted distribution to experimental results (Liao, 2009).

To bypass this issue a Monte Carlo simulation was invoked to predict the fatigue subset distribution based on IDS particle distribution incorporating other microstructural features such as grain size and grain orientation. Four fatigue criteria were used in the Monte Carlo prediction as outlined below.

1. Cracks are nucleated at the largest inclusions.
2. Cracks nucleate at large inclusions at or near large grains.
3. Crack nucleate at large inclusions at or near large grains with favorable orientation.
4. Criteria 3 along with a non-arrest crack condition used to screen out arrested cracks.

Criteria 1 gave similar results to the extreme value theory, which is expected. Conditions 2, 3 and 4 gave most accurate predictions depending on the thickness of the plate used in the study. No significant difference was found between predictions using criteria 3 and 4 leading the author to question the statistical significance of the crack arrest condition (Liao, 2009).

Constituent particles have been thoroughly linked with crack nucleating sites in rolled aluminum plates (Grosskreutz and Shaw, 1965; Bowles and Schijve, 1973; Pearson, 1975; Payne et. al., 2010). However, nucleation is only a single factor in a two step process that includes

propagation. Specifically, short crack growth is greatly influenced by the surrounding crystallography (Langford, 1982; Langford, 1985). Therefore, the following section will discuss models developed to predict effects of crystallography on short crack growth.

2.4 Crystallographic Short Crack Growth Models

Work by Zurek et. al. (1983) on 7075-T6 aluminum alloy studied the effects of grain size and stress ratio R on small fatigue crack growth. The grain sizes selected were 12 and 130 μm and R ratios of 0 and -1. Fully reversed loading causes higher crack growth rates with respect to the tension-tension loading. This was attributed to increased compressive stresses created by microplasicity induced during cyclic loading for the R=0 case. Higher compressive stresses were reported in larger grained material (Zurek et. al, 1983). Even though short crack retardation was observed near the grain boundaries, the authors opted for a plasticity induced crack closure model omitting any grain misorientation factors. For the large grain material ΔK_{eff} is given by

$$\Delta K_{eff} = 1.12(\sigma_{max} - \sigma_{cc})\sqrt{2c} \quad (2.16)$$

where σ_{cc} is the crack closure stress, which was empirically determined. After slight further development equation 2.16 is substituted into the expression $dc/dN=A(\Delta K_{eff})^n$ which yields,

$$\frac{dc}{dN} = A\Delta K^n \left[1 - \alpha z \left(\frac{1.12\sigma_{max}}{\Delta K}\right)^2\right]^n \quad (2.17)$$

parameters α, n and A are all determined empirically (Zurek et. al, 1983).

For the small grain material, the crack growth model was based on the assumption that crack growth rate at low stress amplitudes is the function of the degree to which grain boundaries affect crack growth (Zurek et. al, 1983). It was postulated that at sufficiently high stress amplitudes, the grain boundaries do not retard the crack propagation. The model utilizes a parameter which calculates the fraction P(2c) of cracks stopped by the grain boundaries and is given by

$$P(2c) = \frac{\Delta N_I}{\Delta N_P + \Delta N_I} \quad (2.18)$$

Where $\Delta N_P \; and \; \Delta N_I$ are the number of cycles spent propagating and stopped at the grain boundaries. Substituting the above expression for $(dc/dN)_m = dc/dN * (\Delta N_P/(\Delta NP + \Delta N_I)$ yields

$$\left(\frac{dc}{dN}\right)_m = \frac{dc}{dN}[1 - P(2c)] \quad (2.19)$$

The models proposed correlated well with the experimental data (Zurek et. al, 1983). However a large fraction of small cracks arrest completely and the model presented here cannot be used to account for the properties that lead to crack arrest. The model is only valid if the crack is assumed to grow past the small crack regime into the large crack regime.

A crystallographic model was proposed by Zhai and coworkers (2000) that with aid of the EBSD technique predicts microstructurally small fatigue crack behavior due to interactions with the grain boundaries. The model was developed on the basis that twist and tilt due to grain misorientation govern fatigue crack growth and explain erratic growth

behavior of short cracks. Short cracks grow along preferential slip systems and the rate of crack growth from slip plane in grain 1 to the slip plane in grain 2 is governed by the degree of misorientation. A schematic depicting this phenomenon can be seen in Figure 2.4.

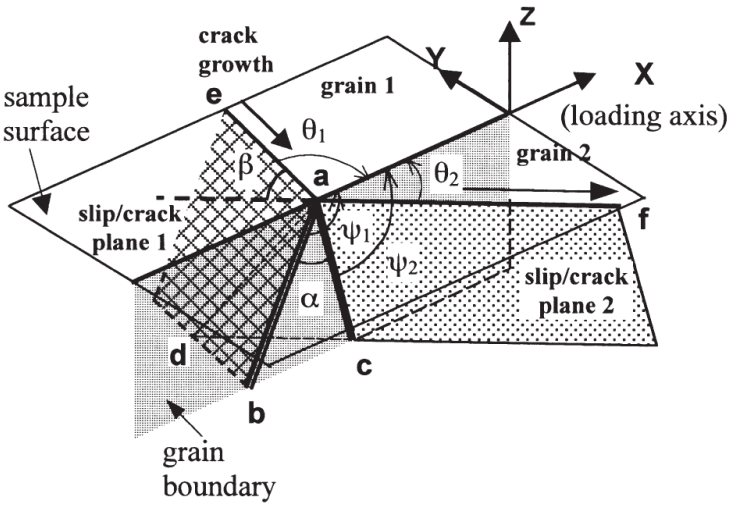

Figure 2.4: Diagram depicting crack growth across the grain boundary from one preferential slip system to the next located in grain 2 (Zhai et. al., 2000).

The orientations of the slip planes in grains 1 and 2 are defined by angles θ and Ψ with respect to the loading axis X. The misorientation angles between the two slip systems are given by $\alpha = |\Psi_1 - \Psi_2|$ and $\beta = |\Theta_1 - \Theta_2|$, where α is the twist angle and β is the tilt angle. Of most importance is the twist angle where in order for a small crack to propagate, the wedge area created by triangle abc needs to be completely fractured in order for crack growth to resume (Zhai et. al., 2000). Tilt angle β contributes to crack retardation by effectively varying the mode I and mode II stress intensity factors resulting in reduced crack growth. Grain boundaries are assumed to be always parallel to the XZ plane. This

assumption is reasonable since grain structure in the 8090 aluminum lithium alloy is pancaked due to rolling. This assumption would not be valid, however, if the grain shapes were equiaxed in nature. With the above assumption made, angles α and β can be computed as follows

$$\alpha = \cos^{-1}\left(\vec{E}X\overrightarrow{N_1}\bullet\vec{E}X\overrightarrow{N_2}\right) \quad (2.20)$$

and

$$\beta = \cos^{-1}\left(\vec{Z}X\overrightarrow{N_1}\bullet\vec{Z}X\overrightarrow{N_2}\right) \quad (2.21)$$

where $\vec{E}$, $\vec{Z}$, $\overrightarrow{N_1}$ and $\overrightarrow{N_2}$ are the unit vectors of the GB plane normal, sample surface normal and normals of the two preferential slip planes located in grains 1 and 2. To attain orientations of all possible slip planes and slips directions in the sample coordinate system, the rotation matrix **B** given by the EBSD software was used to relate crystallographic coordinates of individual grains to the sample coordinates. With the **B** matrix the slip plane and slip direction normals could be calculated for sample coordinates. In order to determine which {111} was activated, angles θ and Ψ need to be computed and correlated to the observed crack angles present on the samples surfaces. Expressions for θ and Ψ are given by

$$\Theta = \cos^{-1}\left(\vec{N}X\vec{T}\bullet\vec{L}\right) \quad (2.22)$$

and

$$\Psi = \cos^{-1}\left(\vec{N}X\vec{S}\bullet\vec{L}\right) \quad (2.23)$$

where $\vec{T}$ and $\vec{S}$ are unit vectors in the S and T directions respectively. This model was used to interpret crack growth behavior in 8090 aluminum lithium alloy across the grain boundaries. Observed crack growth across the grain boundary of two grains revealed significant amount of crack

stepping as the crack grew across the boundary. The serrated steps were attributed to a large twist angle that acted to slow down crack growth by transferring crack growth to unfavorable slip planes and increased fracture path generated by continuous crack stepping (Zhai et. al, 2006). The above conclusion was verified by the model's predictions for the twist angle. In other instances where no stepped crack front existed and no decelerations were observed, the model predicted very low twist angles. While in the above case the crack was decelerated, in other cases higher twist angles will cause the crack to arrest. Similarly in other cases small twist angles across the grain boundaries will not inhibit crack growth at all (Zhai et. al., 2006). The influence of the angle of twist can potentially explain observations of short cracks 1) not experiencing any retardation, 2) experience decelerations followed by a surge of crack growth and 3) complete crack arrest. While the model works well in highly textured materials that exhibit a large degree of crystallographic crack growth, the validity of the model in low texture materials has not been evaluated thus far.

In another paper by Zhai and coworkers (2005) analysis of fracture surfaces of 2026-T351 aluminum alloy showed crystallographic crack propagation similar to that present in the 8090 alloy. As such, the crystallographic model proposed in previous section could also be applied to Al-Cu-Mg alloys as well (Zhai, et. al., 2005). Further analysis on 8090 aluminum lithium alloy determined that Goss type grains were less likely to

allow crack propagation across the grain boundaries than Brass type grains. The crystallographic model developed in the 2000 paper by Zhai and coworkers was utilized to explain the observed results. A simple simulation was developed to calculate the tilt angles between the Brass and Goss grains with respect to randomly oriented adjacent grains. The analysis showed that the twist angle was within 5 degrees with respect to a random grain about 20.3% and 16.9% of the time for Brass and Goss type grains (Zhai et. al., 2005). This result shows a reduced probability for a Goss grain to propagate a crack across the grain boundary, which increases the likelihood of crack arrest. Since short crack growth is highly dependent on texture as shown by the model, such results could be used to develop texture within an aluminum alloy that will increase the chance of arresting or severely retarding short crack growth (Zhai et. al., 2005). Such material forming could easily increase fatigue resistance without resorting to more expensive methods.

In a paper by Liao (2010), a modified dislocation based crack tip opening displacement (CTOD) model originally developed by Tanaka et. al. (1989, 1992) was used to predict crack growth of short fatigue cracks in 2024-T351 aluminum alloy. The model is coupled with a Monte Carlo simulation to generate short crack growth predictions for various initial crack growth conditions such as microstructural properties and stress states. Crack growth rate da/dN is computed as a function of CTOD, where CTOD is determined by calculating the dislocation distribution along

the crack plane based on the continuous distributed dislocation theory (CDDT) (Liao, 2010). Crack growth is assumed to be along a slip band with the highest resolved shear stress. During crack growth the slip band zone is also increasing until it encounters a grain boundary. The slip bands are stopped at the boundary and eventually propagate into the adjacent grain as the crack length increases. The severity of impingement depends on the degree of misorientation between the neighboring grains (Liao, 2010). The state of slip bands is described by the following sequence: the slip band is in equilibrium when c<a denoted (ESB), slip band is blocked when c=a (BSB) and the slip band propagates when c>a (PSB) where c and a are half length of slip bands and crack, respectively. In all the above mentioned cases, the CTOD is obtained by integrating the dislocation density function D(x) which yields the following expressions

$$CTOD = \left(\frac{\sigma}{\pi^2 A}\right) g(x; c, a) \text{ for ESB} \quad (2.24)$$

$$CTOD = \frac{\beta\sigma}{\pi A}\sqrt{(c^2 - a^2)} + \frac{2a\sigma_j^f}{\pi^2 A}\ln\left(\frac{c}{a}\right) + \sum_{k=j+1}^{n}\frac{\left(\sigma_k^f - \sigma_{k-1}^f\right)}{\pi^2 A} g(a; c, L_{k-1}) \text{ for BSB}$$

(2.25)

$$CTOD = \frac{1}{\pi^2 A}\left[2a\sigma_j^f \ln\left(\frac{c}{a}\right) + \sum_{k=j+1}^{n}\left(\sigma_k^f - \sigma_{k-1}^f\right) g(a; c, L_{k-1})\right] \text{ for PSB} \quad (2.26)$$

$$K^m = \pi A\sqrt{2\pi}\lim_{x\to c}\left[\sqrt{c-a}D(x)\right] \quad (2.27)$$

For the BSB and PSB cases, the crack is assumed to be in one grain but the slip bands propagate into the adjacent grain, which gives rise to the summation symbols in equations 2.25 and 2.26. The expression for $g(x; c, a)$ is rater long and results from the integration of D(x). The stress

components σ and σ_f are the applied load and dislocation frictional stresses respectively. K^m is the microscopic stress intensity factor which governs the slip band propagation into the adjacent grain when $K^m > K_c^m$. Parameter K_c^m is regarded as the grain boundary energy that needs to be exceeded in order for crack propagation to continue (Liao, 2010). The above expressions are applicable for macroscopic loads below yield strength. The Tanaka-Mura model surmised above was augmented to account for global plasticity. The expressions for CTOD due to plasticity are given below.

$$CTOD_{plastic} = 4(1-\nu^2)\sqrt{a^2-c^2}\Delta\varepsilon_p \text{ for BSB (2.28)}$$

$$CTOD_{plastic} = \frac{4(1-\nu^2)}{\pi} \bullet F1 \bullet F2 \bullet \Delta\varepsilon_p \text{ for PSB (2.29)}$$

The total CTOD is given by $CTOD_{total}=CTOD_{elastic}+CTOD_{plastic}$. Expressions for F1 and F2 are rather long and are omitted for sake of brevity and v is Poisson's Ratio. Finally, crack growth rate is given by $da/dN=\alpha(\Delta CTOD)^{\beta}$ where α indicates fraction of CTOD responsible for crack growth and β is a material constant (Liao, 2010).

Because crack growth is highly affected by distributions of material properties that govern crack growth (grain size, initial crack size, misorientation etc…), Monte Carlo simulation was used incorporating the modified CTOD model. Monte Carlo simulation had four inputs defined by lognormal density functions that include grain size, initial crack size (initial size of fractured inclusions), friction stress σ_f and K_c^m. The first two

distributions could be gathered by direct observation of material samples. The latter two inputs were numerically calculated by best fitting test data from the AGARD study. The crack was assumed to grow in the S direction of the samples. About a 1000 simulations were conducted and compared to AGARD experimental results, as can be seen in Figure 2.5.

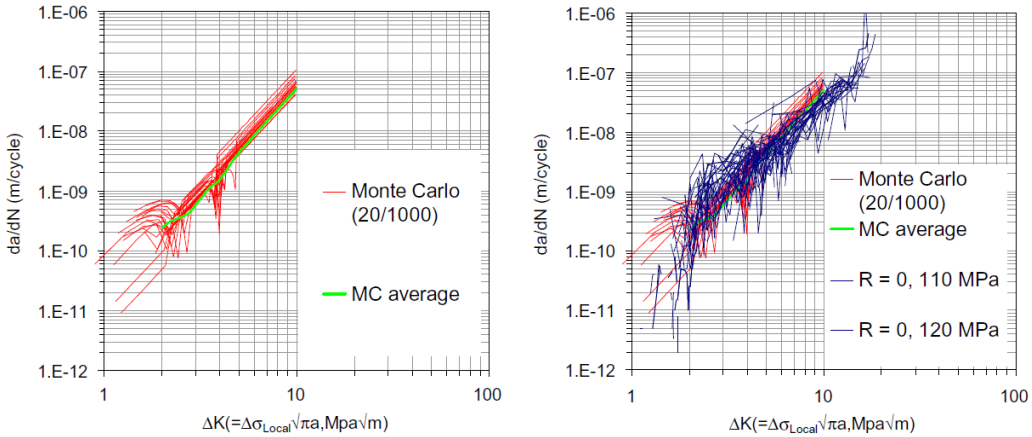

Figure 2.5: Comparison between Monte Carlo simulations and AGARD experimental data for growth of short and long crack regimes (Liao, 2010).

The model is capable of simulating crack retardations in the short fatigue crack regime; however, no crack arrest was present in this model, which is most likely due to the fact that the friction stress and K_c^m were fitted to the experimental data. This omitted any crack arrests in the final presentation. Moreover, the model seems to over predict crack growth at larger crack sizes, which could indicate the limitations of the model in the crack growth region mainly driven by LEFM concepts. Additionally, this model was run using material data for 2024-T351 alloy; however, the AGARD studies were done on 2024-T3 alloy. As such it is not clear whether these predictions are even valid for the T351 temper

All of the studies discussed thus far only dealt with uniaxially loaded fatigue tests. Works presented in the next section deal predominantly with long fatigue crack studies of aluminum plates. Nevertheless, since the present study is incorporating biaxial samples for the study of fatigue performance of Al-2024-T351, a brief discussion on aluminum alloy response to biaxial fatigue loading is warranted.

2.5 Effect of Biaxial State of Stress of Crack Growth

Biaxial study was performed by Liu et. al (1979). on 7075-T7351 and 2024-T351 aluminum alloy using center cracked panel (CCP) and cruciform geometry. The aim of the study was to evaluate the effects of biaxial stress states on cyclic crack growth behavior. Tests were conducted at varying stress amplitudes and R ratios. Additionally, effects of biaxiality were also evaluated by varying the stress ratio $\frac{\sigma_y}{\sigma_x}$. As a benchmark, numerous CCP and cruciform samples were tested under a uniaxial state of stress (i.e. σ_x=0) to gather crack growth data to use as a benchmark (Liu et. al., 1979). For similar materials and stress amplitudes no effect on fatigue crack growth was observed due to varying biaxial stress ratios. Moreover, elastic K factors were found to correlate well with crack growth data under biaxial stresses. While the plastic zone size and shape varied as a function of stress ratio, this appeared to pose no effect on the crack growth rates (Liu et. al., 1979). While the study was mainly concerned with long crack growth, the data obtained still hold value in that

future experiments using similar biaxial samples could be performed to analyze the above mentioned effects on short crack growth.

Donnelly and Nelson performed uniaxial and biaxial fatigue experiments on 7075-T6 aluminum alloy. The samples were loaded in the longitudinal direction at multiple strain amplitudes. The aim of the study was to determine the effects of biaxial state of stress and differing strain amplitudes of crack growth of short fatigue cracks. Biaxial samples were tested in a cantilever bending configuration. The samples had a large width to thickness ratio that gave rise to a tensile transverse stress component in the direction of the crack growth. The longitudinal stresses were mainly constant across in the center section and reduced slightly toward the specimen edges. The transverse stress component was highest in the middle of the specimen and reduced to zero at the sample ends. Cracks nucleated in the center section of the sample mainly due to inclusions. Early crack growth experienced high levels of crack retardation, which became alleviated as crack length increased (Donnelly and Nelson, 2002). Rotating bending specimens were also incorporated to generate crack growth data for uniaxial stress fields that were used for comparison. Evaluation of the data revealed higher short crack growth rates for biaxial samples compared to uniaxial samples. The difference in growth rates was exacerbated at higher strain amplitudes (Donnelly and Nelson, 2002). Studies of the uniaxial samples revealed no microstructural effect on crack growth. This was contributed to the alternating behavior of

grain geometry where at 0º spot grains were 60 μm long and 25 μm deep, conversely at the 90º spot grains were 25μm long and 60 μm deep.

In closing, large amount of work has been performed to understand the effects of material morphology on crack nucleation and propagation of short cracks in rolled Al plates. (Grosskreutz and Shaw; 1965, Pearson, 1975; Kung and Fine, 1979; Lankford, 1982; Newman and Edwards, 1988). The work performed however, looked predominantly at fatigue response in the longitudinal samples and failed to look at the global anisotropy effects on material fatigue response. Those studies that looked into anisotropy effects observed mainly the variability of fatigue life with respect to material directions, types of crack nucleation mechanisms and overall response of short crack growth in different material directions. (Morris et. al. 1976; Zabett and Plumtree, 1995; DeBartolo and Hillberry, 1998). Other studies observed the impact of global anisotropy on particle and grain geometries but failed to perform actual fatigue tests in any other material directions besides the longitudinal direction (Brockenbrough et. al., 1993; Liao et. al., 2008; Liao, 2009). Finally literature on anisotropy effects in Al 2024-T351 is severely lacking. In the present study attempts are made to quantify the effects of global anisotropy on particle and grain morphologies. Moreover, actual fatigue tests are performed in both longitudinal and transverse directions to directly observe the change of material response in fatigue loading due to rolling induced anisotropy and attempt to explain them based on local alloy morphology. Additionally,

cruciform samples with a center notch will be used to directly observe the impact of local and global anisotropies on short crack nucleation and propagation along with any possible interaction between the two.

CHAPTER 3

EXPERIMENTAL PROCEDURES

Aluminum 2024-T351 was used to investigate the role of global and local material anisotropy along with grain and constituent particle morphology on fatigue crack nucleation and short crack propagation. Both Uniaxial samples (dogbones) and biaxial samples (cruciforms) used in this study were fashioned from 0.25” Al 2024-T351 plates. All of the dogbone specimens along with 5 cruciform specimens were manufactured from a single Al 2024-T351 plate along with 2 cruciforms that were manufactured from a Al 2024-T351 plate supplied by the ASU machine shop. Prior to fatigue testing of either the dogbones or the cruciforms, samples were polished to insure that crack nucleation sites are clearly identifiable. All of the cruciforms and a select few dogbones went through EBSD analysis prior to fatigue testing. EDS analysis was performed on all tested samples to determine the chemical composition of failure causing inclusions.

3.1 Material

All experimentation was carried out on an Al-2024-T351 0.25” thick aluminum plate. This aluminum alloy contains copper and magnesium as one of its major alloying elements, for a full chemical composition reference AMS 4037 or AMS 4120R. As per AMS 4120R, the T351 condition is attained by performing a solution heat treatment followed by cold working via rolling and finally naturally aging the alloy. Tensile properties given by MIL handbook 5H for both the longitudinal and

transverse directions are 50,000 PSI (345 MPa) and 44,000 PSI (304 MPa) for yield strength and a ultimate strength of 66,000 (455 MPa) for both L and T orientations respectively.

Al 2024-T351 was chosen for the study since it is a suitable material to work with due to its lengthy service in the industry as well as being a subject of many previous scientific studies in past decades (Fowles, 1961; Swanson, 1960; Kusubov and van Thiel, 1969; Cleland and Prepost, 1965; Giuntoli et. al., 1959; Teale, 2009). More specifically, it has been used extensively in the aerospace industry due to its desirable damage tolerance characteristics along with a favorable strength to weight ratio which is typical of many aerospace materials. As is the case with countless other aluminum, titanium, nickel and cobalt alloys, Al-2024-T351 is a precipitation (age) hardened alloy. In its aged condition, Al 2024 forms second phase particles that act to strengthen the alloy by retarding the movement of defects and/or dislocations in the material under a stressed state. Consequently, it is these second phase particles that act as crack nucleation sites (Zabett and Plumtree, 1995; Morris et. al., 1976; Lankford, 1982); however, more detailed discussion will be presented in the results section. Since Al 2024 is manufactured in the same fashion as many other age-hardened aluminum alloys, Al 2024 can be treated as a model material since it behaves similarly to newer generations of aluminum alloys. As such, its behavior under certain stress states can be extrapolated to other more contemporary aluminum alloys.

To verify material properties of the 2024-T351 plate used for this study both tensile testing and low cycles fatigue tests were performed. Five 0.25” thick dogbones samples were tensile tested in both longitudinal and transverse directions. Dogbone dimensions are similar to the ones found in figure 3.1 except no notches were present and the specimen thickness is 0.25”. Tensile testing procedure followed is in accordance with ASTM E8-09 specification which outlines tensile testing requirements for metallic materials. Same specimens were used for low cycle fatigue tests. Tests were performed with a max load of 3200 lbf and R=-1 at a frequency of 5Hz. Samples usually lasted approximately 20,000 cycles to failure. Three samples with the first cycle in tension for longitudinal and transverse directions were tested to create hysteresis loops used to evaluate the material hardening response. Additionally, one sample of each orientation was also tested with the initial cycle in compression in order to quantify the Bauschinger effect in the material.

3.2 Uniaxial Samples

Dogbone samples were used to gather statistical data on fatigue performance of Al 2024 in the longitudinal and transverse directions. Along with statistics, the dogbones were used to evaluate the effect of constituent particle chemistry on crack nucleation. Notches were introduced into the dogbones in order to create a well defined region of maximum stress where crack nucleation processes could be observed. Dogbone dimensions are shown in Fig. 2.1.

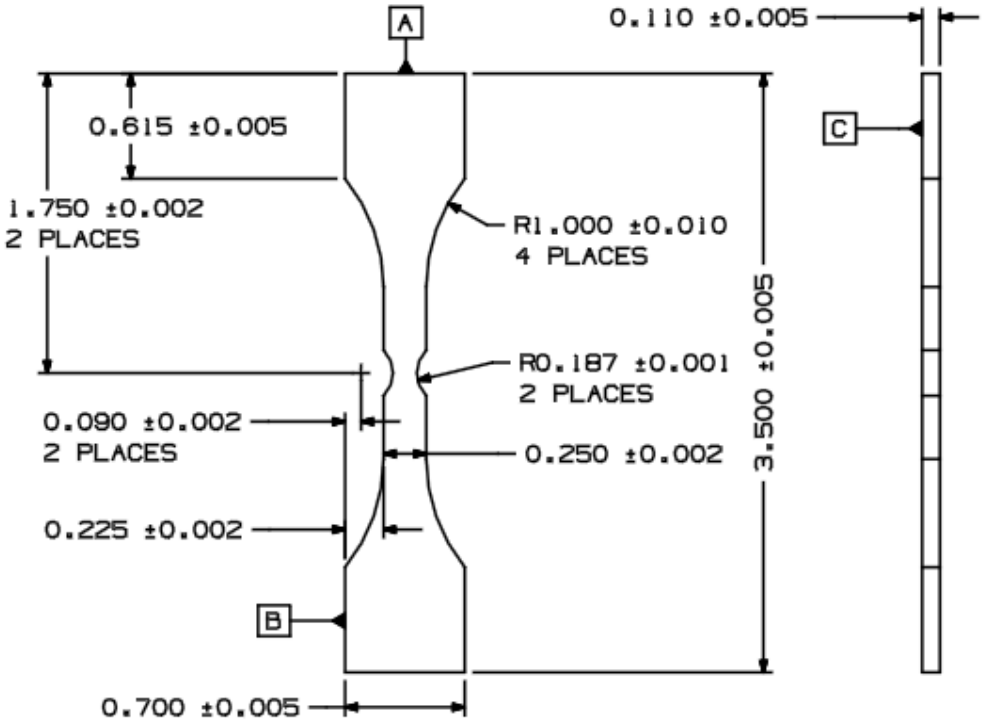

Figure 3.1: Dimensional data for the dogbone. Drawing interpretation is per ASME Y14.5.

Dogbone samples were cut from a single Al 2024-T351 plate at the ASU machine shop. The uniaxial samples were cut in both longitudinal and transverse directions of the plate where longitudinal is parallel to the rolling direction. As depicted in the figure above, the root of the notches is the location where crack nucleation observation and study occurred. The dimensions of the dogbone were constrained by the chamber dimensions of the electron microscope used in this study and the geometry of the servo hydraulic load frame used for the fatigue testing. The dimensions above allowed for sample placement into the SEM chamber where imaging, EDS and EBSD analysis were performed while still being of adequate size to be tested in the load frame.

3.2.1 Uniaxial Sample Preparation

Before the fatigue testing, uniaxial samples were polished to remove any existing damage and machining marks to insure that crack nucleation occurred due to intrinsic material flaws and to facilitate monitoring of crack nucleation and propagation. The samples were polished on both sides and inside the notches. A hand polishing wheel was used to polish the sides of the dogbones. The polish procedure started with the 600 grit paper and ended with either 0.05 or 0.04 μm colloidal silica. Deionized water served as a lubricating media throughout all the polishing steps. Table 3.1 outlines the polishing procedure used on the face of the dogbones.

Table 3.1: Polishing procedure for the sides of the dogbones.

Procedure Steps	Polishing Media	Lubricant	Time per side
1	600 grit SiC paper, 8" adhesive back disk	DI Water	10 Minutes
2	800 grit SiC paper, 8" adhesive back disk	DI Water	10 Minutes
3	1200 grit SiC paper, 8" adhesive back disk	DI Water	10-15 Minutes
4	Either 0.05 or 0.04 μm colloidal silica on a Vel-Cloth adhesive back 8" polishing disk	DI Water	5-10 Minutes

All of the steps outlined above were performed on a hand polisher. Six hundred grit paper was used to clean up all the previous dings, scratches and machining marks. The sample was rotated 180 degrees about the axis perpendicular to the face of the dogbone every 1-2 minutes in order to insure even material removal. Next, 800 grit paper was used to remove

the scratches from the 600 grit polishing step. As with the 600 grit paper, the sample is rotated 180 degrees every 1-2 minutes to insure even material removal. After 800 grit, 1200 grit was used to remove scratches even further. At this stage the material removal is very small as the 1200 grit paper is mainly polishing the dogbone faces, while the sample was still rotated; it is only warranted every 2-4 minutes since material removal is minimal. For the final step, either 0.04 or 0.05 μm colloidal silica can be used as described in Table 3.1. Following this polishing procedure almost all scratches were removed revealing clear a distinction between the matrix and second phase particles. Figure 3.2 shows the surface finish produced by polishing procedure described above.

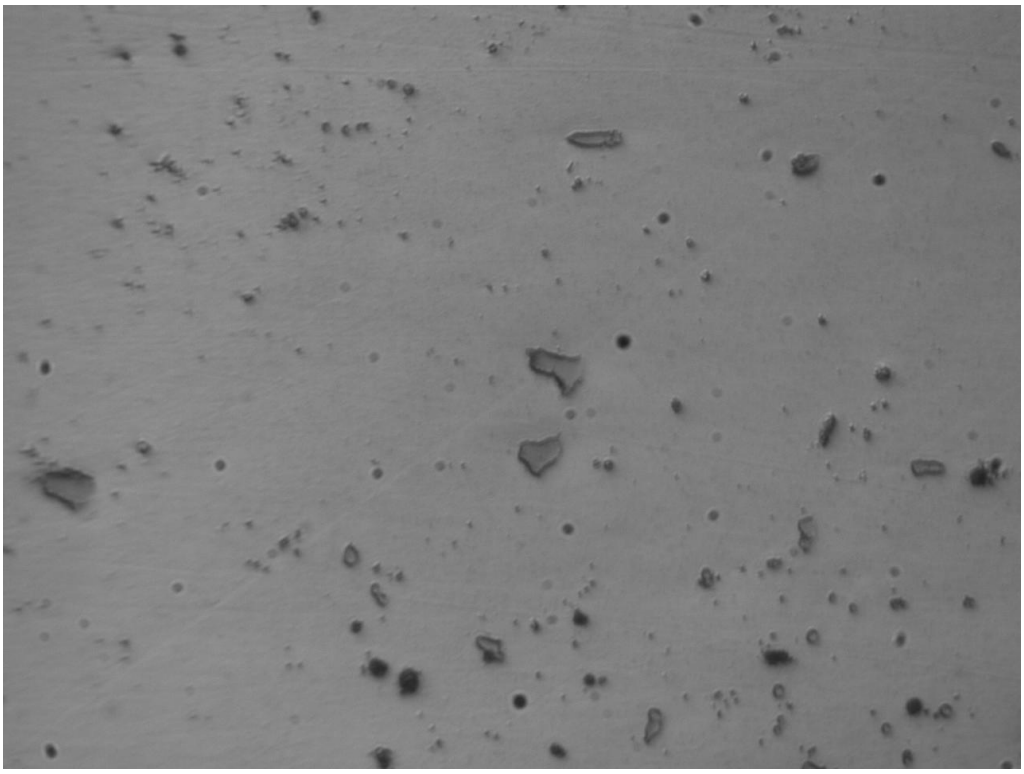

Figure 3.2: Optical microscopy picture at 20X showing the surface finish of the uniaxial samples. Note the second phase particles surrounded by the matrix.

The polishing procedure for the notches is similar to that of the faces except that either a CNC or a manual mill were used to polish the them. A 0.287” diameter gage pin is placed in the mill chuck. A 1” square piece of either sandpaper or Vel-cloth can then be wrapped around the gage pin and reinforced with a piece of tape in order to prevent the sandpaper from unwrapping. Once the gage pin with either sandpaper or Vel-cloth is placed into the mill, the polishing procedure for the notch can begin. As with the face polish, the notch polish is started with the 600 grit paper in order to remove all the machining marks and finished with either 0.04 or 0.05 μm colloidal silica. The polishing procedure for the notches is outlined in Table 3.2.

Table 3.2: Polishing procedure for the dogbone notches.

Procedure Steps	**Polishing Media**	**Lubricant**	**Time per side**
1	1” square of 600 grit SiC paper with adhesive back.	DI Water	5 min max
2	1” square of 800 grit SiC paper with adhesive back.	DI Water	5-10 minutes
3	1” square of 1200 grit SiC paper with adhesive back.	DI Water	5-10 minutes
4	1 μm suspended alumina on a 1” square Vel-Cloth with adhesive back.	DI Water	5-10 minutes
5	Either 0.05 or 0.04 μm colloidal silica on a 1” square Vel-Cloth with adhesive back.	DI Water	5-10 minutes

The spindle speed set on the mill was between 60-70 RPM for all the steps. Six hundred grit paper was used to remove all the machining marks and remaining steps gradually worked the surface finish to mirror quality. The dogbone needed to be rotated every 180 degrees about the axis coming out of the notch in order to prevent tapering of the notches. The dogbone needed to be rotated every 1-2 minutes when polishing with 600 and 800 grit papers and it is recommended to continue rotating the sample in a similar fashion when polishing with steps 3-5 outlined in Table 3.2 to insure a quality finish. Figure 3.3 shows the quality of the polishing surface finish described above along with the mill set-up used to polish the notches.

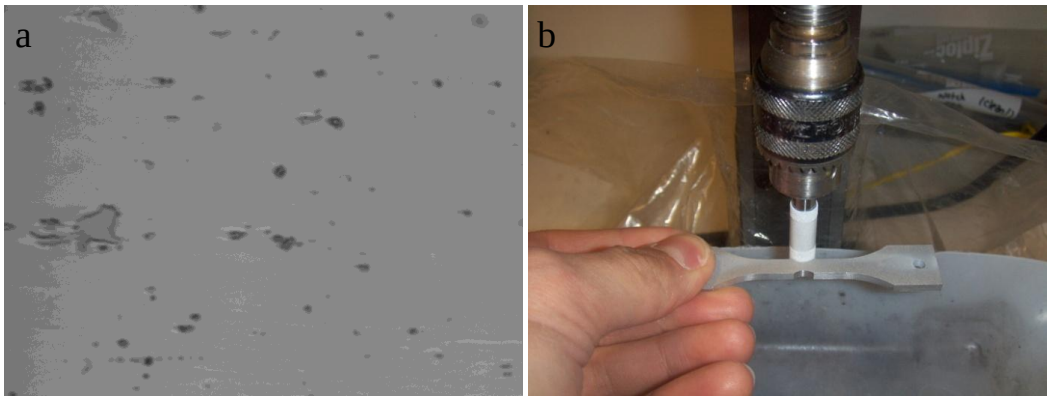

Figure 3.3: Optical microscopy picture at 20X showing the surface finish of the uniaxial notches (a). It's clear to see second phase inclusions surrounded by the matrix. Setup for polishing using the mill (b).

All of the polishing procedures described above are adequate for monitoring and recording crack nucleation and propagation during the fatigue testing process; however it is insufficient to produce EBSD (Electron Backscatter Diffraction) scans needed for this study. As mentioned above, a few of the dogbones were selected for EBSD

scanning prior to fatigue testing in order to study the effects of grain orientations on the crack nucleation under uniaxial loading. The polishing procedure was similar to that described in Table 3.2 except steps 3, 4 and 5 took additional time to complete. Moreover, step 5 required the use of the CNC mill, which was numerically programmed to polish the notches of the dogbones using a spring loaded fixture to control the loads on the notch surface during polishing. Table 3.3 describes the polishing procedure of the notches that undergo EBSD scanning.

Table 3.3: Polishing procedure for the dogbone notches for EBSD scans.

Procedure Steps	Polishing Media	Lubricant	Time per side
1	1” square of 600 grit SiC paper with adhesive back	DI Water	5 min max
2	1” square of 800 grit SiC paper with adhesive back	DI Water	5-10 minutes
3	1” square of 1200 grit SiC paper with adhesive back	DI Water	10-15 minutes
4	1 μm suspended alumina on a 1” square Vel-Cloth with adhesive back	DI Water	10-15 minutes
5	Either 0.05 or 0.04 μm colloidal silica on a 1” square Vel-Cloth with adhesive back	DI Water	60 minutes, times 2

The CNC program is set to run for 60 minutes at which time the sample is rotated about an axis perpendicular to the notch and then the polishing procedure is repeated for another 60 minutes. After the 120 minutes of polishing with colloidal silica, the plastic deformation at the surface which

obscures the EBSD patterns is significantly removed revealing grain orientations. Such a high quality polish is warranted for this case since the EBSD technique probes only the top 10-50 nm of the surface (Li, 2006; Schwartz et. al, 2000). The polishing fixture incorporates linear slides that control the force applied to the sample in both X and Y axes. The spindle speed remains between 60-70 RPM for all the steps outlined in Table 3.3. Figure 3.4 shows the spring loaded fixture stand by itself and also when fixtured into the CNC mill.

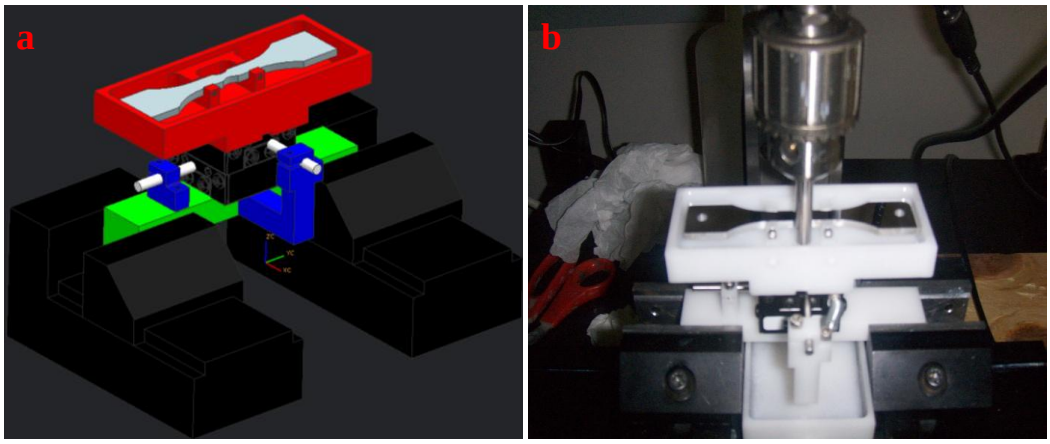

Figure 3.4: Spring loaded polishing fixture with the dogbone secured inside the tub (a). Polishing fixture secured in the CNC mill ready for the polishing sequence to start (b).

3.2.2 Uniaxial Sample Characterization

Within the capabilities of a scanning electron microscope (SEM), EBSD was used extensively to characterize the microstructure of the dogbone samples before fatigue testing in an attempt to understand the impact of microstructure on crack nucleation and propagation properties of Al 2024-T351. The microscope used for the characterization of the material microstructure is Tescan Vega SEM which is equipped EBSD

capability. More specifically, Tescan Vega is equipped with a DigiView 1612-FW high resolution digital camera which runs at 58pps (indexed patterns per second), as well as TexSEM Laboratories (TSL) data collection and analysis software version 5.31 OIM^{TM}.

Electron backscatter diffraction is used to map the grain orientations of a point on the surface of the subject sample. The sample is placed into the chamber of the SEM (in this case Tescan Vega) and tilted to 70 degrees about the Y-axis of the stage. As the electron beam emanating from the pole piece hits the sample surface, the electron beam interacts with the atomic planes in the sample and is subsequently reflected by them. The interaction between the electron beam and the atomic planes follows Bragg's Law, i.e.,

$$n\lambda = 2d \sin\theta \qquad \text{Eq. 3.1}$$

where n is an integer, λ is the wavelength of the incident electron beam as determined by the acceleration voltage, d is the spacing between the atomic planes in the Al 2024-T351 lattice and θ is the angle between the incident electron beam and the scattering atomic planes (Julian, 2008; De Graef and McHenry, 2007; Sands, 1975; Guinier, 1963). The overlapping waves that are re-emitted by the atomic planes can either add or subtract from each other producing higher or lower intensity peaks, i.e., either constructive or destructive interference. The phase shift in the reflected beam due to change in angle θ is the primary culprit for constructive or destructive interference. Reflected electrons that satisfy Bragg's Law

radiate in diffraction cones from the front and back of the atomic planes. When the cones intersect the phosphorus screen of the detector, Kikuchi lines are formed. Each Kikuchi line on the phosphor screen belongs to a specific family of lattice planes. Although the electrons are diffracted in a cone shape, the lines appear straight on the phosphor screen because the cones are very shallow. Numerous Kikuchi lines are diffracted onto the phosphor screen which represents 3-D crystal structures in a 2-D projection (Li, 2006; Schwartz et. al, 2000). Kikuchi lines are indexed by the TSL software, which yields the crystallographic orientation of the material at that point where the electron beam hits the sample. This procedure is depicted in figure 3.5.

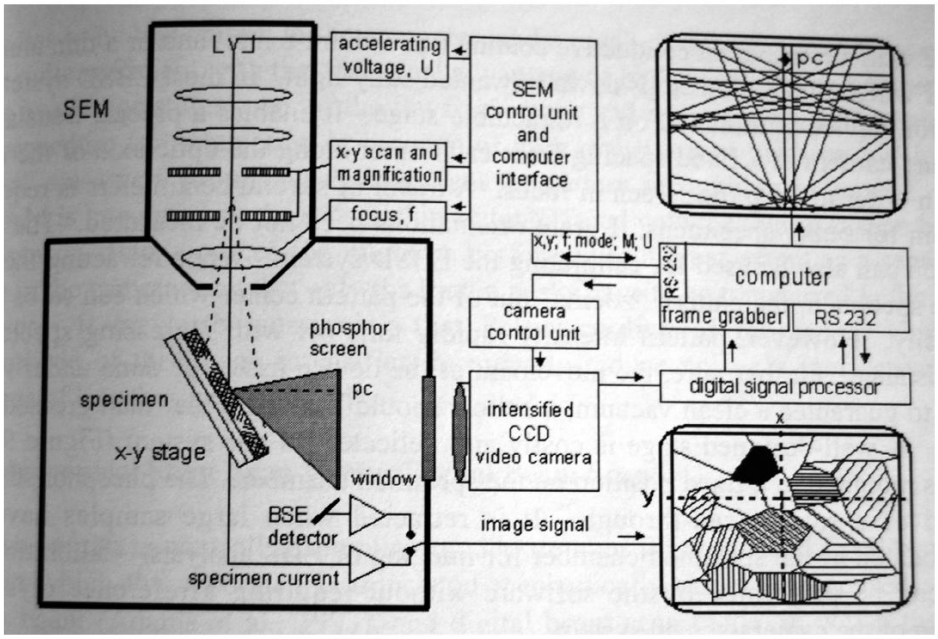

Figure 3.5: Schematic representation of the electron backscatter diffraction method (Schwartz et al, 2000)

Besides just indexing, the TSL software possesses a mapping function that is capable of scanning large areas of the material producing

maps of the grain orientations at specified step sizes. These maps can subsequently be used to generate grain orientation maps or inverse pole figure (IPF) maps, where the colors of the grains correspond to the crystallographic directions of the grains normal to the surface containing the scanned area. Moreover, grain size distributions, aspect ratio, image quality maps and texture maps were also created in order to characterize the microstructure and look for correlations between crystallographic data and crack nucleation sites. Figure 3.6 shows an EBSD scan on the notches of dogbone 8L, the curvature of the grains is due to the curvature of the notch.

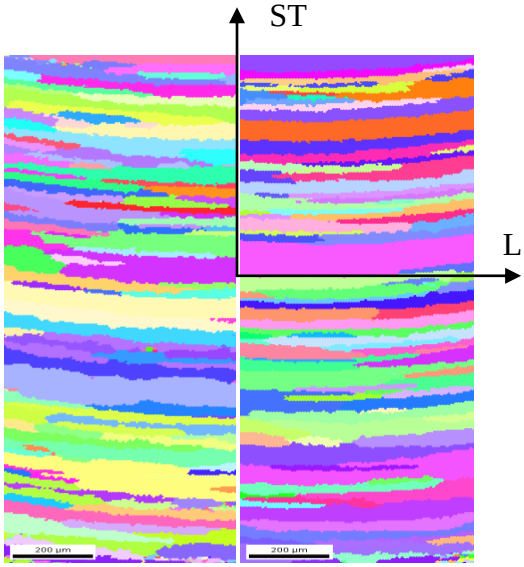

Figure 3.6: EBSD scan of the notches. ST stands for short transverse (Z-direction) and L stands for longitudinal (X-direction). The scale bar for both images is 200 µm.

Besides the EBSD capabilities, the microscope is also equipped with energy dispersive X-rays spectroscopy (EDS). EDS is used to characterize the chemical composition of the second phase particles. Results from previous studies indicate that iron rich inclusions seem to be

the major culprit for crack nucleation sites (Bower and Schijve, 1973; Pearson, 1975; Lankford, 1982; Payne, 2010). This is due to iron's embrittling effect that makes the inclusions more prone to fracture due to the surrounding stress field. Figure 3.7 shows some of the major alloying elements that are found in Al 2024-T351.

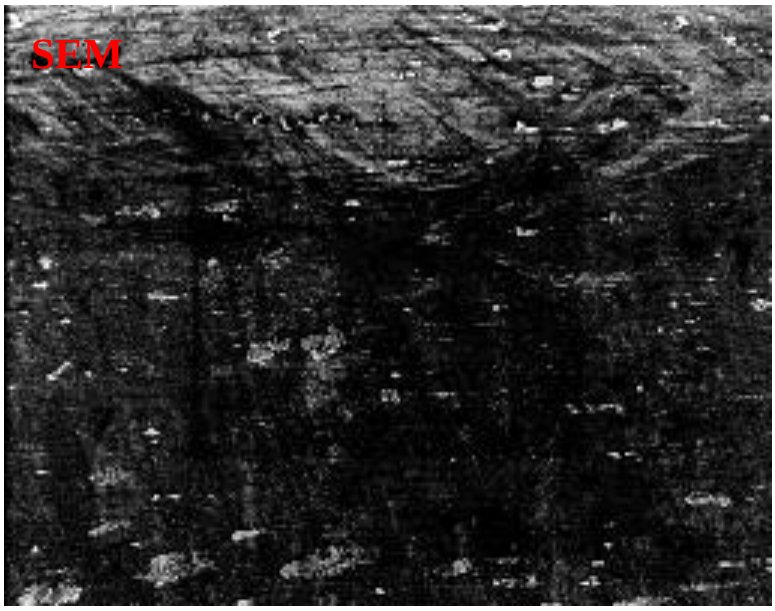

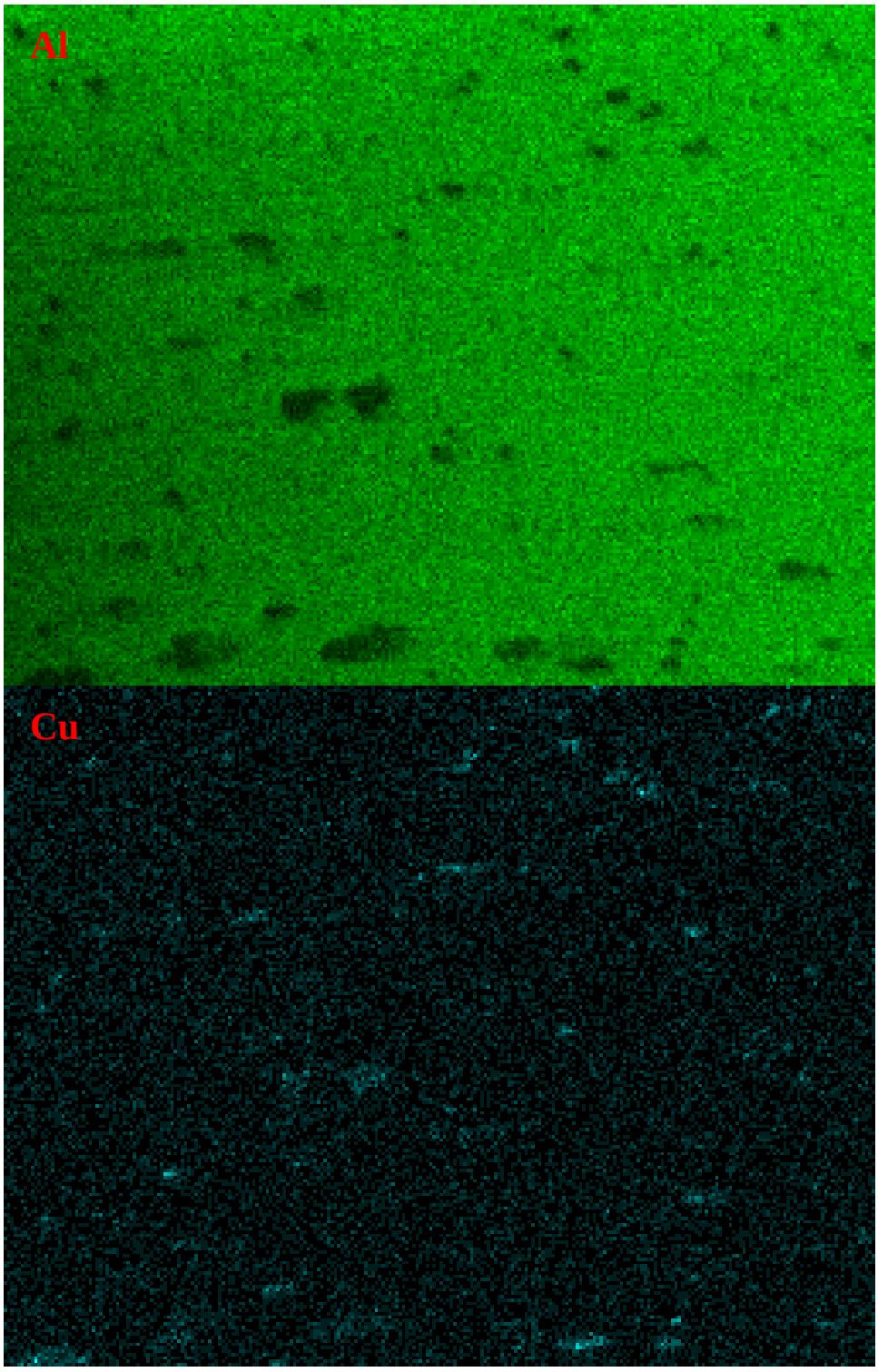
Al
Cu

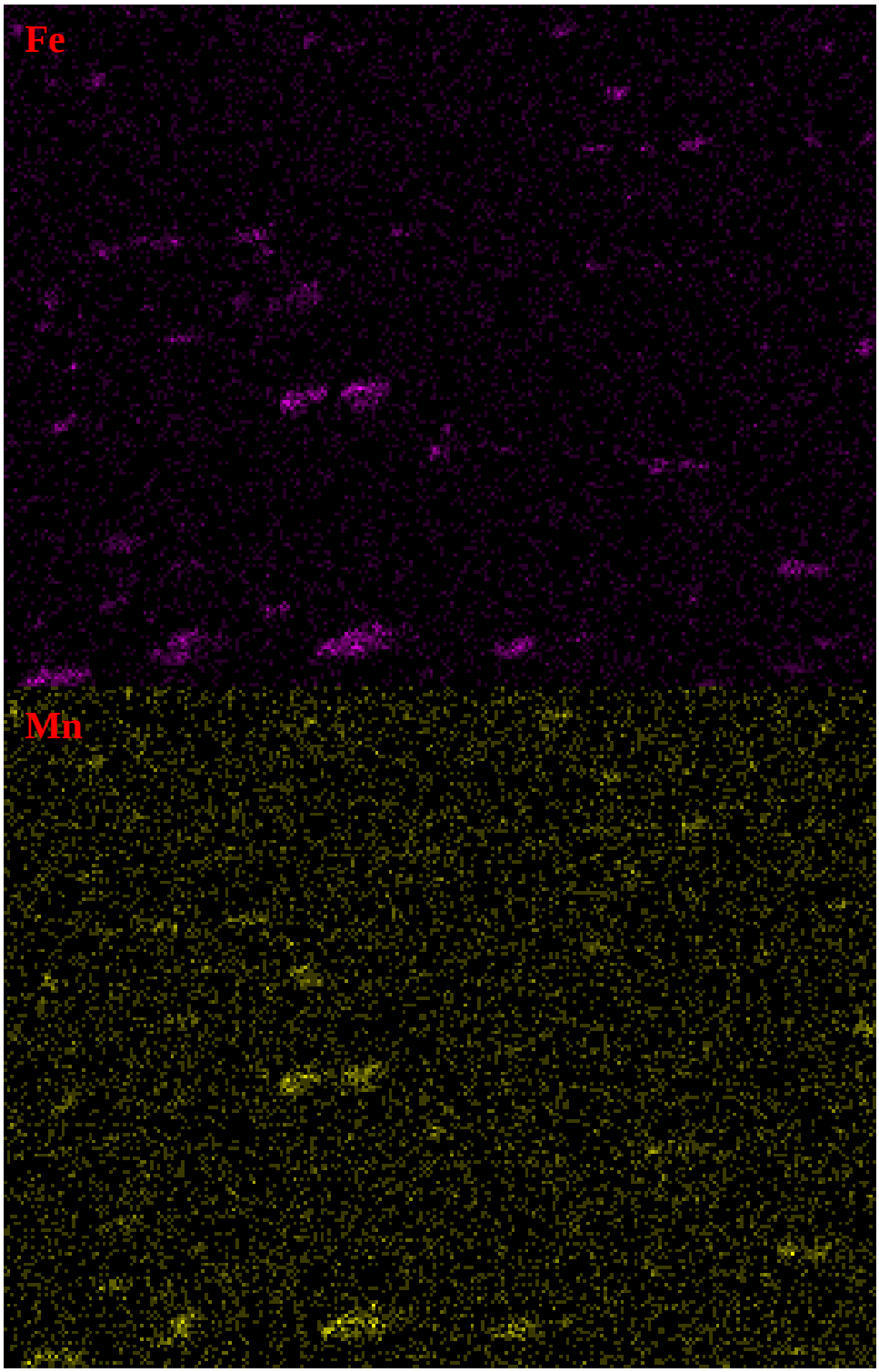

Figure 3.7: EDS scan of Al 2024-T351 showing the major alloying elements along with the parent metal aluminum. Figure shows the distribution of the alloying elements within the inclusions.

3.2.3 Uniaxial Fatigue Testing

The uniaxial samples were tested using Instron servo hydraulic load frame. All the dogbone samples were tested at the yield strength of Al 2024-T351. Since the yield strength varies between the longitudinal and transverse directions, two yield strength values were used depending on the material orientation of the dogbone with respect to the loading axis of the load frame. For the longitudinal samples the yield strength was 52 KSI or 363 MPa. Therefore the loads imposed on the longitudinal sample were designed to generate stresses at yield strength of the material at the tip of the notch. Correspondingly, the yield strength for the transverse samples was 49 KSI or 337 MPa and as for longitudinal samples, the loads imposed on the transverse samples were designed to generate stresses at that value at the tip of the notch. To ascertain the yield strength for the two orientations, 5 tensile tests were carried out for each of the orientations and averaged to give the values reported above. The range of the values for longitudinal and transverse yield strengths are 52700 ±1700 PSI and 48900±1200 PSI respectively.

Since the samples showed dimensional variations due to the machining process, the load required for each dogbone was calculated using the FEA method in order to insure each sample was tested at yield strength. After the polishing procedure, two measurements were taken. The first measurement was the thickness and the second measurement was the width of the dogbone across the two notches. These

measurements were used to build a CAD model of the dogbone using Siemens NX-7 software. Subsequently, the CAD model was meshed using the meshing tools found in the Advanced Simulation toolbox of NX-7. Following the meshing process, the meshed model was exported to NX-Nastran where the model was constrained and appropriate loads were applied. Finally the model was solved to predict the von-Mises stress generated in the notched region. The whole process was re-iterated until the appropriate load that generated stresses at yield strength at the notches was found. Figure 3.8 below shows the dogbone as it goes through its progression from CAD model to the meshed model and finally the solved model.

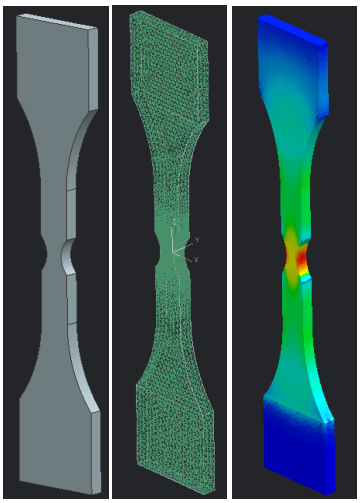

Figure 3.8: Progression of the dogbone model from a simple CAD model to the solved model.

Notice in the model that the mesh is finer in the notch region in order to obtain more accurate stress values at the notch where the stress concentration is present. The model was meshed using second order 3-D tetrahedral elements equipped with 10 nodes.

Once the load values were calculated for each specimen, the dogbones were placed into the load frame for fatigue testing. Cyclic loading was generated using a sinusoidal function at a frequency of 18 Hz with an R ratio of 0.100 where $R = \frac{Load_{min}}{Load_{max}}$. The fatigue test was interrupted every 5000 cycles to monitor for crack nucleating inclusions for later analysis. The sample was placed under an optical microscope and the entire area of both notches was examined for fractured inclusions and cracks that propagated into the matrix. Once damage was found, pictures were taken at 20X to document the area and crack causing inclusions for future study and analysis. The test was carried out until the fatigue crack reached a length of 1 mm.

3.3 Biaxial Samples

Biaxial samples (cruciforms) were used to evaluate the effects of grain orientation on crack propagation into the matrix of Al 2024-T351. The hole in the middle of the gage area allows for sampling of many crystallographic directions inside a grain that are susceptible to matrix crack propagation. At the surface of the hole, tensile uniaxial state of stress is present due to stresses tangent to the hole curvature. Away from the hole biaxial state of stress is present. The cruciform was designed such that the stresses around the hole are independent of angle about the hole. Therefore von Mises stress that is uniform around the hole is achieved. Because the stresses are uniform around the hole, cruciform samples allow for the evaluation of the effect that grain orientation has on

crack nucleation and initial propagation. It is evident from Fig. 2.8 that majority of inclusions contain iron in their chemical composition. As a result almost all the grains will contain fractured inclusions; however, only a select few grains will be subject to crack propagation into the matrix while other grains prevent crack growth into the matrix even though fractured inclusions exist. Cracks in the inclusions are caused by stress fields imposed during testing or are a result of the rolling process during the manufacturing stage of the material. Cruciforms were cut from two Al 2024-T351 plates. Two cruciforms were machined from the plate provided by the ASU machine shop and 5 cruciforms were machined from a plate from a different manufacturer. Cruciform dimensions can be seen in figure 3.9. The cruciforms were machined so that the longitudinal and transverse directions were with the applied loads, i.e., along the arms. The size of the cruciform was constrained by the EBSD procedure which calls for the sample to be inclined at 70 degrees about the Y-axis. In this position cruciforms were mere millimeters from the pole piece. Therefore great care was used when the cruciform was translated inside the SEM chamber.

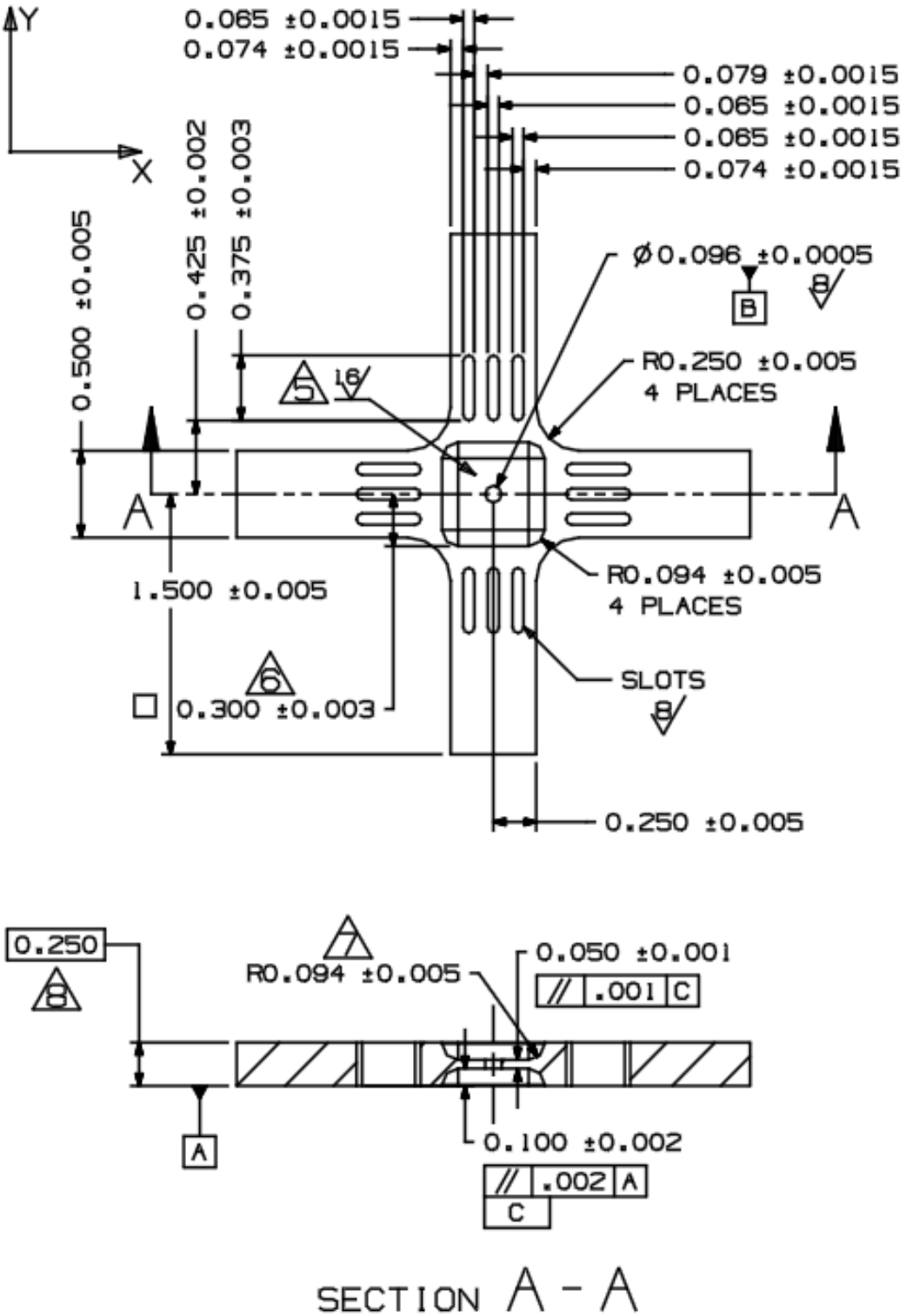

Figure 3.9: Dimensional data for the cruciform.

In order to insure a biaxial state of stress around the hole, swivel arms were used to cancel out any stresses due to bending that would arise from the misalignment of the sample in the testing grips. Prior to testing, both the hole and the gage area around the hole were polished. The gage area was further polished to EBSD quality with a CNC mill and EBSD analysis was performed to obtain the grain orientations around the hole prior to testing.

3.3.1 Biaxial Sample Preparation.

Before the cruciform samples were tested, the hole surface along with the gage area on both sides were polished in order to remove any previous damage and machining marks. The polishing procedure enabled for clear viewing of the crack nucleation and propagation phenomena along with material characterization with EBSD and EDS analysis. The hole was polished using a mini lathe while the gage area was polished using the CNC mill. Both the hole and the gage area were polished starting with 600 grit paper and ending with either 0.04 or 0.05 μm colloidal silica. Deionized water served as a lubricating media throughout all the polishing steps. Table 3.4 outlines the polishing procedure used on the hole of the cruciform.

Table 3.4: Polishing procedure for the cruciform hole.

Procedure Steps	Polishing Media	Lubricant	Time
1	0.200”X1.750” strip of 600 grit SiC paper with adhesive back.	DI Water	5 minutes
2	0.200”X1.750” strip of	DI Water	5 minutes

	800 grit SiC paper with adhesive back.		
3	5 μm suspended alumina on a small cotton swab.	DI Water	10 minutes
4	1 μm suspended alumina on a small cotton swab.	DI Water	10 minutes
5	Either 0.05 or 0.04 μm colloidal silica on a small cotton swab.	DI Water	10-15 minutes

For steps 1-2, the strips of the sandpaper are wrapped around a 0.050” gage pin, after which the pin is inserted into the hole of the cruciform while the cruciform is fixtured against the backplate of the lathe. The lathe rotation is set between 60-80 RPM. Figure 3.10 shows the cruciform fixed up against the backplate of the lathe.

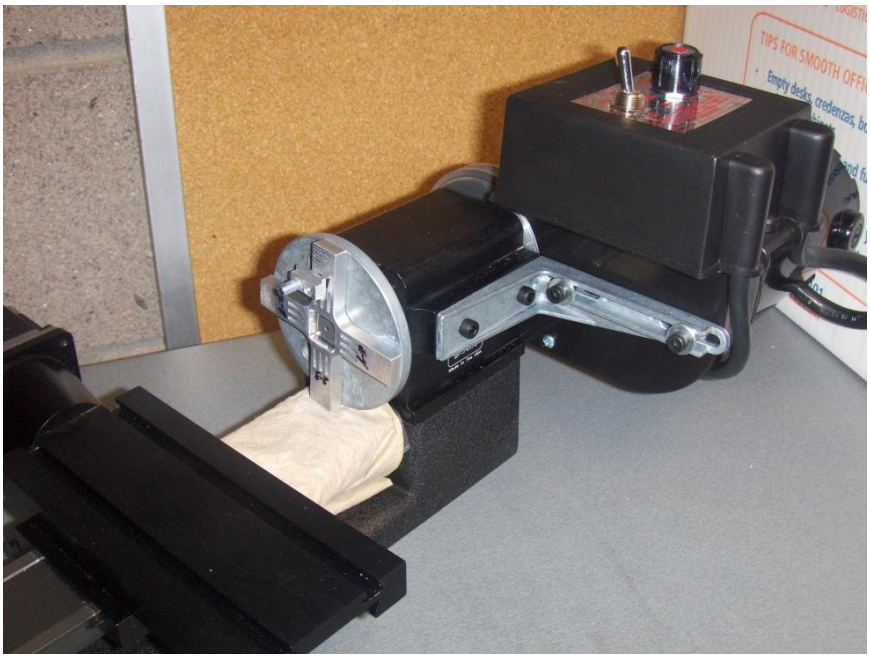

Figure 3.10: Picture showing the cruciform fixtured in the lathe.

The pin with the sandpaper was held manually in the hole and is linearly translated back and forth in the hole while the lathe is running in order to

insure even material removal. For steps 3-5 the procedure was similar except that a small cotton swab was used. The swab was dipped in the suspended alumina or colloidal silica mixture and the tip of the cotton swab was placed inside the hole. As with the gage pin, the swab was worked back and forth slightly as the lathe was running. Figure 3.11 shows the surface finish of the hole after the procedure is completed.

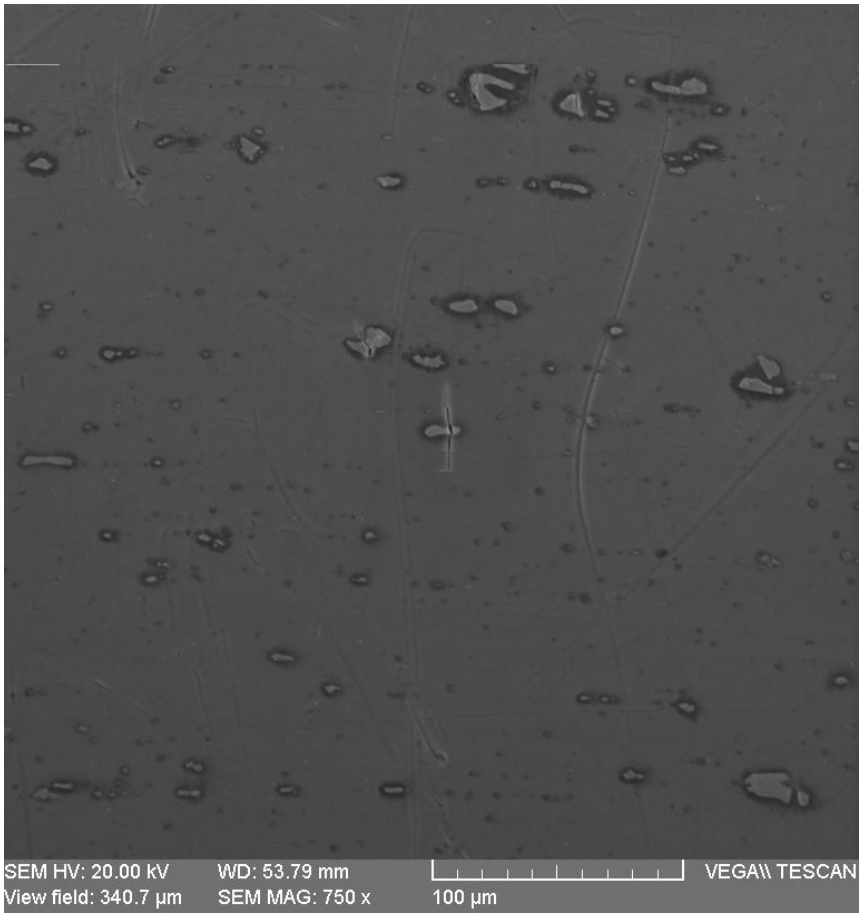

Figure 3.11: SEM microscopy picture depicting the quality of the polishing procedure used in the cruciform hole.

After the hole polishing procedure was completed, a CNC mill was used to polish both sides of the gage area. A CNC program was written to use a circular pattern to polish the gage area. The polishing needed to

yield a surface that could be characterized with a EBSD and/or EDS map and allow for the observation of crack nucleation and propagation phenomena during the testing phase. The polishing procedure is outlined in Table 3.5.

Table 3.5: Polishing procedure for the gage area of the cruciforms.

Procedure Steps	Polishing Media	Lubricant	Time per side
1	0.300” diameter 600 grit SiC paper with adhesive back.	DI Water	10 minutes
2	0.300” diameter 800 grit SiC paper with adhesive back.	DI Water	10 minutes
3	0.300” diameter 1200 grit SiC paper with adhesive back.	DI Water	10 minutes
4	5 μm suspended alumina on 0.300” diameter Vel-Cloth with adhesive back.	DI Water	10 minutes
5	1 μm suspended alumina on 0.300” diameter Vel-Cloth with adhesive back.	DI Water	10 minutes
6	Either 0.04 or 0.05 μm colloidal silica on 0.300” diameter Vel-Cloth with adhesive back.	DI Water	2 Hrs

Disks 0.300” diameter sandpaper or Vel-Cloth were punched out of their respective 8” diameter counterparts using a custom punch. The 0.300” papers were intended to fit into an in-house manufactured polishing bit used on the gage area. The polishing bit was then inserted into a spring loaded engraving tool that was used to control the amount of force exerted

on the gage area during polishing. Figure 3.12 shows the punch and the polishing bit engraving tool assembly.

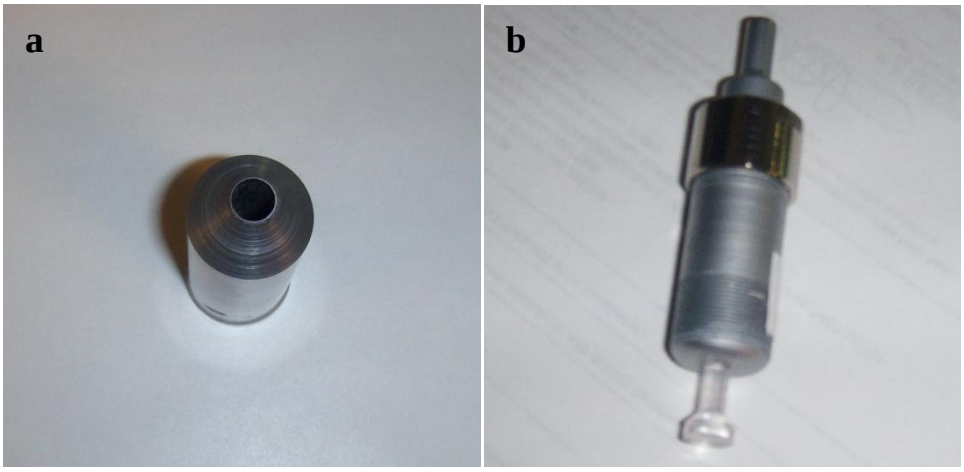

Figure 3.12: Hole punch used to create 0.300” diameter sandpaper segments (a). Engraving tool-polishing bit assembly where the punched sandpaper is placed at the bottom end of the polishing bit (b).

The engraving tool-polish bit assembly and cruciform were placed into the CNC mill. For steps 1-5 the spindle was set to 70-80 RPM. Step 6 was split into two 1 hour blocks where for the first hour the spindle speed was set to 70-80 PRM and for the second hour the spindle speed was set to 50-60 RPM. Figure 3.13 shows the polishing procedure in action.

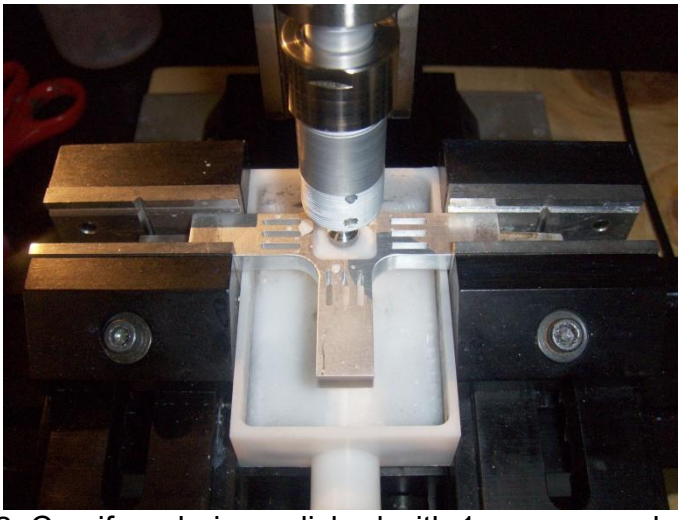

Figure 3.13: Cruciform being polished with 1 μm suspended alumina.

Figure 3.14 shows the surface finish of the gage area after the polishing procedure outlined in Table 3.5.

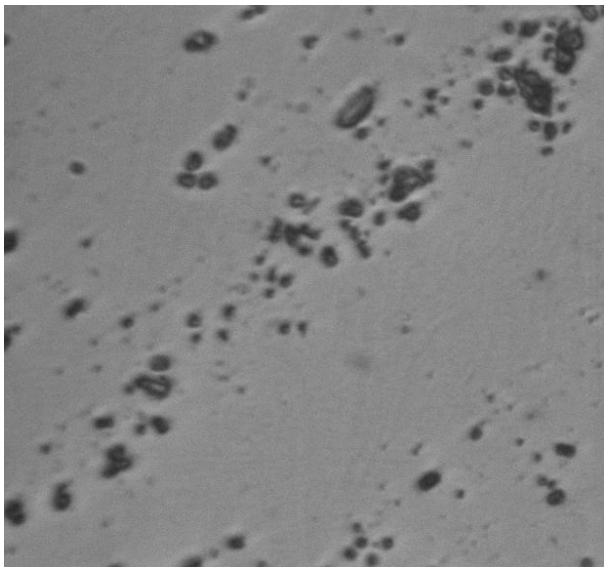

Figure 3.14: Surface of gage area after the polishing procedure outlined in Table 3.5.

3.3.2 Biaxial Sample Characterization

EBSD was extensively used for characterizing the microstructure of the cruciforms on the gage area near the hole. Characterization of the microstructure was done up to 1 mm away from the hole around the entire circumference. The entire EBSD map could not be completed in one scan; therefore, the area was partitioned into 8 smaller regions which were mapped individually. Subsequently the 8 independent scans were merged together to yield the entire map around the hole. Figure 3.15 shows a typical individual scan.

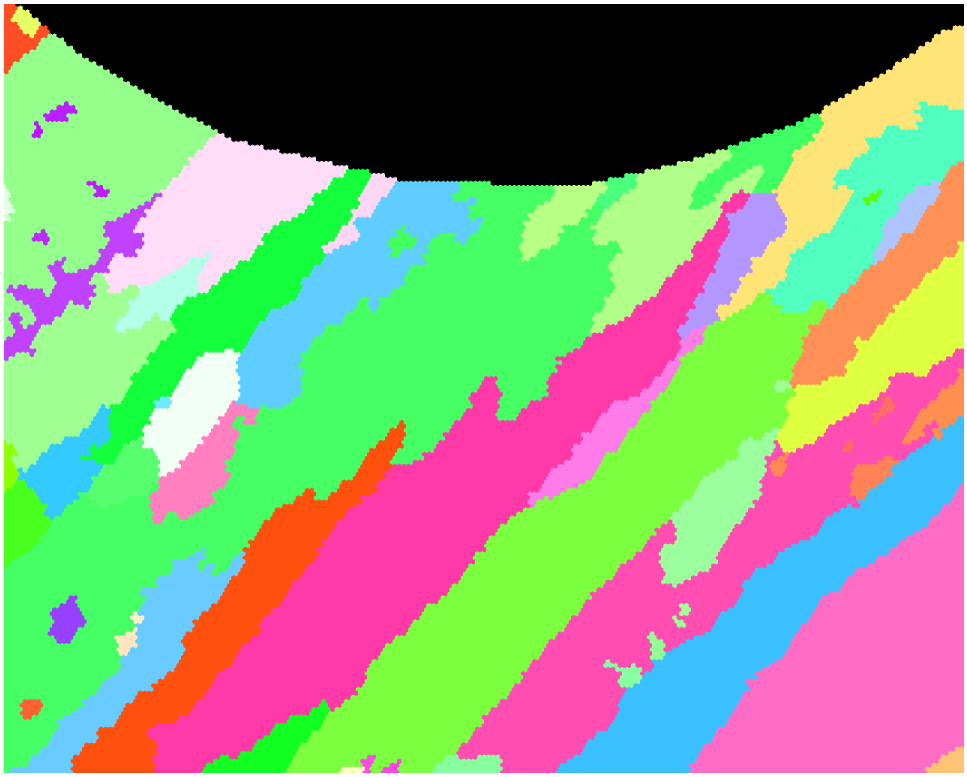

Figure 3.15: Figure of typical cruciform scan. Notice the rolling directions deduced from the elongated grains.

Looking at the EBSD map of the two sides it is easy to determine the rolling direction of the material. Since the sample was inclined by 70 degrees and the scan areas are quite large, there was a concern that working distance was deviating too much as the electron beam is rastering along the scan area. The change in working distance could potentially defocus the electron beam to the point where the indexed patterns would be incorrect. To minimize the possible deleterious effects of varying working distance, the SEM was always focused in the middle of the scan so as the electron beam was moving along the inclined axis the deviations in working distance would be minimized for the opposite ends of the scan area. Moreover, smaller local EBSD scans were performed on cruciform 4

and compared to their larger counterparts in order to see what effect the change in working distance had on the indexing patterns. Localized scans were performed at the opposite ends of the large scan area as these are the locations where working distance variations are greatest. Values of the rotation matrix were compared between the localized scans and large scan to verify the accuracy of the indexing software on the large scans. Figure 3.16 shows a large scan done at the bottom of the hole along with the localized scans at each end.

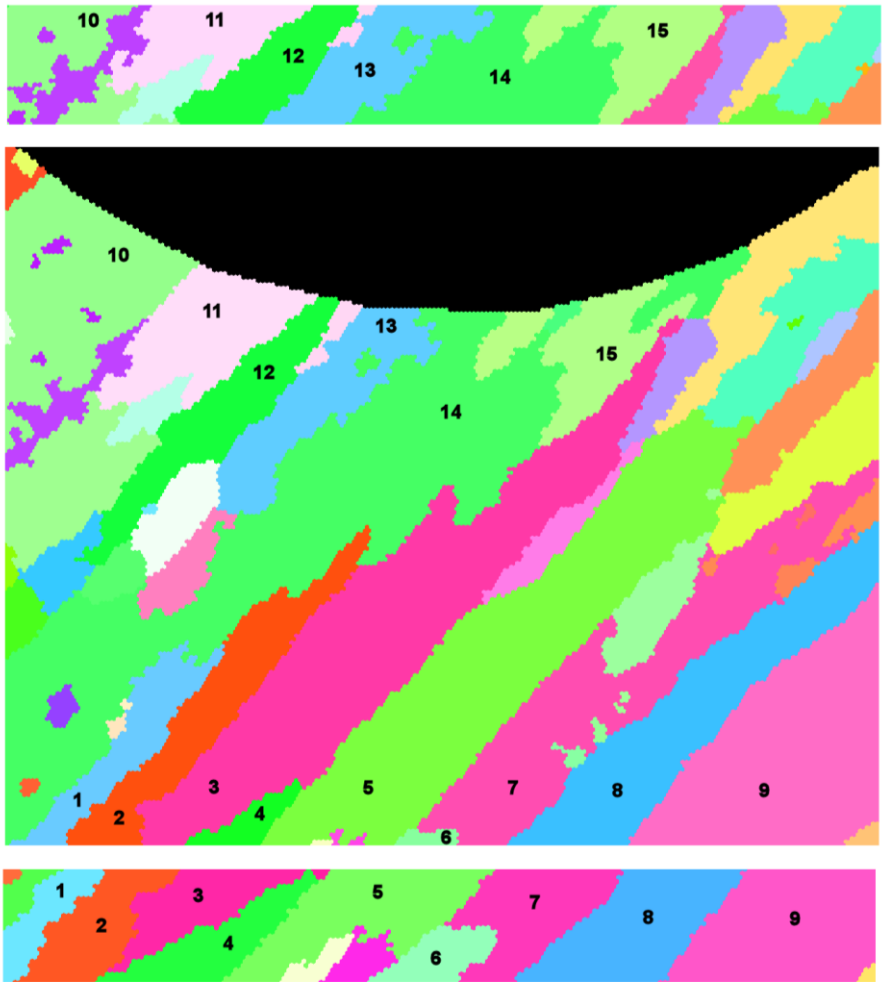

Figure 3.16: Picture shows the large EBSD scan in the middle along with the localized scans at the top and bottom of the scan.

Table 3.6 lists the rotation matrix values of the numbered grains comparing the rotation matrix values of the large scan to those of the localized scans.

Table 3.6: Values of the rotation matrix for the numbered grains in figure 3.16.

Grain ID	Site	Rotation matrix values								
1	Large scan	0.514	0.599	0.615	-0.531	0.784	-0.320	-0.674	-0.162	0.721
	Local scan	0.537	0.567	0.625	-0.517	0.806	-0.288	-0.667	-0.168	0.726
2	Large scan	0.730	-0.679	-0.074	0.681	0.732	-0.002	0.055	-0.049	0.997
	Local scan	0.715	-0.693	-0.094	0.697	0.717	0.011	0.060	-0.073	0.996
3	Large scan	0.945	-0.267	-0.190	0.223	0.949	-0.224	0.240	0.170	0.956
	Local scan	0.938	-0.274	-0.212	0.235	0.952	-0.195	0.256	0.133	0.958
4	Large scan	0.760	-0.650	-0.010	0.456	0.544	-0.704	0.463	0.531	0.710
	Local scan	0.748	-0.663	-0.032	0.459	0.551	-0.697	0.480	0.506	0.717
5	Large scan	0.797	0.075	-0.599	-0.073	0.997	0.028	0.599	0.022	0.800
	Local scan	0.790	0.079	-0.608	-0.055	0.997	0.058	0.611	-0.012	0.792
6	Large scan	0.785	0.148	0.601	-0.282	0.950	0.134	-0.551	-0.274	0.788
	Local scan	0.798	0.118	0.590	-0.262	0.951	0.165	-0.542	-0.287	0.790
7	Large scan	0.944	0.207	0.256	-0.261	0.945	0.198	-0.201	-0.254	0.946
	Local scan	0.949	0.190	0.252	-0.248	0.944	0.220	-0.195	-0.271	0.943
8	Large scan	0.925	-0.144	-0.351	-0.127	0.755	-0.643	0.358	0.640	0.680
	Local scan	0.919	-0.154	-0.363	-0.120	0.768	-0.629	0.376	0.621	0.687
9	Large scan	0.932	-0.292	-0.215	0.218	0.925	-0.312	0.290	0.244	0.925
	Local scan	0.922	-0.310	-0.230	0.237	0.925	-0.295	0.304	0.218	0.927
10	Large scan	0.682	0.573	-0.455	-0.708	0.673	-0.214	0.183	0.469	0.864
	Local scan	0.684	0.572	-0.453	-0.707	0.672	-0.219	0.179	0.470	0.864
11	Large scan	0.539	0.452	-0.710	-0.664	0.747	-0.029	0.517	0.487	0.703
	Local scan	0.535	0.453	-0.713	-0.667	0.745	-0.028	0.518	0.490	0.701
12	Large scan	0.938	-0.129	0.321	-0.108	0.774	0.624	-0.329	-0.620	0.712
	Local	0.938	-0.125	0.322	-0.110	0.775	0.623	-0.327	-0.620	0.713

	scan									
13	Large scan	0.750	-0.658	0.071	0.524	0.525	-0.671	0.404	0.540	0.738
	Local scan	0.749	-0.659	0.069	0.519	0.518	-0.680	0.412	0.545	0.730
14	Large scan	0.788	-0.299	0.538	0.409	0.908	-0.095	-0.460	0.295	0.838
	Local scan	0.790	-0.300	0.534	0.406	0.910	-0.089	-0.459	0.287	0.841
15	Large scan	0.903	-0.188	0.386	0.176	0.982	0.065	-0.391	0.009	0.920
	Local scan	0.907	-0.186	0.378	0.177	0.982	0.057	-0.382	0.015	0.924

Since the values of the rotation matrix do not differ significantly between large and localized scans, the change in working distance due to the inclined sample does not adversely affect the indexing of the diffraction patterns. Besides EBSD analysis, EDS analysis was performed on the location of crack nucleating inclusions, early results indicate that iron rich inclusions tend to break and induce a crack into the matrix which is similar to crack nucleation and propagation mechanics observed in the uniaxial samples (Bower and Schijve, 1973; Pearson, 1975; Lankford, 1982; Payne, 2010). For a more detailed description of the SEM analysis capabilities reference section 2.2.1.2.

3.3.3 Biaxial Fatigue Testing

Cruciform testing was conducted using a MTS biaxial frame. Due to the nature of the biaxial test on the cruciform, the sample was tested in both longitudinal and transverse directions simultaneously. Since material properties depend on the angular direction about the center hole, the cruciform could not be tested at longitudinal and transverse yield strength independently as was the case with the uniaxial samples. Rather the yield

strength for one of the material directions had to be chosen for the fatigue test. In this case, cruciforms were tested at the yield strength of the transverse direction which is 48,900 PSI or 337 MPa. The transverse direction yield strength was chosen in order to prevent severe plastic deformation on the regions of the hole where transverse material properties dominate since testing at longitudinal yield strength would put the cruciform under a tensile stress of 52,700 PSI or 363 MPa, which is over the yield strength of the material in transverse direction. The plastic deformation of the material in the hole region dominated by transverse properties would then impose a compressive stress after the first cycle that would reduce far field stresses imposed by the biaxial machine (Suresh, 1998). Moreover the presence of a large plastic zone would distort biaxial state of stress around the hole, causing a stress dependence on the angular position about the hole.

The biaxial machine used was too large to directly grip the cruciform sample. Therefore, a smaller grip assembly, which was in turn attached to the biaxial machine needed to be used. The smaller grip assembly was comprised of 4 wedge grips (1), 4 swivel arms (2), 4 threaded rods (3) and 4 grip arms (4). The entire assembly can be seen in Figure 3.17.

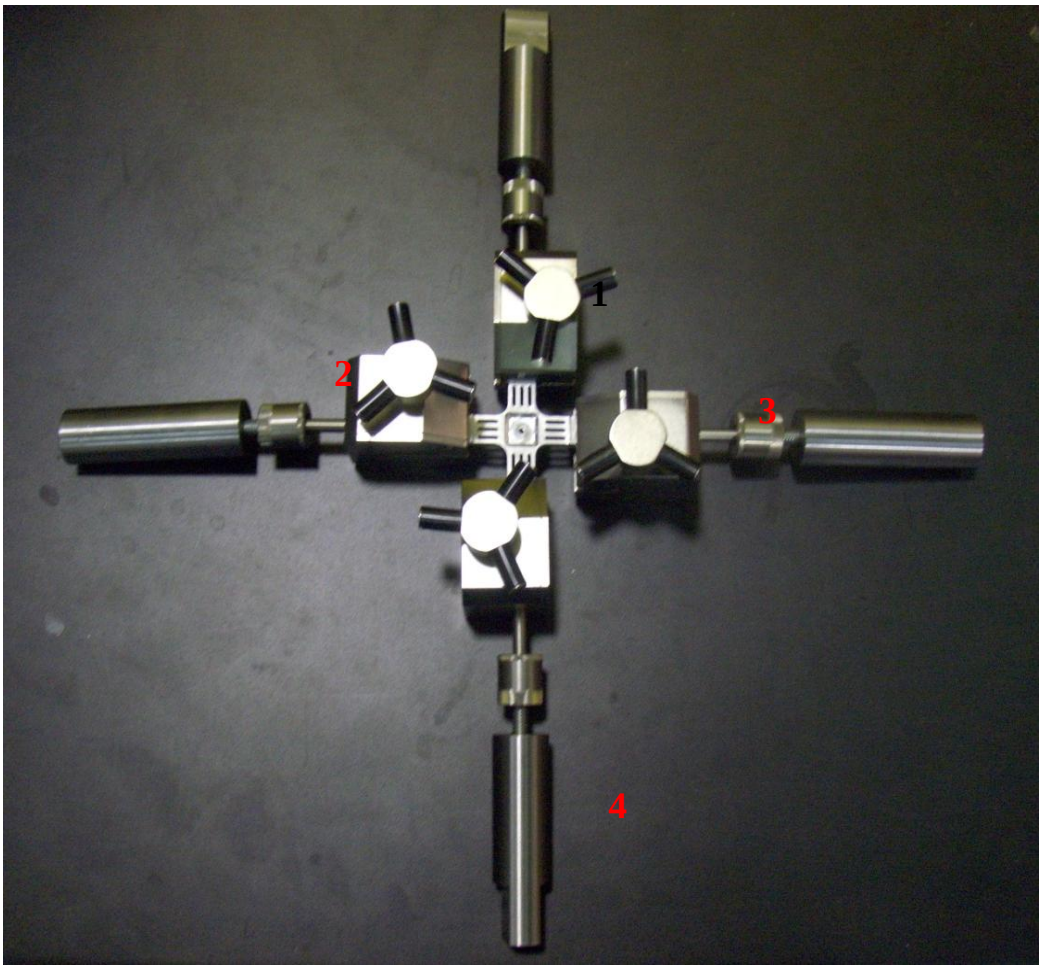

Figure 3.17: The small grip assembly.

The wedge grips were used to grab the cruciform sample. The swivel arms have a spherical joint inside the housing that cancels out any moments generated by the misalignment of the cruciform in the wedge grips insuring a biaxial state of stress. The threaded rods simply connect the swivel arms to the grip arms. Finally the grip arms were placed inside round wedge grips of the biaxial machine. The use of circular grip arms insured that the grip assembly was automatically centered inside the biaxial machine. Figure 3.18 shows the small grip assembly installed in the biaxial frame.

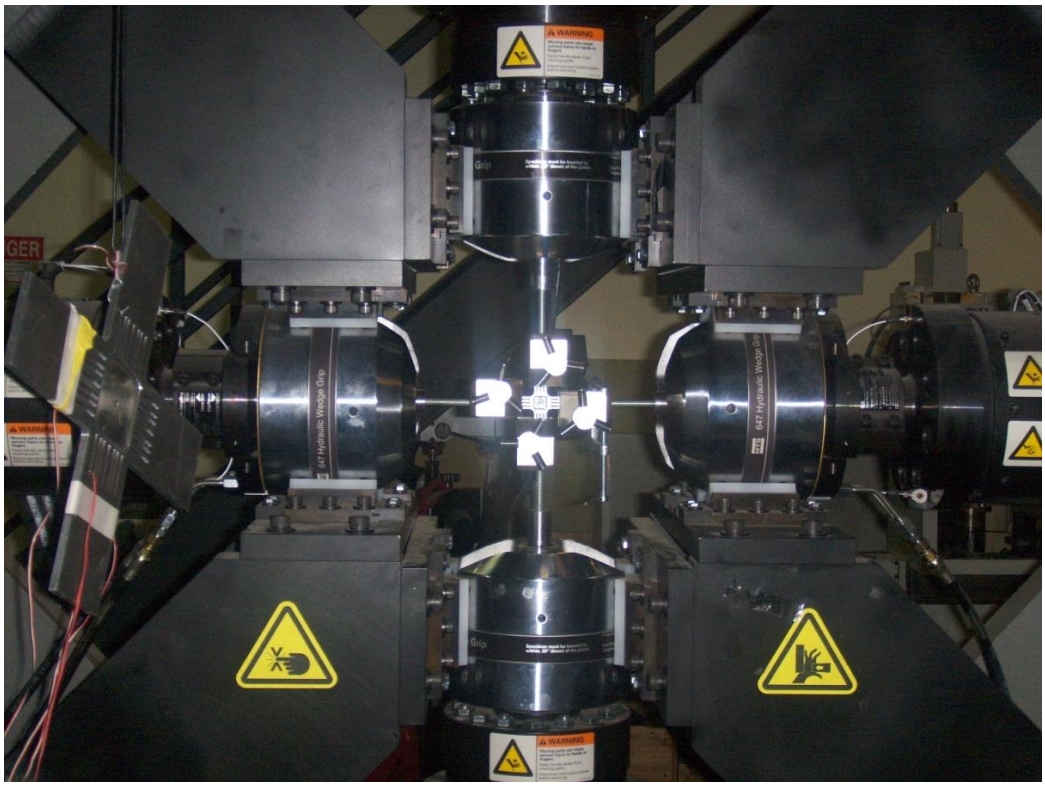

Figure 3.18: Small grip assembly installed in the biaxial frame.

Finite elements method was used to calculate the loads needed to achieve a stress comparable to the yield strength in the transverse direction. The cruciform gage area thickness was specified to 0.050" nominal. However, this dimension will change after the polishing procedure. Therefore, a micrometer was used to measure the thickness of the gage area after both sides of the cruciform were polished through step 3 outlined in table 3.5. The measurement was not taken at later steps since the contact surfaces of the micrometer leave dents and scratches which obscure EBSD scans. Material removal in steps 4-6 was estimated to be less than 0.001" total; therefore, measurement taken after step 3 is acceptable for use in the FEA analysis. The CAD model used for the

analysis was constructed with NX-7 software. Subsequently the model was meshed with the aid of the meshing tools found in the Advanced Simulation module of the NX software. Following the meshing process, the model was exported to NX-Nastran where the model was constrained and appropriate loads applied. Following the model solution, the predicted stresses were compared to the yield strength of the Al 2024-T351 in the transverse direction. The process might go through a few iterations until the predicted stress matches the yield strength value. Figure 3.19 shows the progression of the cruciform from CAD model to a solved model.

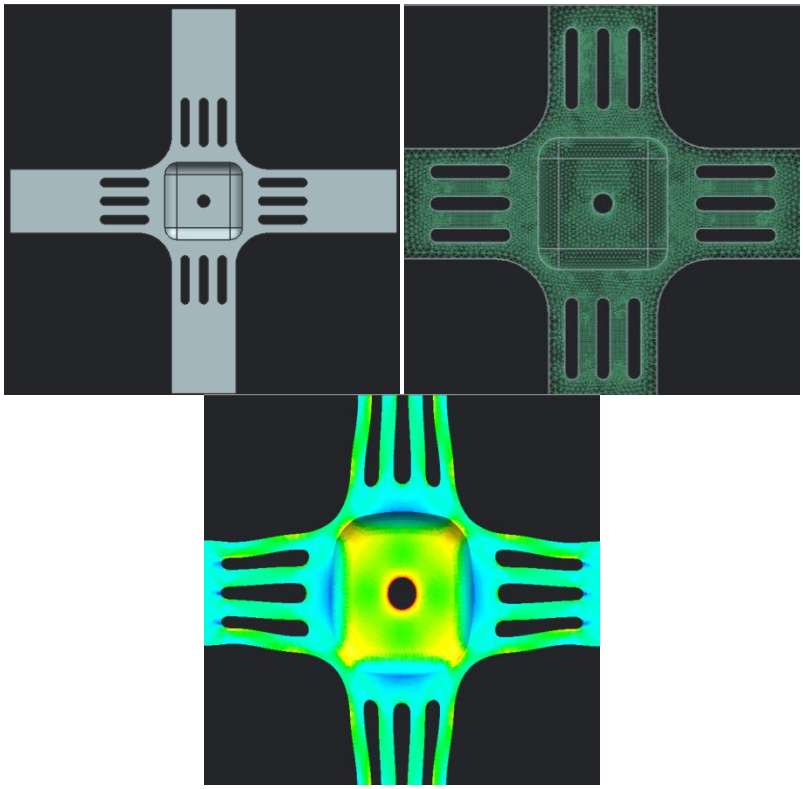

Figure 3.19: Progression of the cruciform model from a simple CAD model to the solved model.

For higher accuracy, the mesh is finer around the hole region as well as the slots. The model was meshed using higher order 3-D tetrahedral elements with 10 nodes.

Once loads were determined the cruciform was loaded into the biaxial frame for fatigue testing. Cyclic loading was generated using a sinusoidal function at a frequency of 10 Hz and a R-ratio of 0.100. The fatigue test was interrupted every 20,000 cycles in order to look for crack nucleation sites in the hole and gage area. The hole was examined under the SEM with the stage tilted at 60 degrees about the Y-axis while the gage area was evaluated with an optical microscope at 20X. All of the crack nucleating particles and subsequent cracks into the matrix were captured via photographs to document crack causing inclusions for later analysis. The test was carried out until the fatigue crack reached 1 mm in length on the gage area

CHAPTER 4

EXPERIMENTAL RESULTS AND DISCUSSION

This section shall discuss the findings from the experimental work for both dogbone and the cruciform sample geometries. A discussion will be offered on the interpretation of the results as they pertain to the effect of inherent material anisotropy on the short fatigue crack regime. The chapter will open first with the results gathered by the uniaxial samples and the corresponding discussion will be separated into four categories, starting off with a section on fatigue performance of the longitudinal and transverse samples, respectively. Then, the discussion will lead to the analysis of particle chemical and dimensional data that will aid in the interpretation of the fatigue performance data. Next, a fractography analysis is presented for longitudinal and transverse samples. Finally, the discussion of experimental results for the uniaxial samples will be closed by addressing the crystallographic data generated with the aid of EBSD maps obtained for both orientations along with a discussion on crystallographic directions prone to short crack nucleation. Cruciform data will be presented in a similar fashion as described above for the uniaxial samples. However, a more detailed analysis is presented on the crystallographic directions prone to short fatigue crack nucleation and propagation in the cruciform samples. This is in part due to the fact that cruciform samples were designed to test many local loading axes simultaneously, yielding those crystallographic directions that are most

prone to crack nucleation and propagation, while allowing the study of how these directions might be affected by the orthotropic symmetry at the macroscopic level induced by rolling of the Al 2024-T351 plates.

The dogbone samples are numbered as XL and XT where X stands for the number of the dogbone tested and L and T stand for longitudinal and transverse loading directions, respectively. Cruciforms are numbered C-1 thru C-7 where C stands for cruciform and the values 1-7 correspond to each of the seven cruciforms tested. There is no longitudinal or transverse designation given to the cruciforms since both directions are being evaluated concurrently during cyclic testing.

4.1 Dogbone Results

4.1.1 Fatigue Performance

As discussed in the literature review section, many studies have been performed on short fatigue crack properties of various rolled aluminum variants (Lankford, 1982; Newman and Edwards, 1988; Grosskreutz and Shaw, 1965; Schijve and Jacobs, 1965). However, only a few studies discussed in detail the effect of local and global anisotropy on the short fatigue crack regime (Morris et. al., 1976; Zabett and Plumtree, 1995; DeBartolo and Hillberry, 1998; Zhai; 2006). Studies that looked at the effects of anisotropy discovered that short fatigue crack behavior is indeed a function of sample orientation. Results obtained here from the Al 2024-T351 dogbones for the longitudinal and transverse directions are in agreement with previous findings. For the fatigue life analysis, 15

longitudinal and 13 transverse samples were used. The goal was to get 15 successfully tested samples at each orientation; however, a number of transverse samples went up to 800,000 cycles without failure. Possible reasons for this outcome will be discussed in more detail later. As previously discussed, all the samples were tested at their respective yield strength, which led to a statistical distribution of life at the chosen stress level. The key parameters measured during the cyclic testing procedure were life in cycles till particles fractured, life till crack propagated into the matrix and life till crack reached 1 mm. Figures 4.1and 4.2 show the results of the fatigue testing for both orientations.

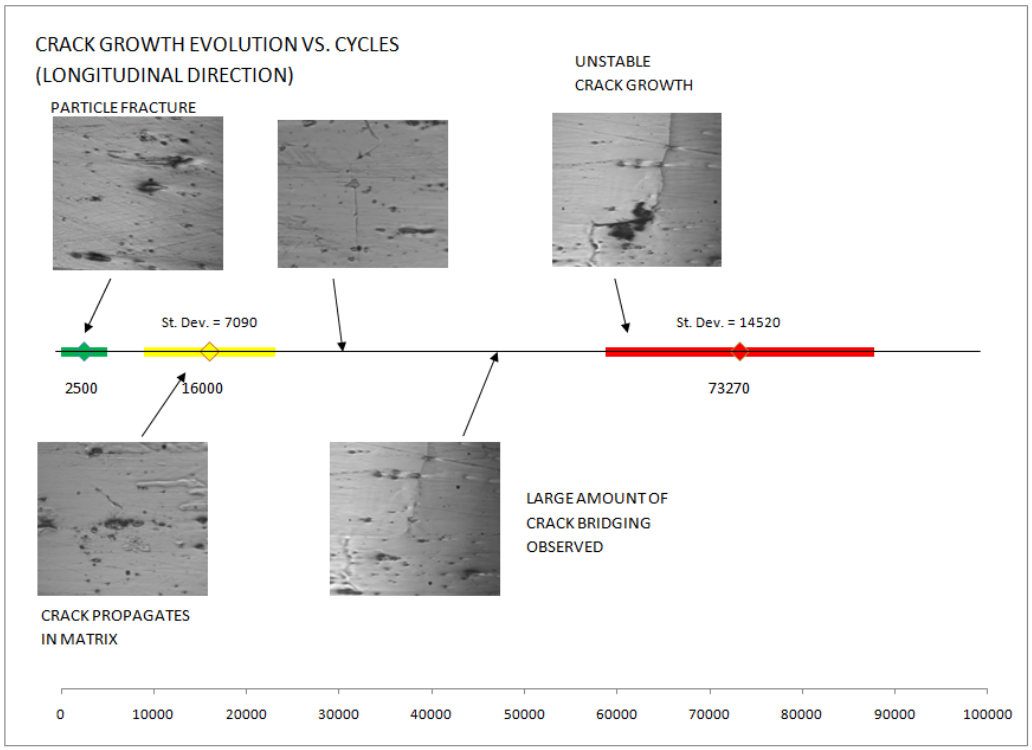

Figure 4.1: Crack growth evolution vs. cycles for the longitudinal samples.

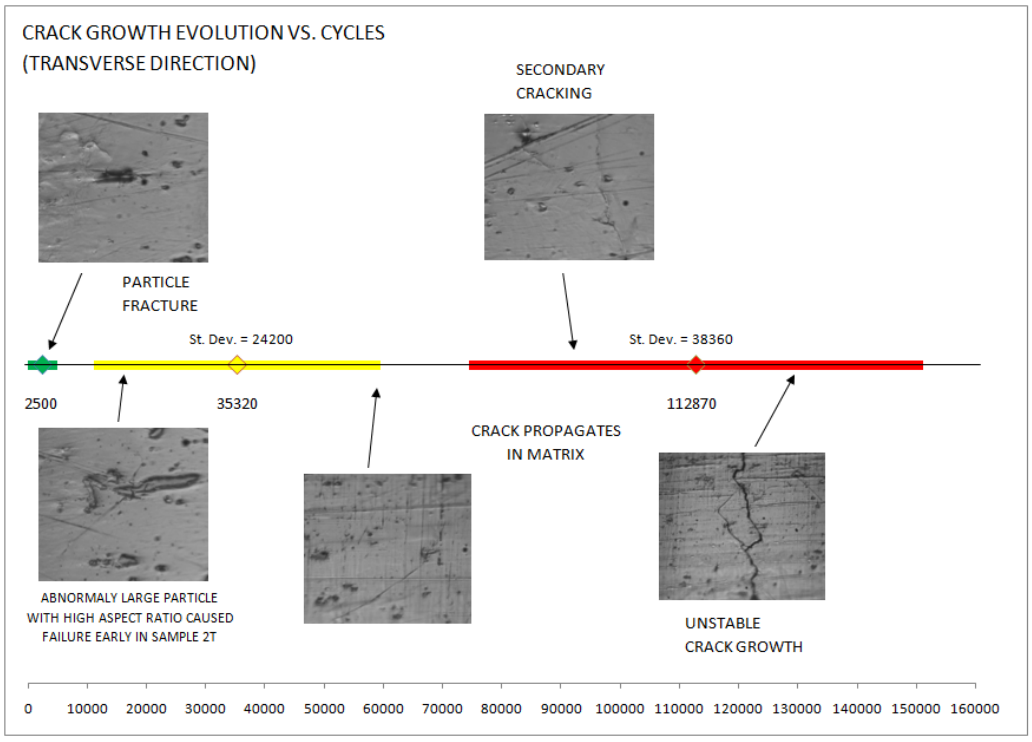

Figure 4.2: Crack growth evolution vs. cycles for the transverse samples.

Figures 4.1 and 4.2 indicate that precipitate fracture occurs very early in the fatigue life of the samples. Indeed numerous particles were observed to be fractured before any loads were applied to the specimens. This is the result of the rolling step during the thermo-mechanical processing of the material and has been reported in other studies as well (Bowles and Schijve, 1973; Payne et. al., 2010). Figure 4.3 shows the presence of fractured particles due to the rolling process.

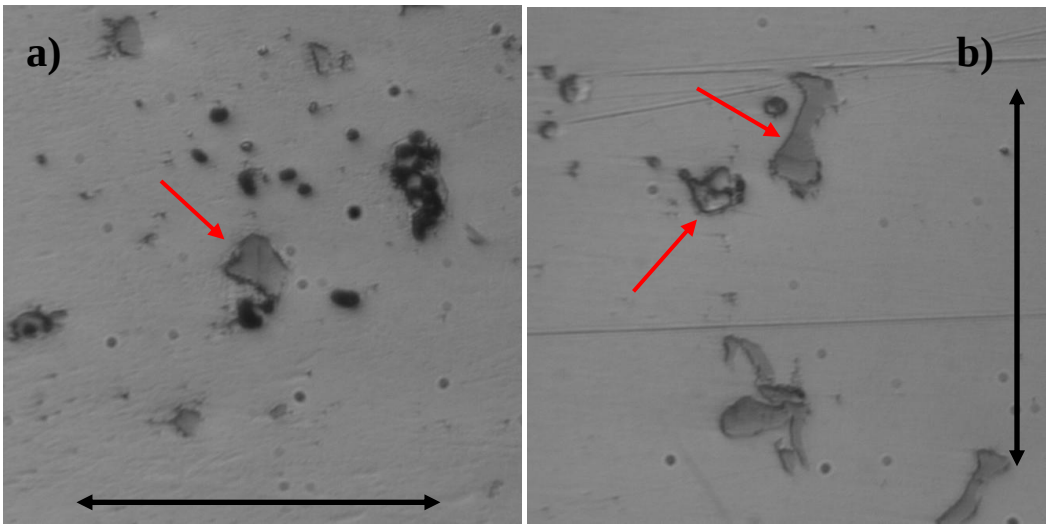

Figure 4.3: Fractured particles (identified by red arrows) due to the rolling step, a) sample 4L, b) sample 5T. Black arrows indicate rolling direction.

The majority of the particles that fractured during cyclic testing were broken in the first cycle followed by a scarce few in subsequent cycling. After about 5000 cycles no additional particles were observed to fracture and the samples reached a saturation limit in broken particles. Besides a few exceptions, all fractured particles were iron bearing Al_7Cu_2Fe particles. Similar results were observed by Payne et. al., 2010, where in situ SEM observations of Al 7075-T651 showed a large increase in fractured particles in the first cycle after which only a few additional broken particles were discovered. While the trend is similar for both sample orientations, L samples exhibited a higher frequency of fractured particles than the T samples. Moreover, T samples had a higher instance of particle/matrix debonding, which mainly occurred at the softer Al_2CuMg particles.

Crack initiation into the matrix occurred at 16±7 kcycles for the longitudinal samples. All the cracks were initiated by fractured particles with a few instances of cracks appearing from defects resulting from either the casting or thermo-mechanical processing. The majority of the cracks initiated through-thickness in the middle portion of the notch with a few instances of crack nucleation on the edge between the face and notch surfaces. Examples of typical crack nucleating particles for the longitudinal load direction can be seen in Figure 4.4.

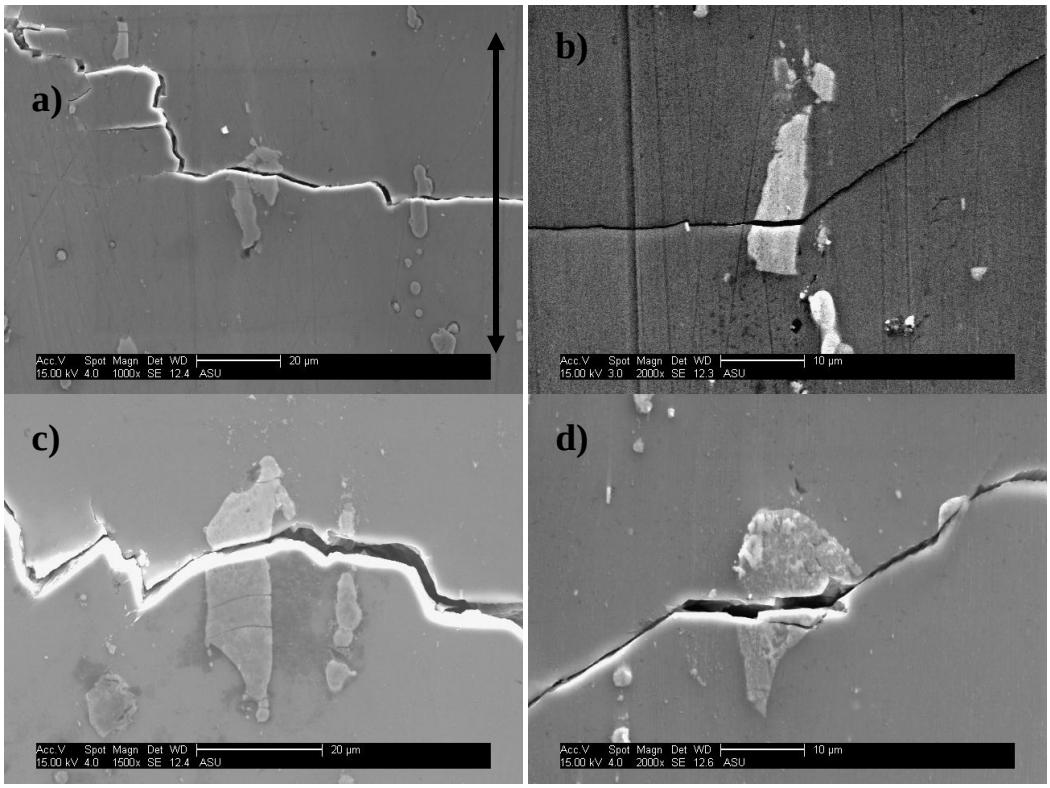

Figure 4.4: Typical crack nucleating particles for the longitudinal samples, a) 1L, b) 3L, c) 7L and d) 9L. Arrow indicates loading and rolling direction, applicable for all pictures.

All the particles shown in figure 4.4 contain iron in their chemical composition. The presence of iron is the primary contributor to the

brittleness of the particles (Li, 2006). Particle brittleness is also evident by the perpendicular fracture plane of the inclusions relative to the load axis. The standard deviation of 7000 cycles is likely attributed to varying shape, size, and chemical makeup of the particles along with crystallographic orientation of the matrix. Indeed there are many instances in which fractured particles did not nucleate a crack in the matrix. This is most likely due to unfavorable crystallographic direction of the surrounding matrix grain.

Crack initiation into the matrix for the transverse samples occurred at 35±24 kcycles. While all the cracks initiated from fractured particles for the longitudinal samples, matrix cracks in the transverse samples were initiated by either fractured or debonded particles. Cracks mainly nucleated in the notch with a few instances of crack nucleation on the edge between the face and notch surfaces. Examples of typical crack nucleating particles for the transverse samples can be seen in Figure 4.5

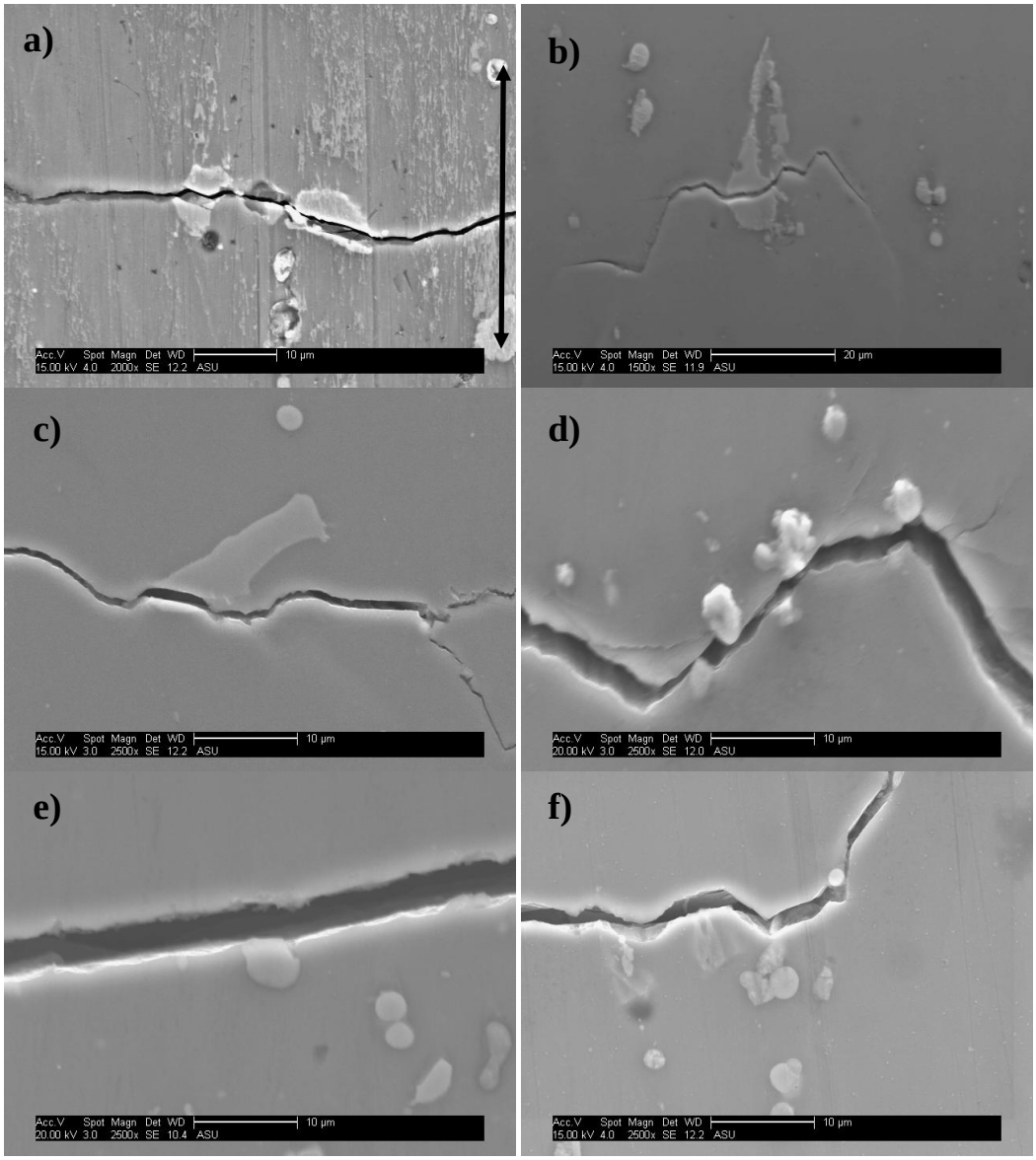

Figure 4.5: Typical crack nucleating particles for the transverse samples. Pictures a-c show fractured crack nucleating particles for samples 3T, 8T and 12T. Pictures d-f show debonded crack nucleating particles for samples 5T, 6T and 11T. Arrow indicates load direction for all samples.

Particles in Figure 4.5 a-c are iron bearing (Al_7Cu_2Fe) particles that initiated a matrix crack due to fracture. Particles in Figure 4.5 d-f are softer (Al_2CuMg) particles that initiated matrix cracks by debonding. Rare instances of soft particle fracture were observed only in cases where particles sizes exceeded 20 µm. The addition of debonding as a failure

mechanism is in part one of the reasons why the standard deviation for the transverse samples is higher compared to their longitudinal counterparts. However, the addition of debonding alone does not explain the increased variance in the life till the crack initiates in the matrix. For example, both samples 2T and 3T had their respective failing crack initiated by fractured iron bearing particles. Conversely life till crack initiated in the matrix was 23000 cycles for 2T and 95600 cycles for 3T. In this case, the variance in the lives could be attributed to the disparity in the size of the crack nucleating particles, since the nucleating particle height for samples 2T and 3T was 65 μm and 9 μm, respectively. Figures 4.6 and 4.7 plot cycles till crack propagates to the matrix versus particle height and width, respectively, for transverse samples where height is the dimension of the particle parallel to the load and width is the dimension perpendicular to the load.

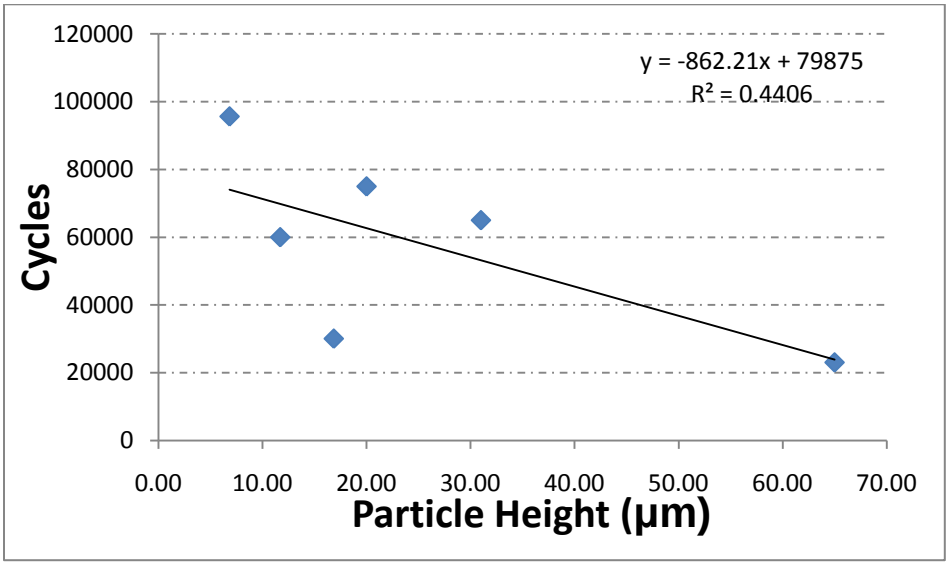

Figure 4.6: Life (in cycles) till crack propagates to the matrix from a broken particle as a function of particle height for transverse samples.

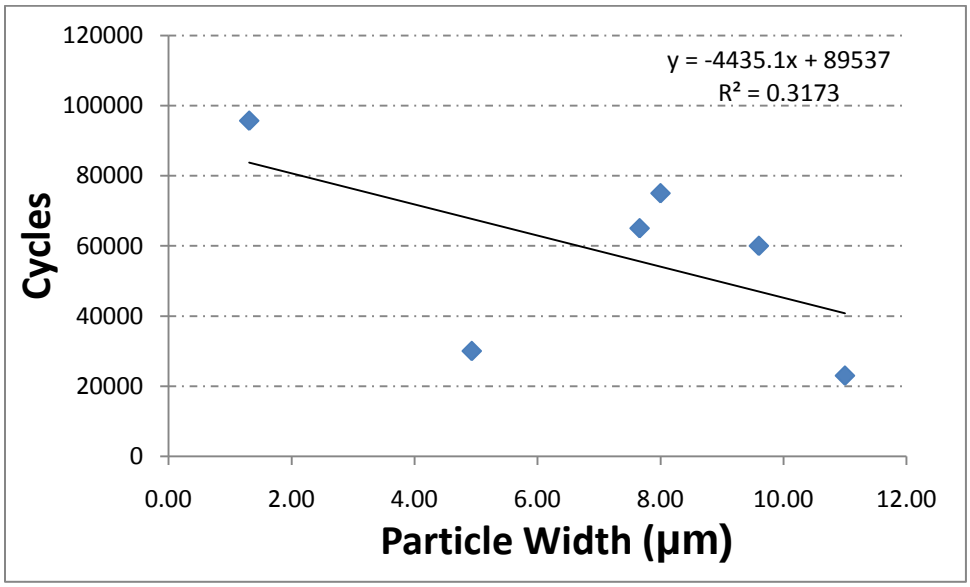

Figure 4.7: Life (in cycles) till crack propagates to the matrix from a broken particle as a function of particle width for transverse samples.

Except for a few exceptions, Figures 4.6 and 4.7 show a clear trend of decreasing number of cycles to propagate a crack into the matrix as the particle size increases. A similar trend was also observed for the longitudinal samples, as can be seen in Figures 4.8 and 4.9. Since enough data point were available, error bars were calculated for Figures 4.8 and 4.9. Normal distribution was assumed and the error bars were constructed with 95% confidence.

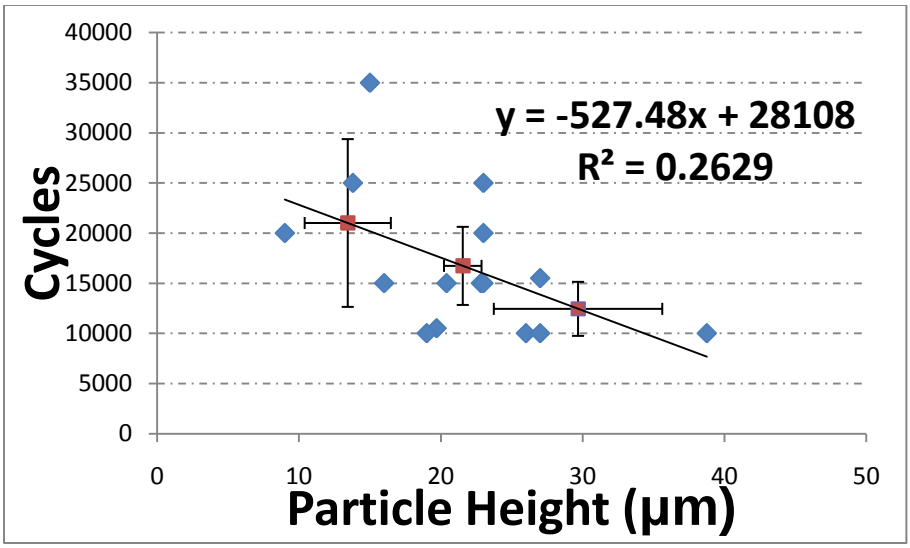

Figure 4.8: Life (in cycles) till crack propagates to the matrix from a broken particle as a function of particle height for longitudinal samples.

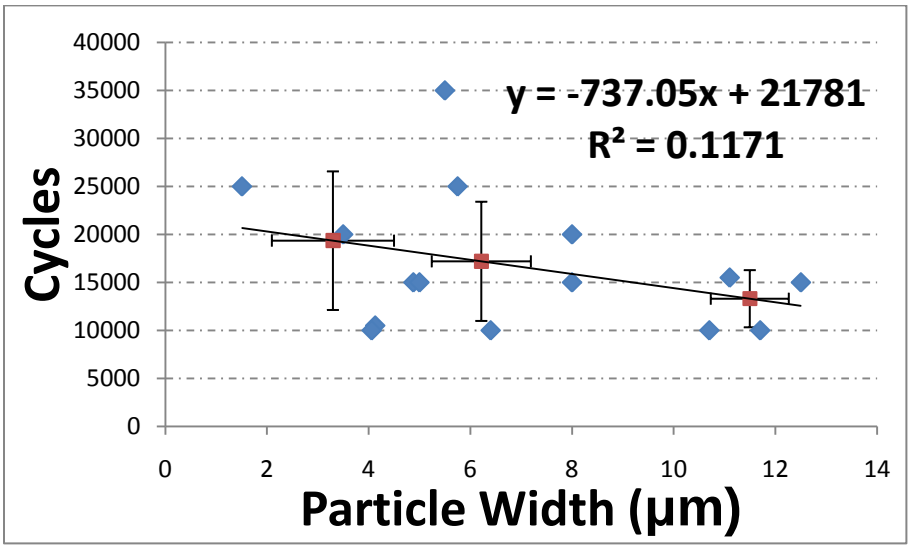

Figure 4.9: Life (in cycles) till crack propagates to the matrix from a broken particle as a function of particle width for longitudinal samples.

In similar fashion particle height and width for longitudinal samples is measured parallel and perpendicular to the load, respectively. As with transverse samples, Figures 4.8 and 4.9 show a few instances where smaller particles nucleated cracks faster than their larger counterparts. For

both orientations, this is most likely due to the crystallographic orientation of the surrounding grains.

Not surprisingly the debonded particles showed trends similar to those presented in Figures 4.6 thru 4.9 as can be seen in Figures 4.10 and 4.11.

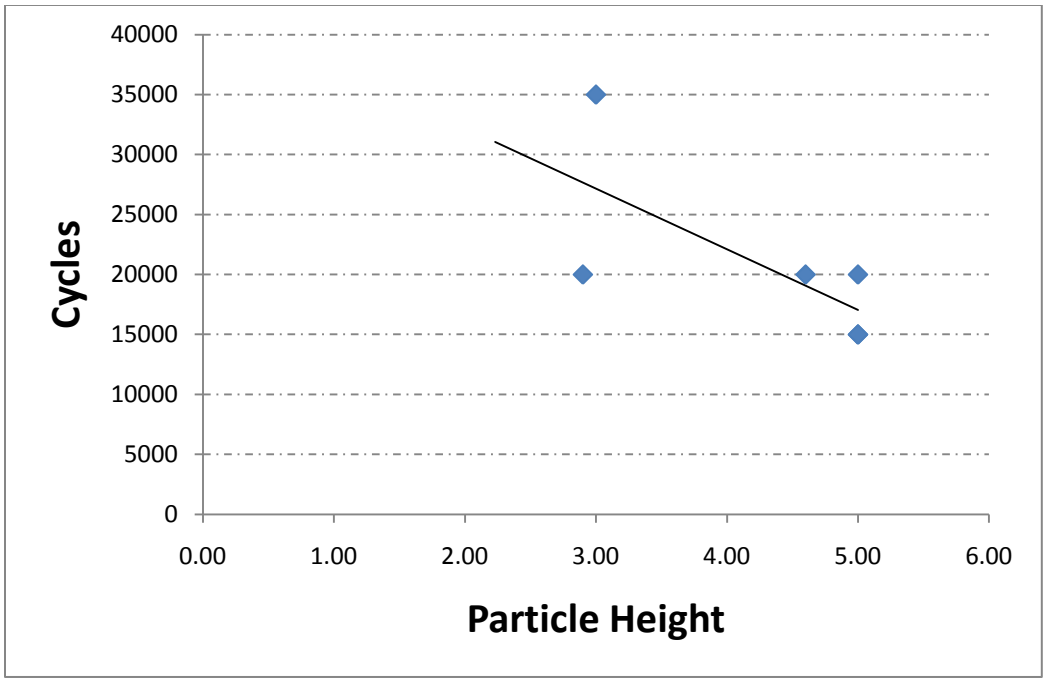

Figure 4.10: Life (in cycles) till crack propagates to the matrix from a debonded particle as a function of particle height for debonded particles in the transverse samples.

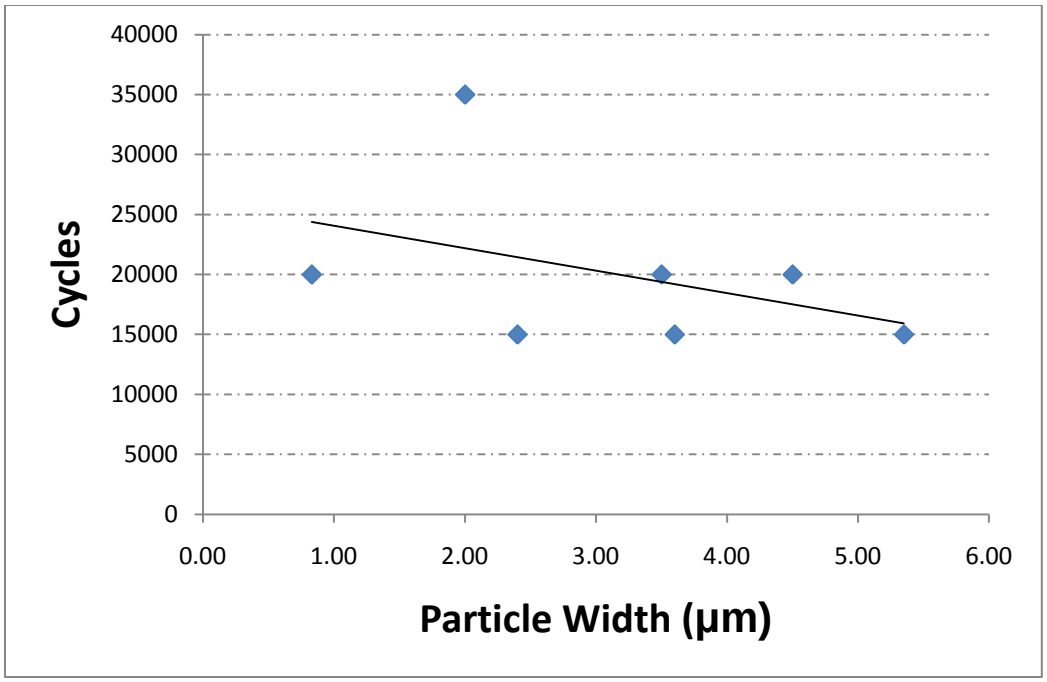

4.11: Life (in cycles) till crack propagates to the matrix from a debonded particle as a function of particle width for debonded particles in the transverse samples.

Another aspect of transverse samples that certainly contributed to the higher variance is the greater variability in the particles sizes responsible for failure causing cracks. Figure 4.12 shows the sizes of these particles for both longitudinal and transverse samples. The figure contains information on both the fractured and debonded particles separately for the transverse samples.

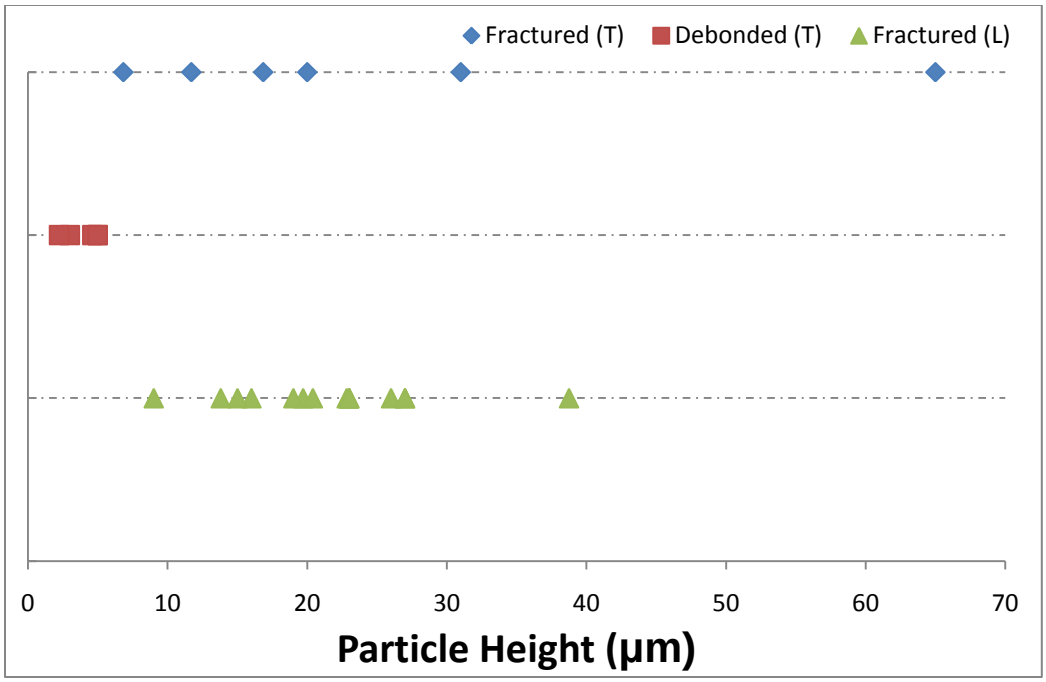

Figure 4.12: Height of failure-causing particles for longitudinal and transverse samples.

The particle size grouping for the longitudinal samples is much narrower when compared to the fractured crack initiating particles found on the transverse samples. Conversely, variability in the size for the debonded particles is much smaller than compared to that of fractured particles in both longitudinal and transverse samples.

Difference in fatigue lives till crack initiates in the matrix between transverse samples that fractured and debonded could be explained by the sharpness of the initial discontinuity in the matrix upon the immediate fracture/debonding of the failure causing particles. Figure 4.13 illustrates the morphology of the two failure phenomena. Looking at figure 4.13a it is evident that the flaw at the particle/matrix interface created by the fractured particle is quite blunt. The blunting causes the flaw to act like a

notch that requires additional fatigue cycles to actually generate a propagating crack into the matrix. The flaw generated by the debonded particle and shown in figure 4.13b is much sharper at the particle/matrix interface compared to its fractured counterpart. The sharpness of the flaw enhances the stress intensity in the matrix and causes the flaw to act in a crack like fashion immediately upon its creation. Therefore, the crack like aspect of the debonded flaw requires little to no additional fatigue cycles to initiate crack propagation into the matrix. It should also be noted that despite the large disparity between the particle sizes shown in figure 4.13, the actual discontinuity flaw width, measured perpendicular to the loading axis, is of similar dimensions.

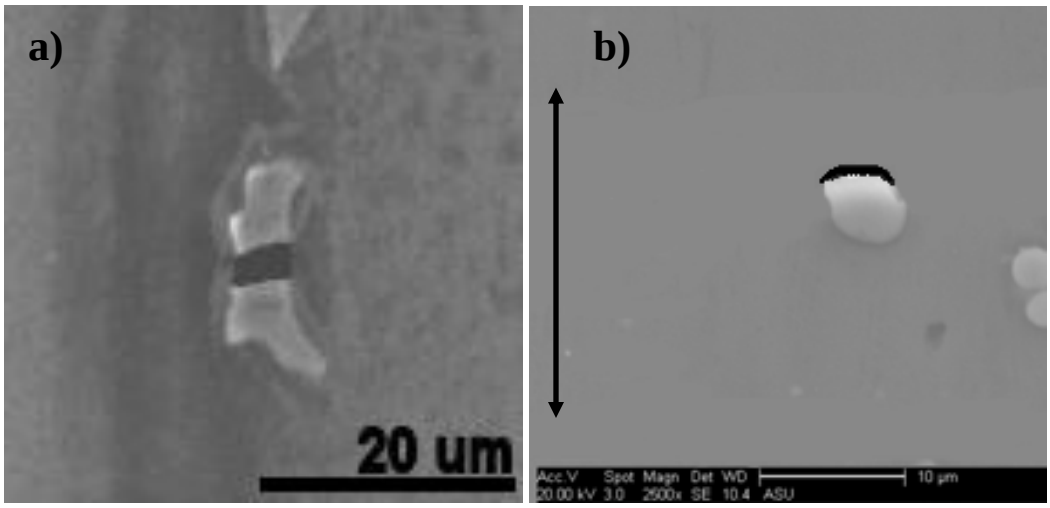

Figure 4.13: Flaw types induced into the matrix by a) fractured particles and b) debonded particles. Arrow indicates load direction. The discontinuities have been enhanced for better viewing.

Figures 4.6 thru 4.12 clearly point to the fact that iron bearing particles are larger in size when compared to their soft particle counterparts. This phenomenon has been consistently reported for 2000

and 7000 series alloys in many studies previously performed (Pearson, 1975; Payne et. al. 2010). The ease with which the soft particles debond for transverse specimens implies a weak mechanical bond between the matrix and smaller soft particles. Weak mechanical cohesion at the particle/matrix interface was also reported for Al 2024-T3 by Bowles and Schijve (1973). Conversely, the larger area of the bigger iron bearing particles insures higher mechanical cohesion that acts to fracture the particle due to a more efficient load transfer between the matrix and subject particles. Instances of fractured particles are less for transverse samples when compared to the longitudinal samples. Moreover, the crack tends to kink at high angles and grow around the iron bearing particles in the transverse samples, which can be seen in figure 4.14. A possible reason for this behavior is the favorable orientation of the particle in the transverse samples that effectively reduces the stress imposed on the particles. The decreased frequency of fracture could also explain the lack of multi-site cracking that is prevalent in longitudinal samples and therefore, increasing fatigue performance. A more detailed discussion on effects of multi site fracture and particle orientation with respect to the material directions will be offered later in the text.

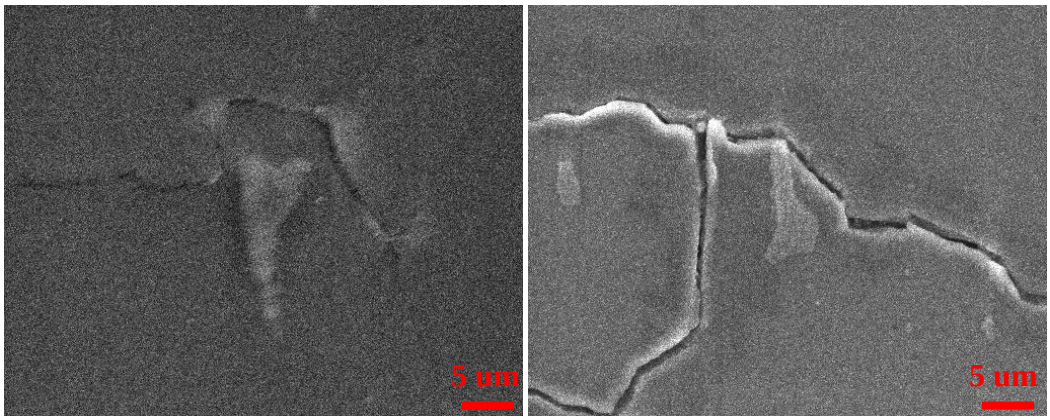

Figure 4.14: Large crack deflections by iron bearing particles in transverse samples.

While the majority of the discussion thus far has been on the particle effect on the fatigue performance of transverse and longitudinal samples, it is worthy to spend some time evaluating possible effects of grain morphology on small fatigue crack nucleation into the matrix. Figure 4.15 illustrates EBSD scans of the notch for the longitudinal and transverse samples, respectively.

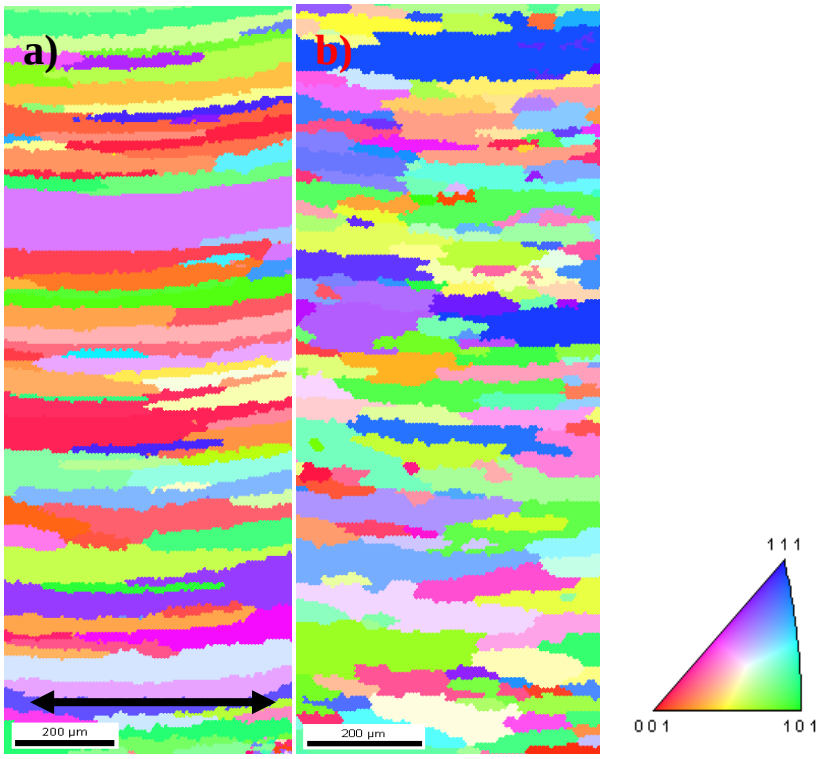

Figure 4.15: Inverse pole figure maps obtained from EBSD scans of a) longitudinal notch and b) transverse notch. The evident curvature present in the longitudinal scan is due to the curvature of the notch. Inverse pole figure maps plotted along the loading direction defined by the black arrow.

It is clearly evident that grains in the longitudinal notch are larger when compared to their transverse counterparts. It has been demonstrated in previous studies that larger grains are more prone to damage accumulation in the form of persistent slip due to increased spacing between grain boundaries (Suresh, 1998; Li, 2006; Tanaka and Mura, 1982, Gupta and Agnew, 2011). Increase in accumulated damage could promote earlier particle fracture and crack growth that could serve as another mechanism for earlier crack initiation of short cracks into the matrix for longitudinal samples.

In summary, the difference in life till crack propagates to the matrix between the longitudinal and transverse samples shows dependency on particle size and failure type properties. Looking at Figures 4.6-4.13, it can be seen that on average, failure causing particles in the longitudinal samples are larger compared to their transverse counterparts which could explain the lower life in cycles till the crack propagates to the matrix. Moreover, since the longitudinal samples experience only one type of crack initiating phenomenon (i.e. due to fractured particles only), the variance in life is seen to be much smaller compared to the transverse samples. On the other hand, the combination of varying crack initiating phenomena coupled with higher particle size variance for the transverse samples are the most likely contributors to differing matrix crack initiating times and higher variance. Furthermore, the disparity in grain sizes between the longitudinal and transverse samples could negatively influence fatigue performance of longitudinal samples since larger grains are more prone to damage accumulation due to longer slip lengths and larger plastic strains.

While the majority of cracks initiated due to either iron bearing or soft particles, a few samples failed due to the presence of linear defects that originated during casting or thermo-mechanical processes. Figure 4.16 depicts two such instances of defect driven failures in samples 5L and 4T.

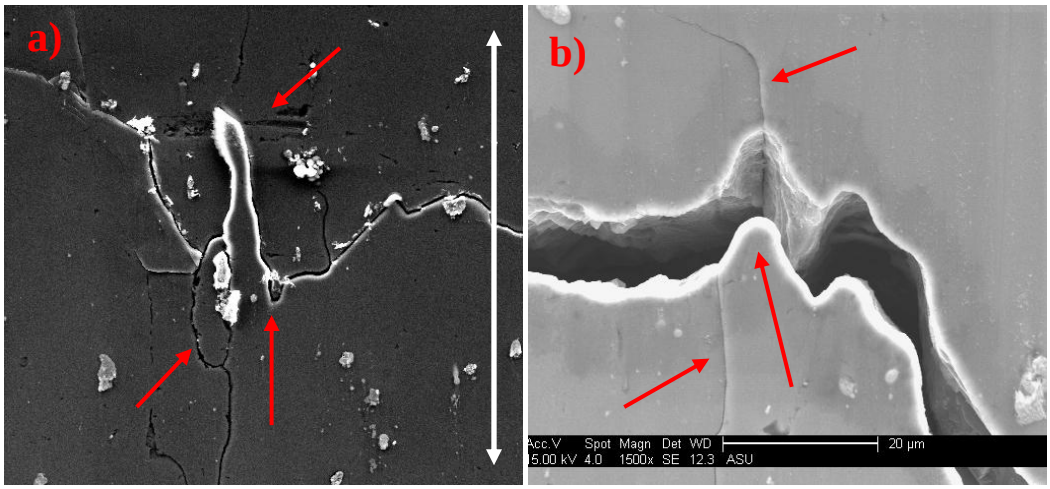

Figure 4.16: Casting defects (identified by red arrows) responsible for the failing crack in samples a) 5L and b) 4T. Arrow shows the loading direction.

The morphology of the defects suggests that a relatively large pore failed to completely close during the rolling process, which left in its wake a linear defect that acted as a crack-initiating site. Furthermore, EDS performed by two independent detectors showed the presence of Carbon and Oxygen implying some type of hydrocarbon contamination present at the site. The defect had no significant effect on the total life of sample 5L, since it had a life of 90,200 cycles till the crack reached one millimeter, which is 23% higher than the average life of all longitudinal samples tested. However, the life of sample 4T, 66,520 cycles, is 41% lower than the average of all transverse samples. Similar defects were discovered on other samples, but most were in unfavorable locations that prevented crack initiation. A total of three samples (5L, 10L and 4T) had cracks initiated by similar defects.

Life in cycles till the crack reached 1 mm for the 15 longitudinal samples averaged out to be about 73±15 kcycles. For the 13 transverse samples life till the crack reached 1 mm averaged to be 110±40 kcycles. While the yield strength is higher for the longitudinal samples as seen in Table 4.1, transverse samples possess better fatigue performance.

Table 4.1: Tensile results for longitudinal and transverse samples.

Orientation	Yield Strength	Ultimate strength
Longitudinal	363 MPa	486 MPa
Transverse	337 MPa	498 MPa

Since L and T samples are being tested at their respective yield strength, the longitudinal samples are being tested at higher stresses. If the fatigue lives of the L and T samples were similar, that would indicate the dominance of cyclic plasticity in the fatigue response. However, it has been clearly demonstrated with the data presented thus far that fatigue properties are influenced by quasi-static failure of particles. Looking at the S-N curve of 2024-T3, (which is comparable to 2024-T351) the predicted fatigue life is around 115 kcycles for longitudinal samples at 337 MPa and 90 kcycles for 363 MPa (Mil Handbook 5, 1998). However, test results show the average fatigue life to be around 73 kcycles for 2024-T351. If the difference in the predicted values is added to the test value then the predicted life at 337 MPa would be about 100K, which is still lower than average life of the T samples. This quick comparison indicates that quasi-static failure modes would still govern the fatigue response in the longitudinal samples even if they were tested at the lower stresses used for the transverse specimens. However, actual experimental work needs

to be done to confirm this hypothesis. A few phenomena were observed that can shed some light on the poor performance of the longitudinal samples compared to the transverse samples. First, the longitudinal samples experienced a high fraction of multi-site crack initiation. The cracks would grow independently up until about 75% of the fatigue life when the cracks began to coalesce together to form larger cracks, which in turn led to substantially increased crack length and crack growth rate. Evidence of multi-site crack nucleation and coalescence can be observed in figure 4.17.

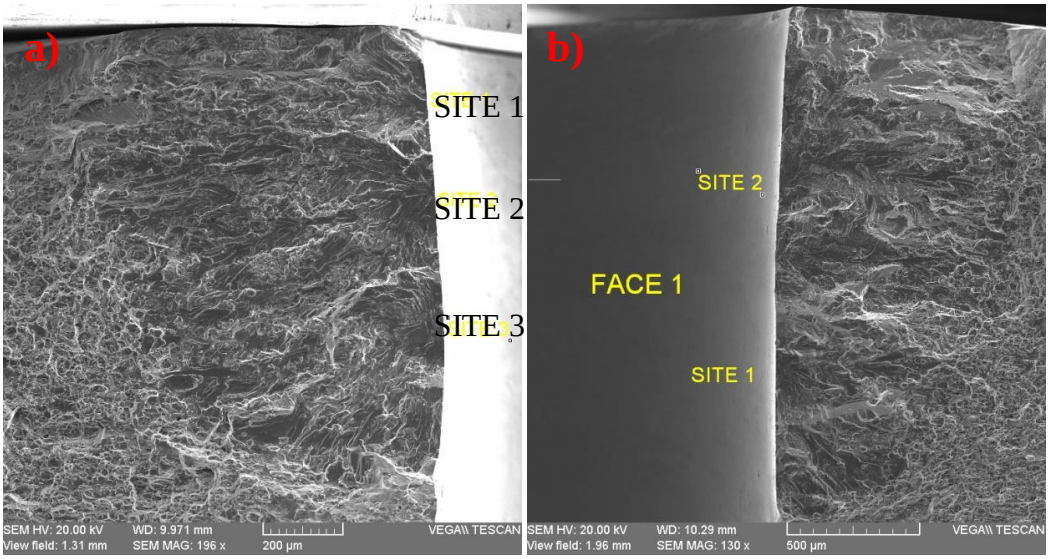

Figure 4.17: Crack initiation sites for a) 1L and b) 7L.

On the other hand, the transverse samples exhibited only one crack-initiating site most of the time. It stands to reason that a single crack would take longer to reach 1 mm when compared to three 200-300 µm individual cracks that joint to form the final failure-causing crack. Figure 4.18 illustrates crack surfaces of transverse samples containing only one crack-initiating site. The discussion offered on figure 4.14 shed some light

on possible reasons for reduction of crack initiating sites due to particle orientation in transverse samples. However, a more detailed discussion will be offered in section 3.1.2.

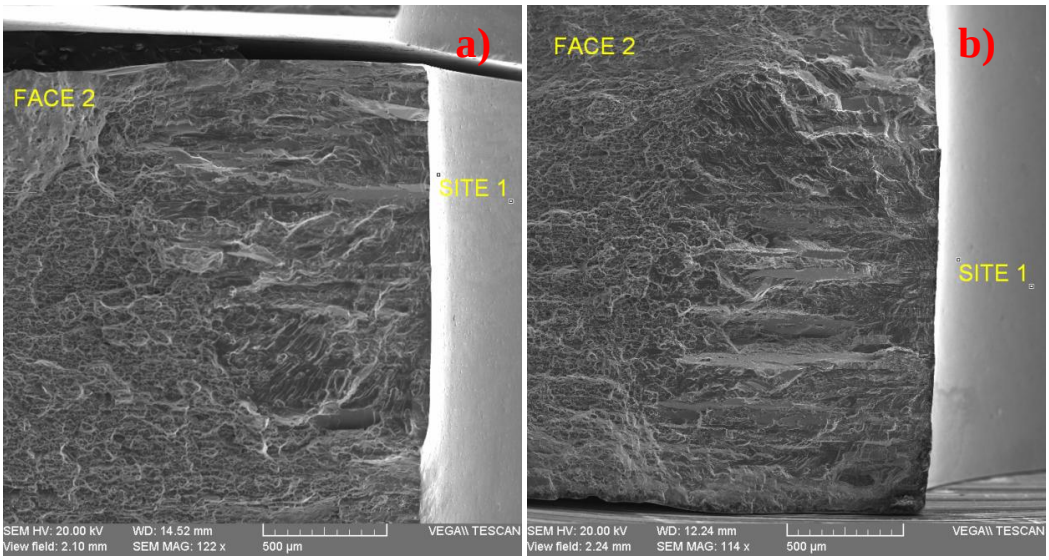

Figure 4.18: Crack initiation sites for a) 2T and b) 17T.

Crystallographic length scale disparities between the two orientations could also serve as a source for varying fatigue lives. Referring back to figure 4.15, it has already been established that longitudinal samples have larger grains in the notch when compared to the transverse samples. Because larger grains are more susceptible to deformation it is possible that the increased bulk plasticity in the larger grains acts to increase the crack driving force of the short fatigue cracks. Indeed this hypothesis has been proposed by Lankford (Lankford, 1982). The transverse samples would not experience deformations gradients as large due to smaller grains, which would effectively reduce the crack driving force due to the bulk plasticity within these grains. Cracks in the transverse samples were often observed to retard in their growth for a period of time, while little to

no crack retardation was observed in the longitudinal samples. Another possible reason for slower crack growth in the transverse samples is the increased frequency of grain boundaries as compared to the longitudinal samples. Grain boundaries are known to slow down or completely arrest crack growth, especially in the short fatigue crack regime (Lankford, 1982; Lankford, 1985; Zhai et. al., 2000).

4.1.2 Particle Chemistry and Dimensional Data

For the longitudinal samples there were 63 iron bearing and 14 soft particles observed on or near the crack path. Chemical composition and dimensional data for iron bearing and soft particles can be seen in Tables 4.2 and 4.3.

Table 4.2: Chemical and dimensional data for the 63 iron bearing particles observed in longitudinal samples. AR stands for aspect ratio and St. Dev. Stands for standard deviation.

	at% Cu	at% Al	at% Fe	at% Mn	at% Si	at% Mg	Height (um)	Width (um)	AR
Mean	13.81	59.04	14.89	8.77	4.80	n/a	16.51	7.40	2.60
St. Dev.	7.42	5.52	2.60	1.83	1.08	n/a	6.18	3.62	1.34
Max	47.55	81.39	23.90	11.53	6.84	n/a	34.80	19.20	9.14
Min	7.70	38.54	8.29	1.70	0.44	n/a	5.00	1.51	0.50

Table 4.3: Chemical and dimensional data for the 14 soft particles observed in longitudinal samples. AR stands for aspect ratio and St. Dev. Stands for standard deviation.

	at% Cu	at% Al	at% Fe	at% Mn	at% Si	at% Mg	Height (um)	Width (um)	AR
Mean	43.13	54.40	n/a	n/a	n/a	4.95	14.46	4.94	2.84
St. Dev.	16.40	15.07	n/a	n/a	n/a	3.97	11.17	2.56	1.27
Max	79.07	78.50	n/a	n/a	n/a	10.11	38.76	10.70	4.93
Min	20.75	20.93	n/a	n/a	n/a	1.03	5.25	2.45	1.00

Likewise for the transverse samples 41 iron bearing and 22 soft particles were observed on the crack path. Particle chemical and dimensional data can be seen in Tables 4.4 and 4.5.

Table 4.4: Chemical and dimensional data for 41 iron bearing particles observed in transverse samples. AR stands for aspect ratio and St. Dev. Stands for standard deviation.

	at% Cu	at% Al	at% Fe	at% Mn	at% Si	at% Mg	Height (um)	Width (um)	AR
Mean	17.79	58.37	13.82	7.08	4.52	n/a	15.98	6.48	2.86
St. Dev.	10.40	7.20	3.82	2.19	1.40	n/a	10.97	4.62	1.56
Max	48.67	74.26	22.73	10.52	7.48	n/a	65.00	28.80	7.86
Min	8.04	28.27	6.82	1.68	1.88	n/a	1.50	1.20	0.39

Table 4.5: Chemical and dimensional data for 22 soft particles observed in transverse samples. AR stands for aspect ratio and St. Dev. Stands for standard deviation.

	at% Cu	at% Al	at% Fe	at% Mn	at% Si	at% Mg	Height (um)	Width (um)	AR
Mean	38.44	56.66	n/a	n/a	n/a	5.84	10.44	4.07	2.39
St. Dev.	16.39	14.47	n/a	n/a	n/a	4.02	14.15	1.85	2.69
Max	79.60	83.51	n/a	n/a	n/a	13.47	66.10	9.00	13.38
Min	6.29	20.40	n/a	n/a	n/a	1.33	2.23	0.83	0.80

Surprisingly, the dimensional data between the two orientations is comparable for both iron bearing and soft particles. Soft particles for the longitudinal direction are slightly larger compared to their transverse counterparts. The similarity of the dimensional data could be a result of only observing those particles that were involved in the fracture process, which have sizes that should correspond to the upper tail of the particle size distribution in the samples (Merati, 2004). The iron content, along with the other elements, between the two orientations is also similar, as expected. Since iron content is primarily held responsible for early fracture

of the particles (Merati, 2004; Patton et. al., 1998; Brockenbrough et. al., 1993; Tanaka and Mura, 1982), fatigue life till crack initiated into the matrix was plotted as a function of iron percent content.

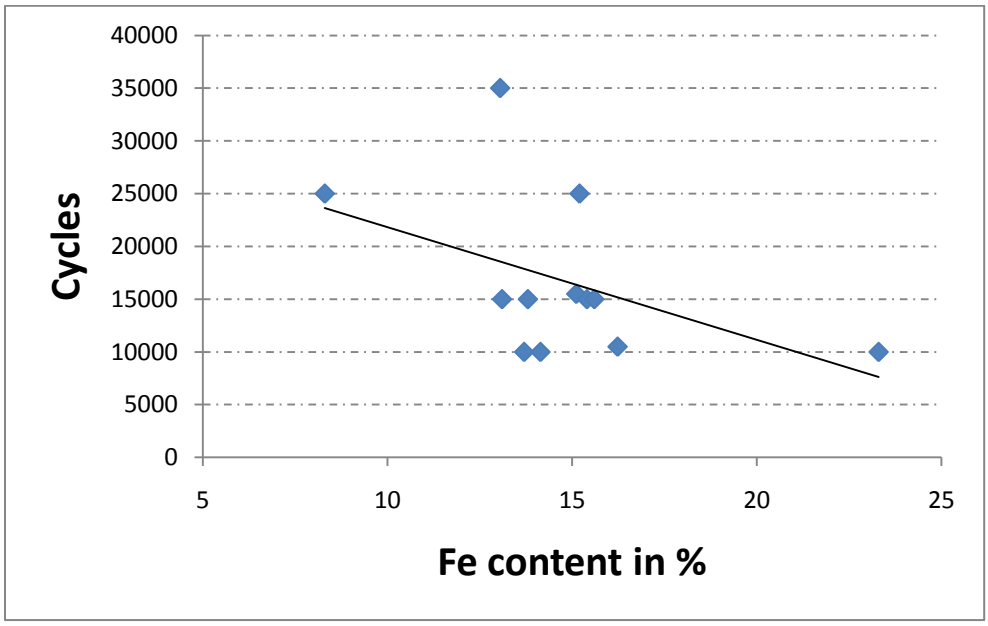

Figure 4.19: Life till crack propagates to the matrix from broken particles as a function of iron content in the particle for longitudinal samples.

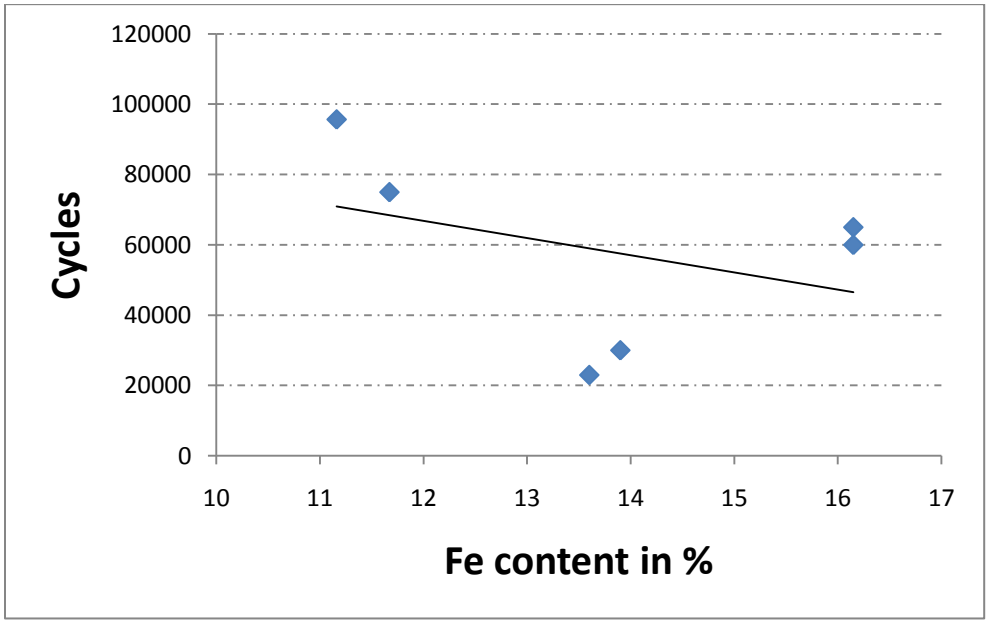

Figure 4.20: Life till crack propagates to the matrix from broken particles as a function of iron content in the particle for transverse samples.

The data in figure 4.19 and 4.20 show a decreasing trend for life as the iron particle content is increased. Since particles break very early, the amount of iron does not influence total life of samples. However, amount of iron does control the size of particles and the initial flaws created upon their fracture do impact fatigue life.

As mentioned earlier, 63 iron bearing particles fractured on the longitudinal samples compared to the 41 particles that fractured on the transverse samples. This discrepancy could be attributed to the geometrical orientations of the particles with respect to the applied load. Figures 4.21 and 4.22 show a particle about 28 um in height and 10 um in width oriented along longitudinal and transverse directions respectively. The dimensions were chosen to mimic the aspect ratio of 2.8 from tables 4.2 and 4.4.

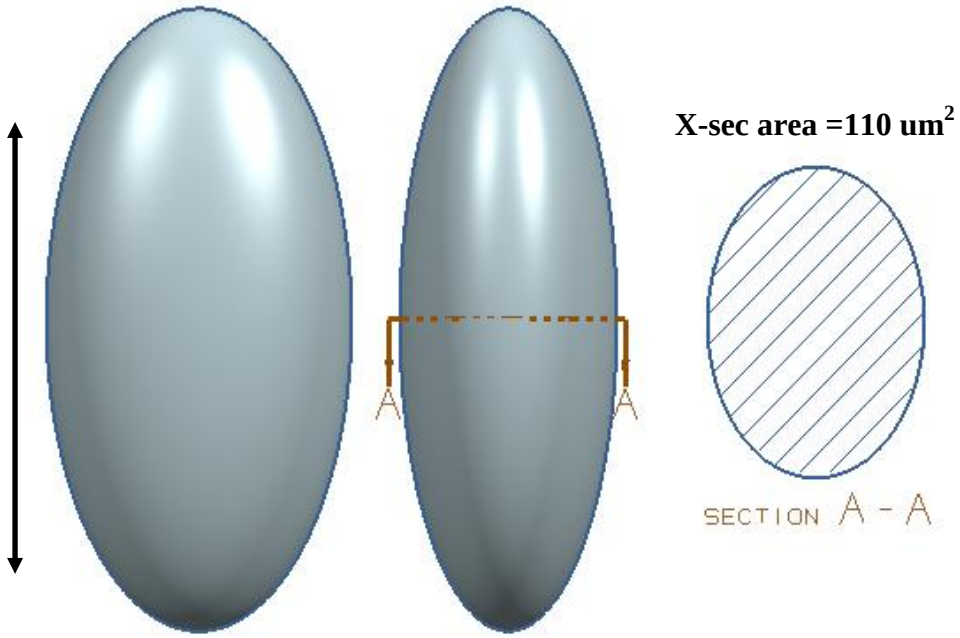

Figure 4.21: Particle shape with respect to the loading axis for longitudinal samples. Black arrow shows rolling and loading direction.

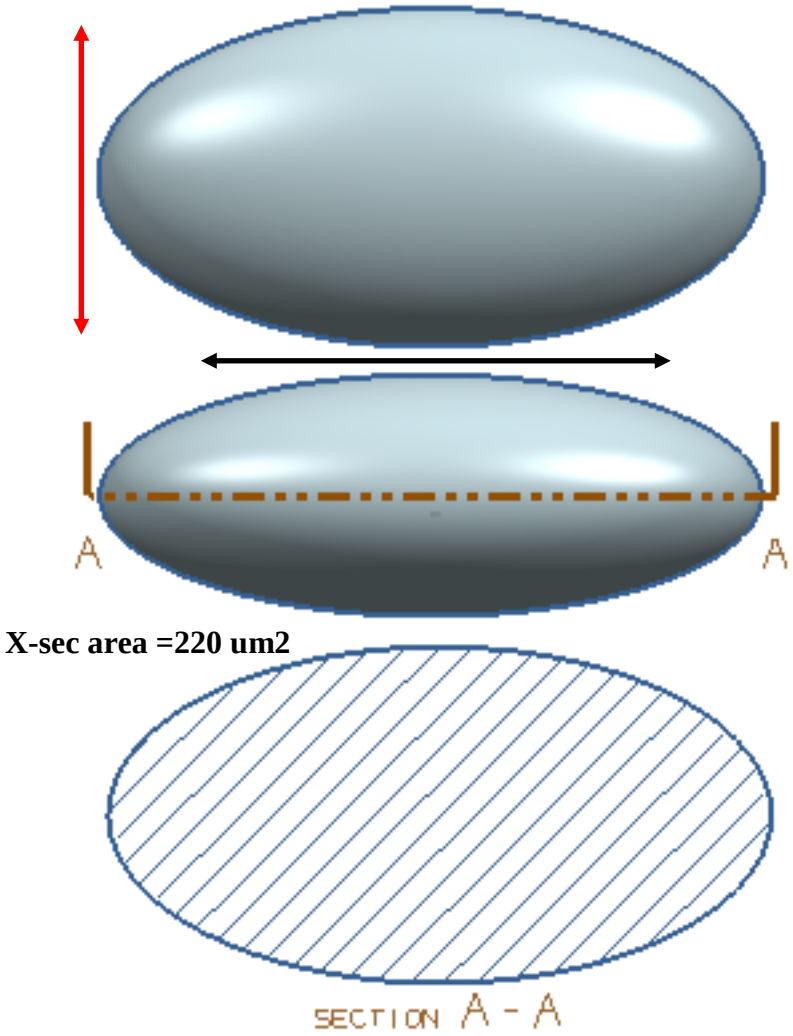

Figure 4.22: Particle shape with respect to the loading axis for transverse samples. Black arrow indicates rolling and red arrow indicates loading direction.

Based on particle geometry and orientation with respect to the material directions, inclusions have larger cross sectional areas in the transverse direction. For the case of the inclusion in figures 4.21 and 4.22, the cross section area is twice as large for the transverse orientation. The increased area acts to reduce the stresses imposed on the particle by the far field loads and in turn minimizes the occurrence of fractured particles.

Furthermore, for the case of particle orientation in figure 4.21, loads generated by the shear stresses at the particle/matrix interface are transferred more effectively to the cross-section of the inclusion since the major axis of the particle is parallel to the rolling direction.

4.1.3 Dogbone Sample Fractography

Scanning electron microscopy of the fracture surfaces normal to the load revealed mostly semi-elliptical cracks. In some instances shallow semi-elliptical cracks were observed (ref. figure 4.23) where crack depth “a” is smaller as compared to the length “c” of the crack on the notch surface.

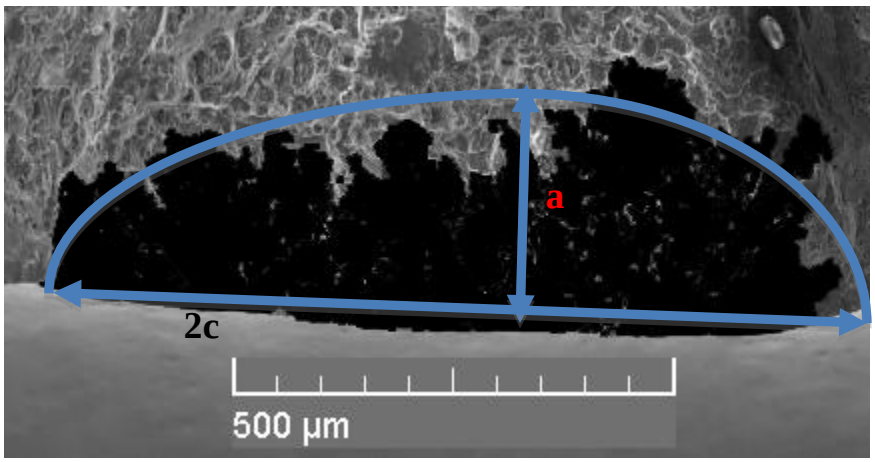

Figure 4.23: Shallow semi-elliptical crack topography.

Figure 4.23 also shows the irregular crack front that is typical for short cracks due to heterogeneity in crack growth due to variability in local crystallography. Instances where cracks initiated in the corners between the notch and sample surface yielded quarter circle cracks. Findings of semi-circular and quarter circular crack shapes are in accordance with observations of previous studies (Lankford, 1982; Newman and Edwards,

1988). Figure 4.24 shows typical crack geometries observed on the longitudinal and transverse samples respectively.

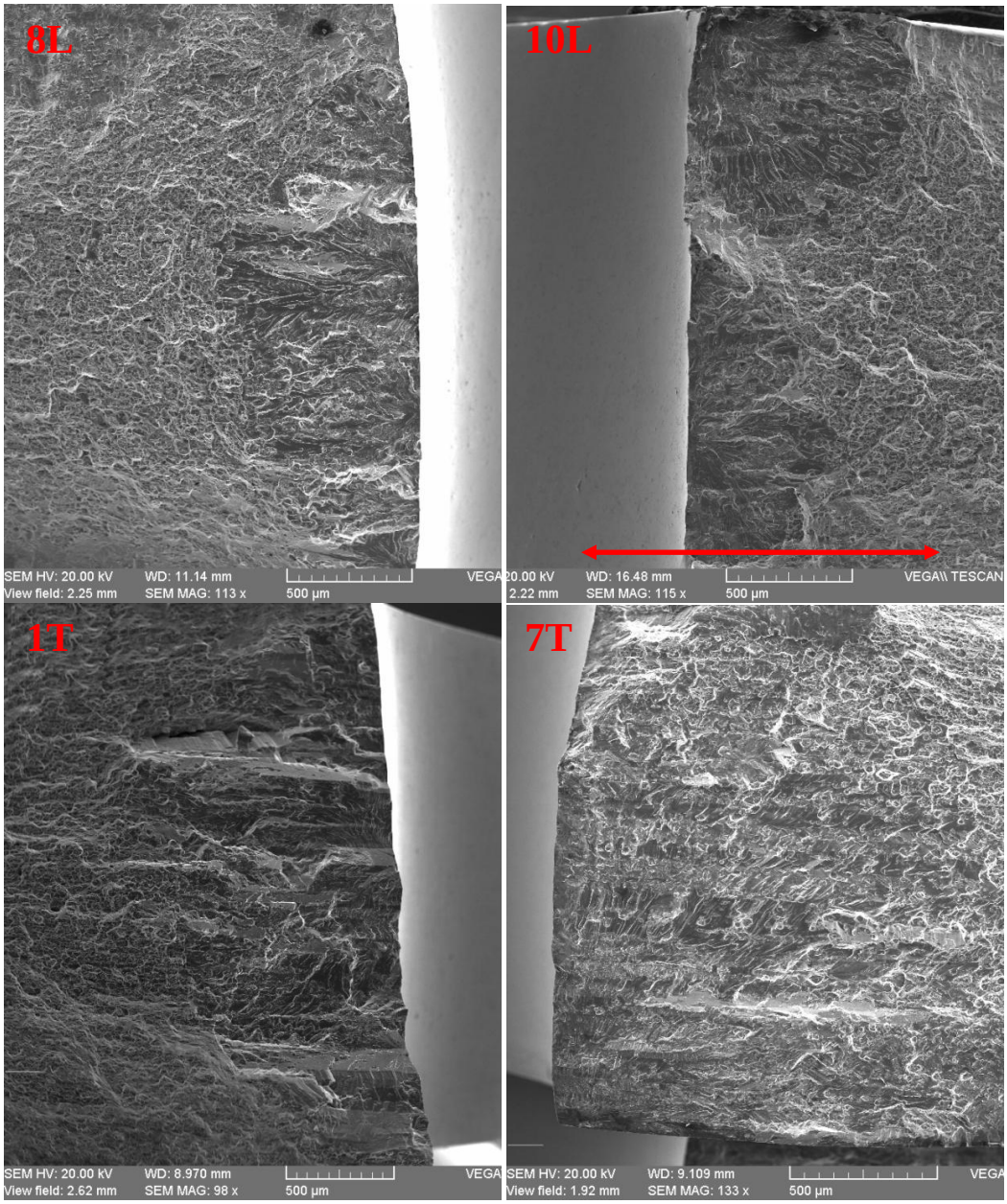

Figure 4.24: Various fracture surfaces for longitudinal and transverse samples. Rolling direction for transverse samples indicated by red arrow. Rolling direction for longitudinal samples is normal to the page.

One immediate difference among the fracture surfaces between the longitudinal and transverse directions is the amount of planar crack

growth. This disparity is quite clear when looking at pictures for samples 8L and 1T. It is obvious that increased planar growth in the transverse samples is influenced by the elongation of the grains due to rolling. In fact, many instances of planar crack growth for distances of 500 μm or longer are evident in the transverse samples, which correlate well with average grain sizes observed in the EBSD scans for the alloy used. It is safe to conclude that favorably oriented grains fracture along preferentially oriented crystallographic planes. The faceted regions of crack growth are most likely a result of environmental effects. Results from the literature indicate that suspect planes are most likely either {100} or {110} oriented planes, as well as orientations in between those two normals, which are often associated to rolled aluminum alloys (Garrett and Knott, 1975; Nix and Flower, 1982; Ro et. al., 2007; Ro et. al., 2008). More detailed discussion is offered in subsequent section.

Using the weight function approach (Glinka, 1996), stress intensity factors (K) were calculated for the crack profiles seen in Figure 4.24. The weight function method was preferred since the equations accounted for the thickness of the samples, which on average was about 3.56 mm. The results of the calculations are shown in Table 4.6. Sample 10L has two crack initiation sites; one quarter-circular and another semi-circular. Stress intensity factors calculated for both crack shapes assume no interaction between the two cracks. Stress intensity values were calculated at the deepest point where K values are the highest for these types of cracks.

Loads used were 363 MPa for longitudinal and 337 MPa for transverse samples.

Table 4.6: Stress intensity calculations for crack profiles shown in figure 4.24.

Samples	Depth "a" (μm)	Length "c" (μm)	Stress Intensity Factor K (MPa*m^1/2)	Crack Type
2L	254	492	14.4	Semi-elliptical
8L	794	913	30.0	Semi-elliptical
10La	493	479	19.0	Semi-Elliptical
10Lb	832	853	25.2	Quarter-Elliptical
1T	1102	1144	44.0	Semi-Elliptical
7T	1357	1380	33.1	Quarter-Elliptical
18T	1043	963	27.2	Semi-Elliptical

Calculated stress intensity factor values are quite high once the crack size exceeds 1 mm. This result seems reasonable because sharp increases in crack growth rates occurred and samples were observed to fail soon after the crack length reached 1 mm. The reported fracture toughness for Al 2024-T351 ranges between 40.5-37 MPa.$m^{1/2}$ and fracture toughness is being readily approached as crack size reaches and exceeds 1 mm (ASM Metals Reference Book, 1993; Metals Handbook, 1990).

During the fractography analysis, depth of the failure inducing particles was also gathered. Average depth of particles for longitudinal and transverse samples is tabulated in Table 4.7. There were 18 and 9 particles evaluated for longitudinal and transverse directions, respectively.

Table 4.7: Depth in μm of fractured particles on fracture surface for longitudinal and transverse samples.

	Longitudinal	Transverse
Average	14.6	22.3
Standard Deviation	5.0	11.5

As expected, the depth dimension is on average larger in the transverse directions when compared to the longitudinal samples. This is mainly due to the fact that the rolling direction is parallel to the depth direction for the transverse samples. Surprisingly, average height (direction parallel to the rolling direction) of longitudinal particles is not considerably larger than the depth dimension. The average height is 16.7 μm, which is only 2 μm greater when compared to the depth results in Table 4.7. This could be a due to sectioning bias since only 2-D projections of the particles are measured and the actual height of the particle is probably larger. Referring back to figure 4.21 the probability of getting the max 2-D projection at the free surface is very small (especially for the height dimension) since change in height is steep as we move perpendicular to the rolling direction. It was expected that the average height of the transverse direction would match the depth results of the longitudinal direction. Indeed the results did match where average height in transverse direction is 14.7 μm, which closely matches the value of 14.6 μm for the depth of longitudinal particles. Not surprisingly the average depth of the transverse particles exceeds the height, as expected. Figure 4.25 illustrates some of the broken particles on the fracture surface of longitudinal and transverse samples.

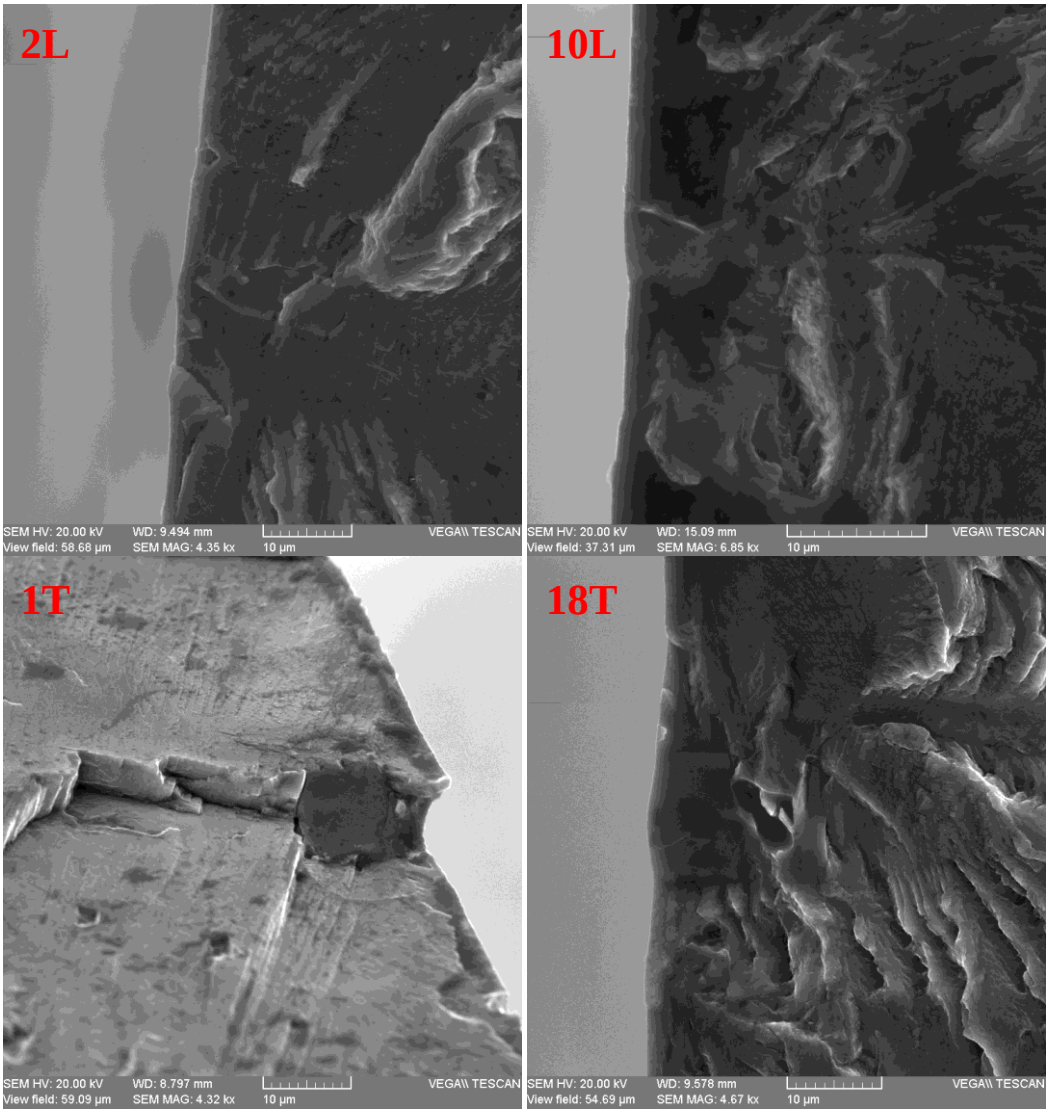

Figure 4.25: Broken particles on the fracture surface for various longitudinal and transverse samples.

4.1.4 Dogbone Crystallography Results

Before cyclic testing, two dogbones (8L and 17T) underwent electron backscatter diffraction to elucidate the grain structure of the notches and to identify the crystallography of grains involved in crack initiation and initial propagation. The EBSD maps were superimposed on the fracture photographs, which allowed correlating the crack initiating

location and the neighboring grain crystallography. Figure 4.26 shows the superimposed pictures.

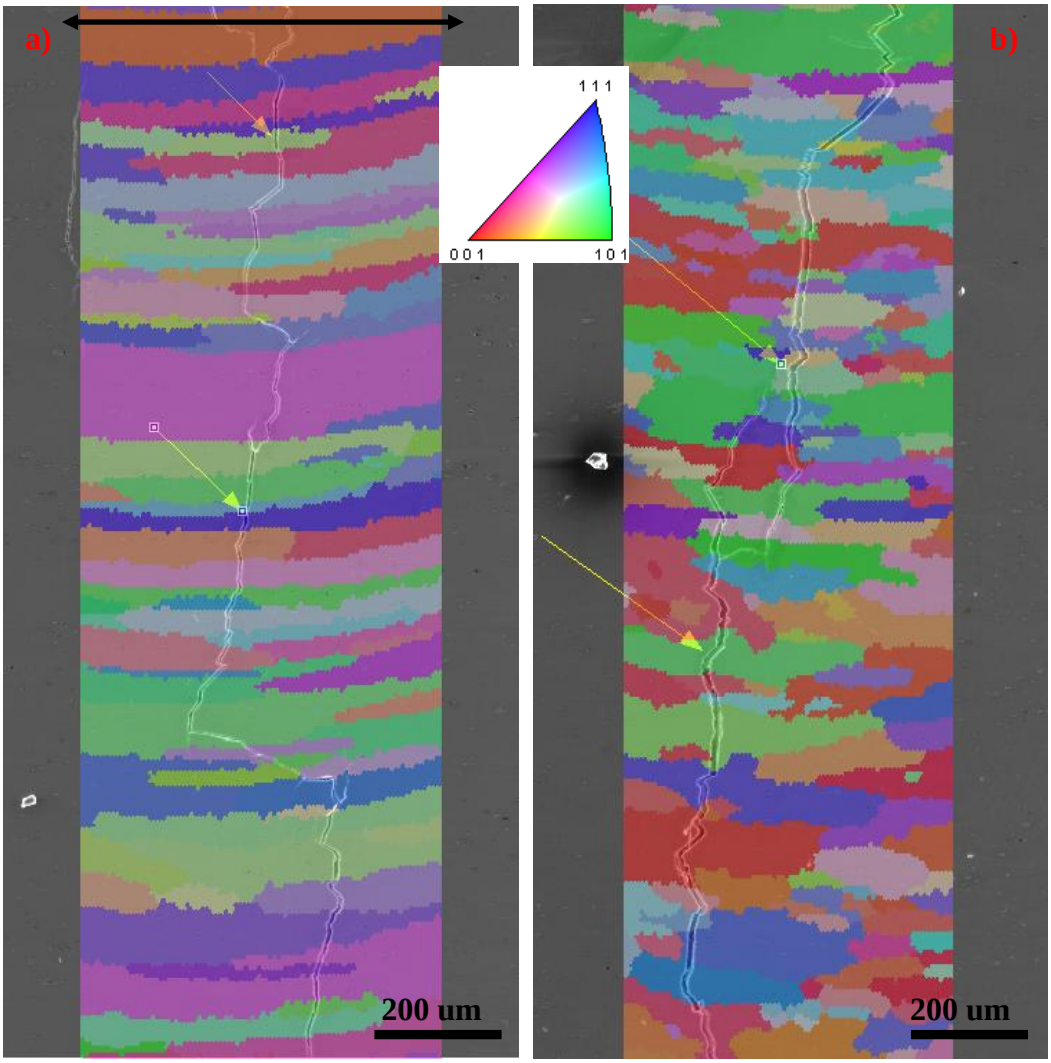

Figure 4.26: Superimposed EBSD inverse pole figure maps on notch fracture images of samples (a) 8L and (b) 17T. Yellow arrows indicate crack nucleating location and the black arrow indicates the loading direction.

Crystal directions in the crack initiating grains were measured along the direction parallel to the load, which is indicated by the black arrow. The resulting crystal directions were plotted on the standard stereographic triangle shown in figure 4.27.

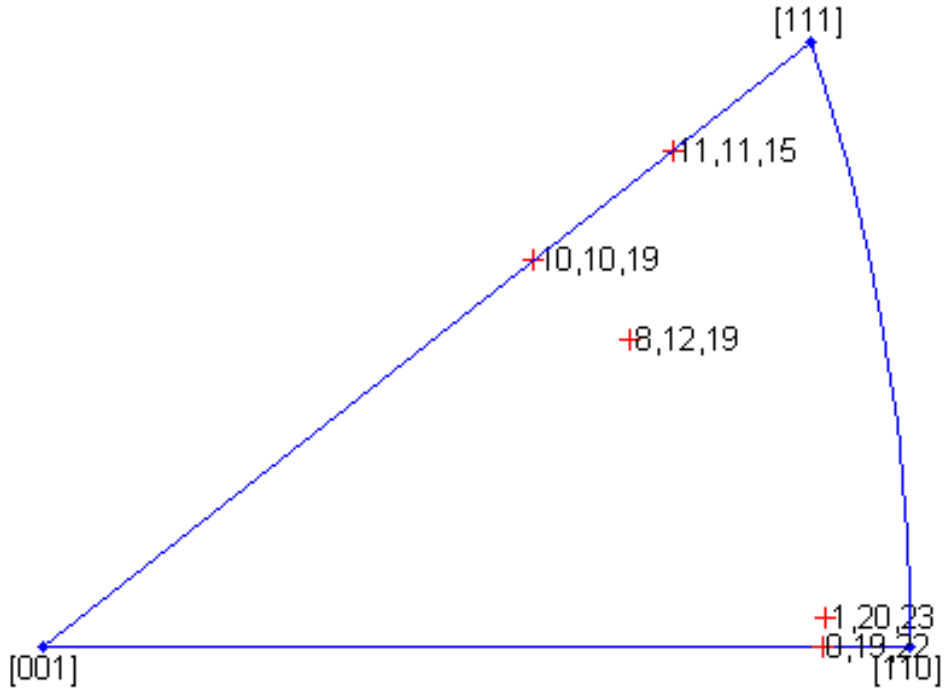

Figure 4.27: Crystal directions parallel to the applied load for grains where cracks initiated.

Results indicate that the loading direction of the grains with crack initiation sites corresponded to both double slip and single slip situations. Moreover the projected directions group closely to the <111> and <110> orientations. It has been observed in prior studies that {111} planes are primarily responsible for crack propagation in high vacuum cyclic tests, while in the presence of environmental effects crack growth can be along the {110} planes. (Ro et. al., 2007; Ro et. al., 2008; Gupta and Agnew, 2011). However, the crystal directions plotted parallel to the load in figure 4.27 do not necessarily correspond to the planes mentioned above because of the measurement technique used. Crystal directions were obtained by looking down onto the notch as depicted in figure 4.26.

Therefore, the actual orientations of the fracture planes are not clearly defined unless direct observations are made on the fracture surface as was the case in the studies performed by Ro et. al. (2007, 2008) and Gupta and Agnew (2011). The double slip directions [11 11 15] and [10 10 19] are 8.7 and 18.1 degrees away from the the [1 1 1] direction. Fracture directions this close to the [1 1 1] direction only occurs in high vacuum environments where environmental effects are virtually eliminated (Ro et. al., 2007; Ro et. al., 2008). However, fatigue testing of the dogbones was performed under conditions such that environmental effects must certainly be present. Therefore, it is highly unlikely that fracture took place on planes close to the {1 1 1} orientation. A more likely explanation is that particle geometry at the nucleation sites encouraged the crack growth along the measured crystal directions; therefore, making it appear that the crack growth took place normal to the [1 1 1] direction. The fractographs in figure 4.28 show the fracture surface at the nucleation site for both 8L and 17T, which correspond to the double slip directions plotted in figure 4.27.

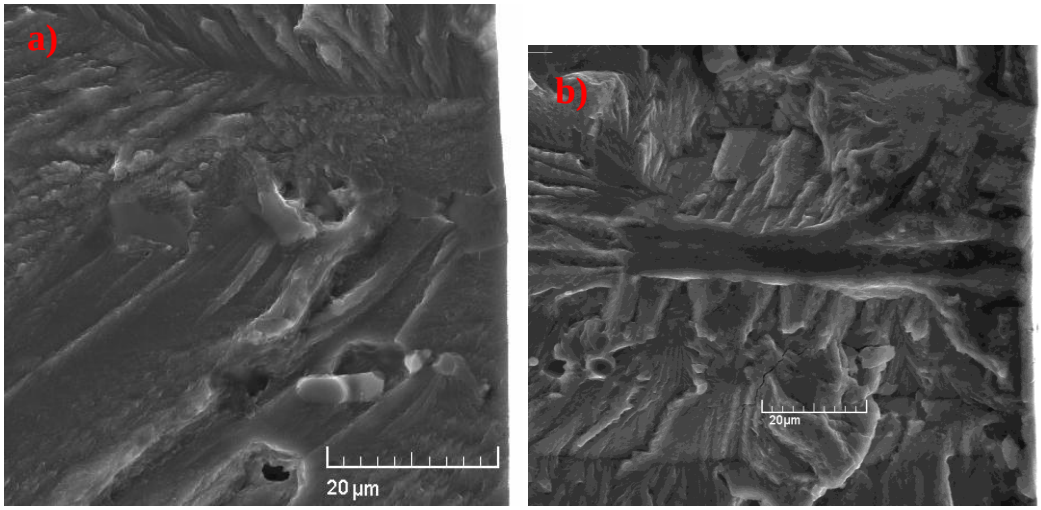

Figure 4.28: Particle depths for a) 8L and b) 17T at the sites corresponding to the double slip directions.

Particle depth dimensions are 50 µm and 71 µm for 8L and 17T, respectively. Inclusions of this size could undoubtedly drive the crack growth perpendicular to the [1 1 1] direction in the vicinity of the particle. Regarding results close to the <110> direction, the load axes parallel to [1 20 23] and [0 19 22] are 4.4 and 4.2 degrees away from the [1 1 0] direction. In this case, the directions near [1 1 0] are expected because of the environmental effects; however, because of the measurement technique employed, there is no guarantee that fracture is taking place along the {1 1 0} planes. On the other hand, the probability that the obtained directions near the [1 1 0] pole are a coincidence is very low. Since the initial short crack growth is crystallographic, there is a good probability that the plotted crystal directions near the [1 1 0] pole are indeed the normals to the plane of crack growth.

4.1.5 Dogbone Vickers Hardness Testing

In section 3.1.1, it was mentioned that some transverse samples were tested up to 800,000 cycles without failure or any indication of matrix fracture despite the presence of broken particles. It is suggested that this outcome could result from compressive stresses generated due to tensile plastic strains in the notch, as a result of loading the samples at values of stress that are slightly higher than the local yield strength at the tip of the notch. It is possible that inherent heterogeneity of the plate from which samples were machined varied the yield strength properties as a function of position on the plate. Table 4.8 tabulates tensile test results of the longitudinal and transverse samples.

Table 4.8: Tensile test results for longitudinal and transverse direction. Five samples were tested in each direction.

	Longitudinal	**Transverse**
Average	363 MPa	337 MPa
Standard Deviation	12.5 MPa	8.6 MPa

All the samples were tested at the average values given. Given the scatter measured from the tests, it is certainly possible that some of the tested transverse samples could posses a yield strength below the average value, which would generate higher than normal plastic strains in the notch region, particularly if one takes into account the fact that the stress-strain curve for the material is fairly flat after yielding, i.e., a small amount of stress above yielding can lead to significant amounts of plastic strain. Since the first cycle in the tests was set to always be in tension, the resulting residual stress would be compressive, in turn reducing the

applied stress on the notch area. If significant plastic deformation is present, the material around the notch should have higher hardness when compared to material away from the notch region. Vickers hardness testing was performed on subject samples that showed the long fatigue lives near the notch region and away from it. Hardness values for the low stressed region was used as a control and compared to the hardness in the high stressed region. Total of 19 and 24 data points were collected for the low stress and notch regions, respectively. Table 4.9 shows the results of the hardness testing.

Table 4.9: Vickers hardness results for the notch and low stress areas.

	Notch region	**Low stress region**
Vickers hardness	160±8	143±5

The result suggests that plasticity is indeed present in the notch regions of the samples that showed unusually long life. Increase in plasticity in the notch areas is a reasonable explanation to the observed results. However, it should be noted that longitudinal samples did not experience the same phenomenon even though the variance in the yield strength was higher when compared to the transverse samples.

4.2 Cruciform Results

4.2.1 Fatigue Performance

All the cruciforms were tested at the yield strength in the transverse direction. As pointed out in the experimental setup section, the main purpose for the use of cruciforms is the ability to evaluate strength properties of many crystal directions in one test. This procedure should

yield the crystal directions that are most prone to fracture. Moreover, the sample geometry allows for the evaluation of the effects macroscopic anisotropy present in the 2024-T351 Al alloy due to rolling, since the tangential uniaxial stress around the hole probes all physical directions in the plane of the plane simultaneously. Later it will be seen, with one exception, that the cruciform samples tend to propagate cracks either along the longitudinal or transverse direction. All the fatigue cracks initiated from broken iron bearing particles. Only a few instances of debonding were observed, but the debonded particles were not responsible for any crack nucleation in the matrix. Fatigue life till the crack initiated in the matrix and the total life of samples are shown in Table 4.10.

Table 4.10: Fatigue lives of cruciform specimens.

Cruciform	**Life till matrix crack**	**Fatigue Life**
C-1	50,000	163,000
C-2	50,000	150,000
C-3	90,000	191,000
C-4	70,000	n/a
C-5	90,000	232,000
C-6	100,000	230,000
C-7	100,000	185,000

Cruciform C-4 experienced an overload during the test. Therefore, further testing was invalid because of the significant increase in plastic deformation in the gage area. However, the sample still provided information about crack nucleation sites. An obvious difference in fatigue life is evident between C-1 and C-2 and all other samples. Samples C-1 and C-2 initiated cracks and failed earlier than samples C-3 thru C-7; in all likelihood, this result is due to the fact that samples C-1 and C-2 came

from a different Al 2024-T351 plate. One immediately recognizable difference between the two plates is the size of the constituent particles. Samples C-1 and C-2 on average had larger particles when compared to the remaining samples. Average particle height and width for the 7 cruciforms is tabulated in table 4.11.

Table 4.11: Particle dimensions for cruciform samples.

	Particle Height (um)	**Particle Width (um)**	**# of Particle Analyzed**
C-1	27.0±16	8.6±3	5
C-2	25.3±12	8.0±4	10
C-3	15.7±5	5.4±2	10
C-4	17.6±6	7.0±3	13
C-5	11.7±3	3.4±1.5	11
C-6	14.5±5	5.2±3	11
C-7	11.1±8	4.0±2	11

For sample C-1 only 5 particles were identified on the crack path. The reason for this is still unknown but C-2 , which comes from the same plate had twice the number of fractured particles on the crack path. Samples C-1 and C-2 have a larger deviation in particle dimensions but the large variance seen for C-1 could be attributed to the low number of particles examined. The impact of the particle sizes on fatigue life is more evident when fatigue life is plotted as a function of particle size, as was shown for the uniaxial specimens. Figures 4.28 and 4.29 plot particle height and width versus fatigue life for all samples.

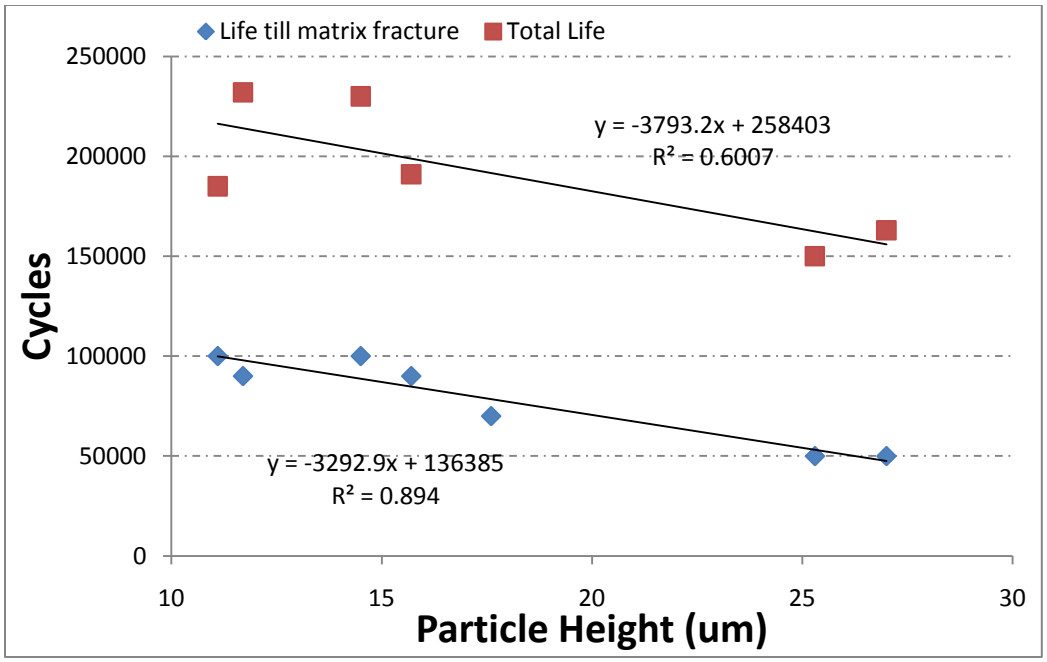

Figure 4.29: Plot of fatigue life as a function of particle height.

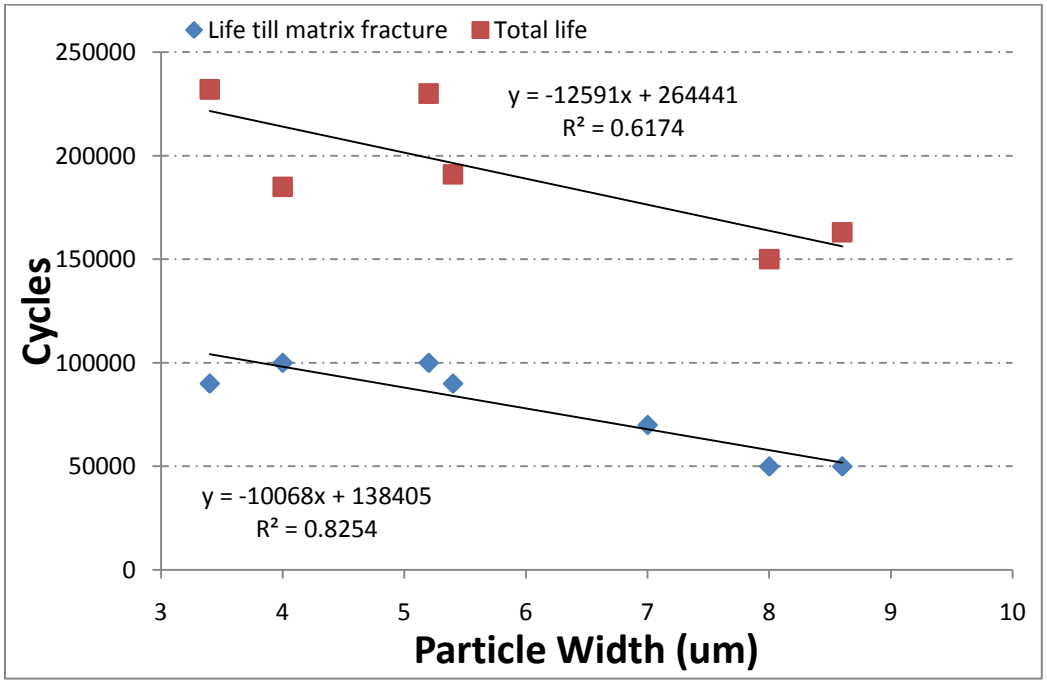

Figure 4.30: Plot of fatigue life as a function of particle width.

Trends in figures 4.29 and 4.30 correlate well with results for the dogbone samples (Figures 4.6 thru 4.9). It has been shown for dogbones that

fatigue life is reduced as particle size is increased; a similar trend also present for the cruciforms. Moreover, cruciforms show a better fit for the life till matrix fracture than the dogbone data. It is also desirable to see if particle size has any influence on crack propagation once the crack is nucleated. Therefore, plots 4.31 and 4.32 were constructed that plot fraction of total life for which crack is nucleated and propagating versus particle size (i.e., total life – life till matrix fracture).

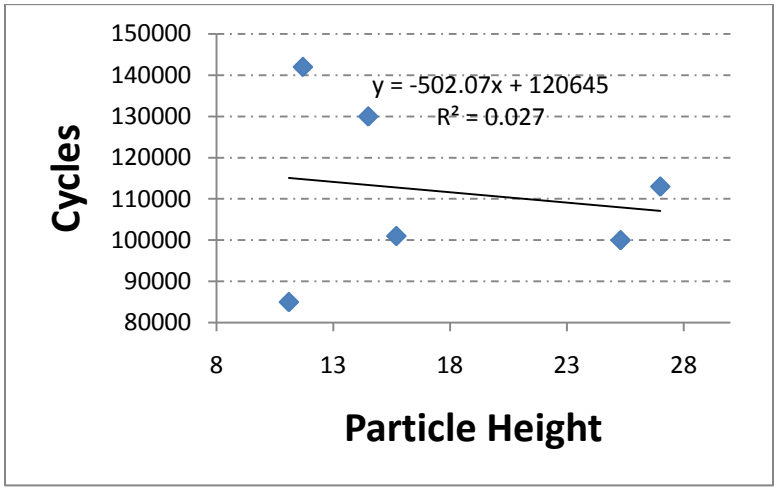

Figure 4.31: Fraction of life in which crack is in the propagating regime versus particle height.

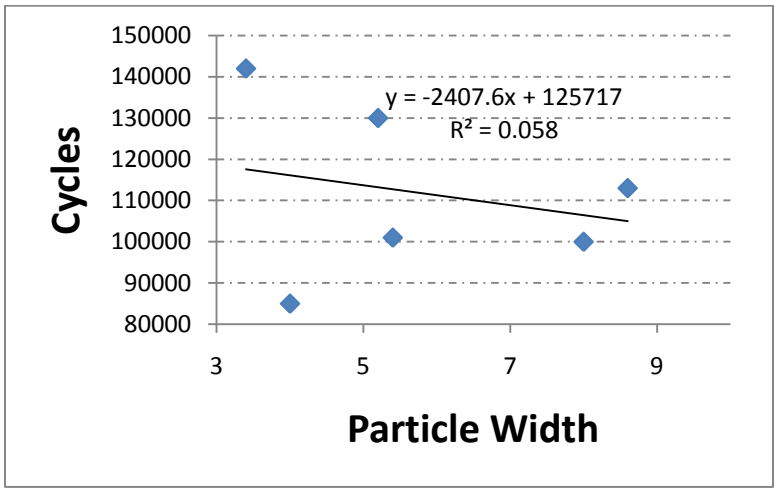

Figure 4.32: Fraction of life in which crack is in the propagating regime versus particle height.

The relatively flat trend coupled with a poor fit show that particle size has very little influence on the growing crack once the crack is formed in the matrix. This further implies the shift in fatigue controlling factors from particles to material crystallography as the main factor behind the crack growth kinetics. Therefore, crack growth can be divided into 2 regimes. Regime one deals with crack nucleation where particle morphology governs the life till matrix fracture. Once the crack is nucleated, the crack transitions into regime two where further crack growth behavior is governed primarily by the material crystallography.

Another differing factor between the two plates is the average grain size. On average, the grain size for samples C-1 and C-2 is 283,972 um^2 and 309,891 um^2 for all other samples. It has been observed in previous studies that larger grains tend to slow crack propagation due to increased crack tortuousity (Li, 2006). This effect could also have contributed to the increased fatigue lives of samples C-3 thru C-7. The results shown above bring to question the validity of only relying on material specification currently used in the industry. Both plates were certified to various AMS, ASME, MIL and SAE standards; however, their fatigue performance was dissimilar. Findings such as these as well as others in the community, e.g., Brockenbrough et. al., (1993), would suggest that modifications to current specifications need to be incorporated to attain more consistent fatigue performance between different metal manufacturers.

No unique fracture direction was observed on the tested samples. However, majority of crack growth took place along the longitudinal and transverse material directions indicating the influence of macroscopic anisotropy on crack growth directions. Figure 4.33 shows the observed crack orientations relative to the rolling and transverse directions. Axes depict the rolling (RD) and transverse (TD) inside figure for C-1 and can be used as a reference to determine material directions for the remaining samples.

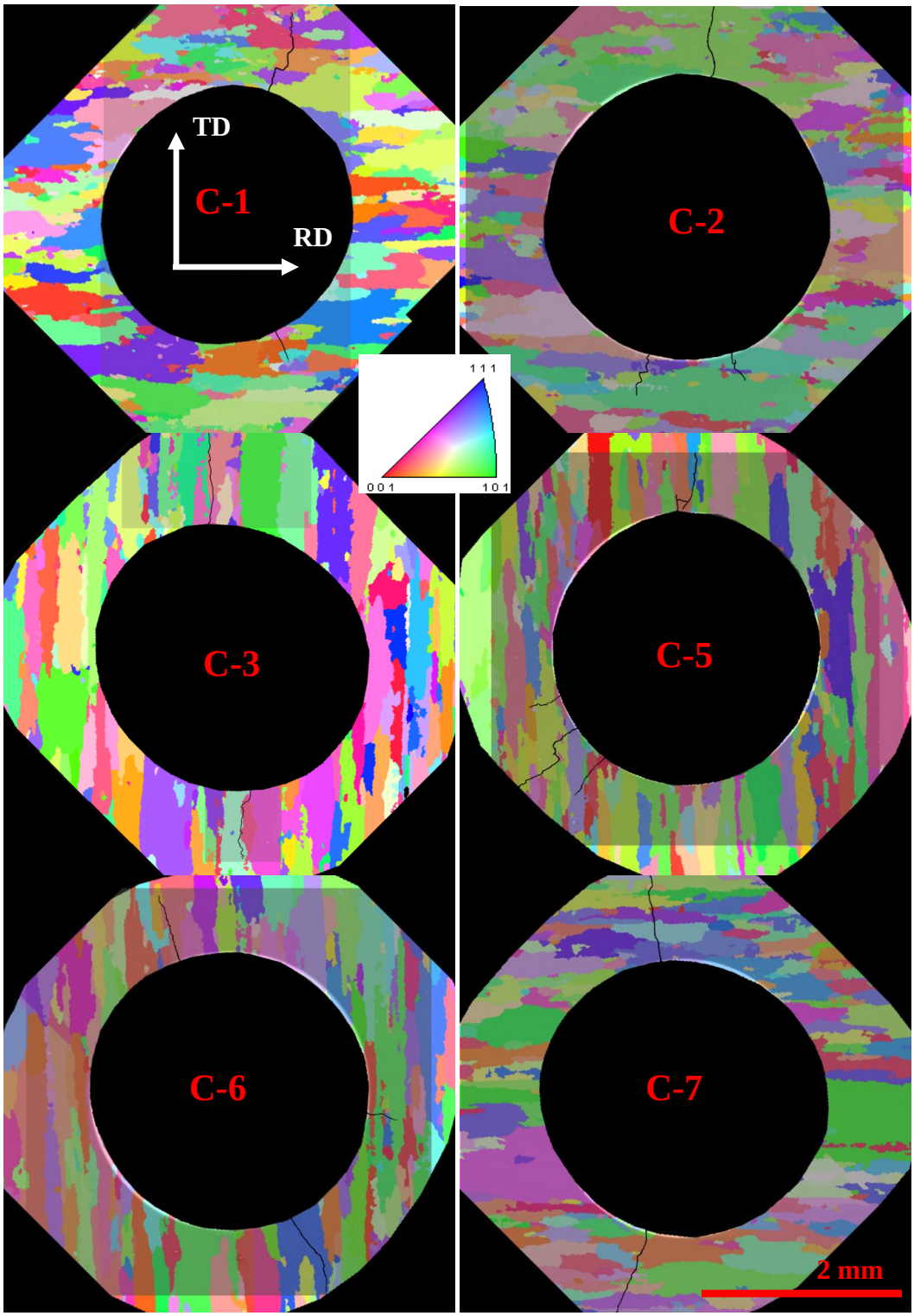

Figure 4.33: Superimposed crack profiles on the EBSD maps for all cruciforms except C-4.

Samples C-1, C-2 and C-7 initiated failure inducing cracks parallel to the transverse direction. Samples C-3 and C-6 grew cracks in the rolling direction with sample C-6 also containing a smaller crack along the transverse direction. Sample C-5 had one of the main cracks grow along the rolling direction and the other one was at 45 degrees from the rolling direction. A closer look was taken at the texture plots for sample C-5 along longitudinal, transverse and diagonal (45 degrees to rolling direction) directions in hopes to explain the occurrence of fracture at 45 degrees. The analysis of the texture plots yielded no intrinsic material properties to explain the phenomenon. However, the plot of crystal directions parallel to the loading axes for all featured cracks did show some noteworthy trends. The plotted crystal directions can be seen in figure 4.34.

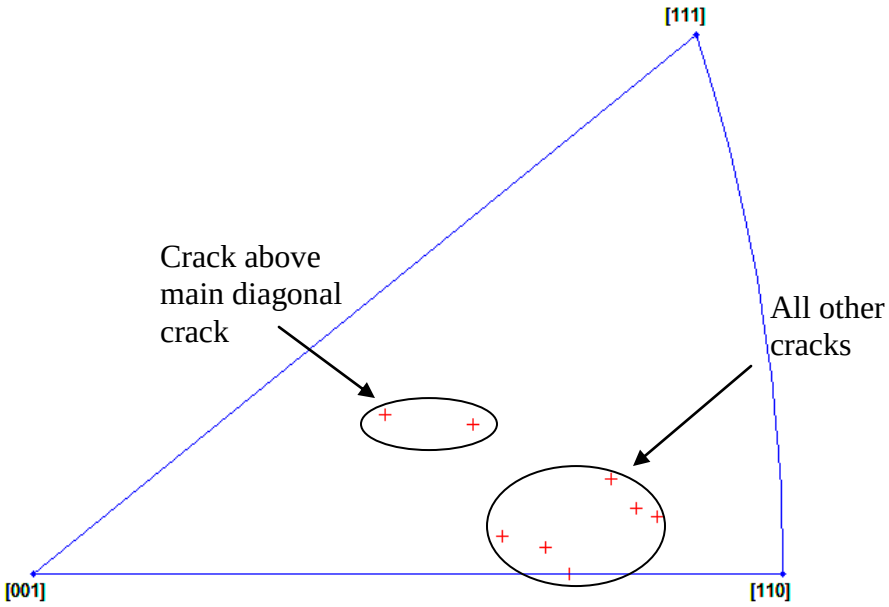

Figure 4.34: Crystal directions parallel to the loading direction for all cracks in samples C-5.

Even though the cracks were growing along different physical directions, the plotted crystal orientations for the main longitudinal and diagonal cracks are similar. This suggests that crystal orientation, e.g., local anisotropy, could be more influential on crack nucleation than global anisotropy due to rolling in this case. The fact that the crack was not growing in the opposite longitudinal direction, as was the case for samples C-3 and C-6, suggests that no favorably oriented grains were present at the corresponding location or the particles were not sufficiently damaging to initiate cracks there, or a combination of both. In fact, the opposing longitudinal side where the crack was expected to grow showed markedly reduced number of broken particles. This could imply a decrease in influence of global anisotropy. Additional analysis needs to be done on particle geometries and grain crystallography in order to confirm the statements made above. However, results gathered thus far suggest that the process for fatigue crack nucleation is governed by the competition between local and macroscopic anisotropy, and C-5 is an instance where local anisotropy was more influential. The fact that other samples failed in either longitudinal or transverse directions indicates a strong influence of global anisotropy due to rolling.

Cracks usually initiated inside the hole within about 20-50 μm of the gage face. The crack grew at a moderate rate until the crack spanned the entire thickness of the gage area. Once the crack spanned the thickness, crack growth rate increased sharply and few additional cycles were needed to

propagate the crack to 1 mm. In most cases, once a crack initiated in the hole near the top surface, a secondary crack would form in the hole near the opposing bottom surface and the cracks would grow toward each other until coalescence. This process was most prevalent in samples C-1 and C-2. Moreover, once crack initiation occurred on one side of the hole an opposing crack 180 degrees apart from the initial crack would form and grow in the opposite direction. This can be seen clearly in Figure 4.33 for all samples except perhaps for sample C-5 where the opposing cracks are less than 180 degrees apart. Note that one could speculate that perhaps the creation of the first crack perturbed the stress field around the hole and caused favorable stress conditions on the opposing side that encouraged crack nucleation. To study the effect of crack presence on stress distribution around the bore two types of crack geometries were examined using finite element analysis via a linear elastic model, as shown in figure 4.35. The first crack geometry is quarter-elliptical and located on the corner between the bore and gage face surfaces as shown in figure 4.35b. Dimensions chosen for the quarter-circular crack are meant to resemble typical crack sizes at the time the opposing crack 180 degrees apart from the initial crack would form. The crack going through the thickness and the gage face length are shown in figure 4.35b. The second geometry resembles a crack that propagated through the whole thickness of the sample. The crack length on the gage face remains 250 μm since little to no crack growth is observed on the gage face until the

crack grows through the thickness. The crack geometry for the second case can be seen in figure 4.35c. Finite element calculations (Figure 4.35e) showed no significant perturbation of the stress state in the side the hole opposite to the crack side for the quarter-elliptical crack. The simulation showed that, besides the immediate region around the defect, the stress distribution remained mostly unchanged. A second simulation was carried out with a crack-like defect that went through the entire thickness of the gage face (Figure 4.35f). In this case the stress perturbation was significant enough to produce a higher stress concentration on the opposite side of the hole. The second result suggests that it is indeed possible for a crack on one side of the hole to disturb the overall stress distribution around the notch and generate higher stresses on the opposite side of the hole.

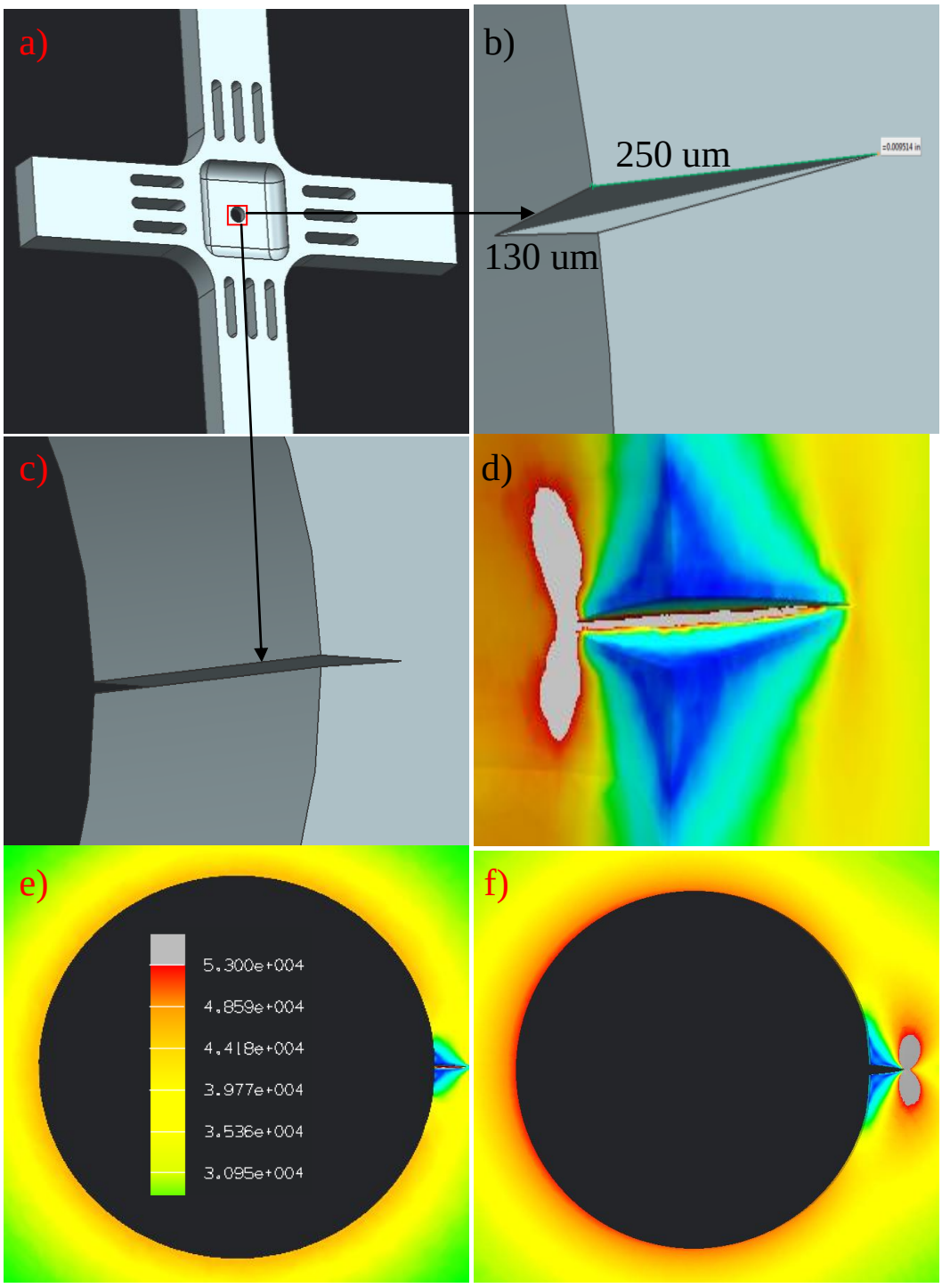

Figure 4.35: Finite element simulation of stress perturbation due to presence of a crack-like flaw on one side of the circular notch in the cruciform samples. Figures a-c show crack location and geometries and figures d-f show the simulation results, as described in the text. Gray areas indicated stresses above the yield strength of 2024-T351 in the T direction.

A convergence analysis via mesh refinement was attempted to further confirm the results, to make sure that there was enough resolution to capture any stress perturbation due to the flaws, particularly for the quarter-elliptical crack. Unfortunately, any further refinement to the finite element model used to obtain the results shown above would have exceeded the computational limit of the computer used for the analysis. Nonetheless, the lack of stress perturbation shown in figure 4.35e is consistent with Saint-Venant's principle, due to the small size of the flaw as compared to the hole size. Note that a perturbation of less than 10% of the stress level could still occur at the size of the hole opposite to the flaw, given the resolution of the legend used in the contour plots. However, this is certainly much lower than the perturbation induced by the through-thickness flaw. Figures 4.35 d and f further support the experimental observations discussed above regarding the behavior of the crack before and after it has propagated through the sample thickness, since a full through-thickness crack will lead to higher stress concentrations and stress intensities, and, consequently, to more damage.

Figure 4.35d shows that a higher crack driving force is present in the tip that is at the surface of the hole when compared to the opposite crack tip located on the gage surface. The simulation results are in agreement with the observation that the crack prefers to grow through the thickness first before propagating along the gage face. Figure 4.35f illustrates the large stress levels ahead of the crack once the crack propagates through the

sample thickness. This result agrees with the observations of increased crack growth rates once the crack grows through the thickness. In Figures 4.35 e and f, the stress in the hole away from the crack locations is comparable to the yield strength in the transverse direction.

4.2.2 Particle Chemistry Data

A total of 53 iron bearing and 14 soft particles were examined on all the cruciforms. As mentioned earlier only iron bearing particles were responsible for crack nucleation. Typical fractured particles can be seen in Figure 4.36

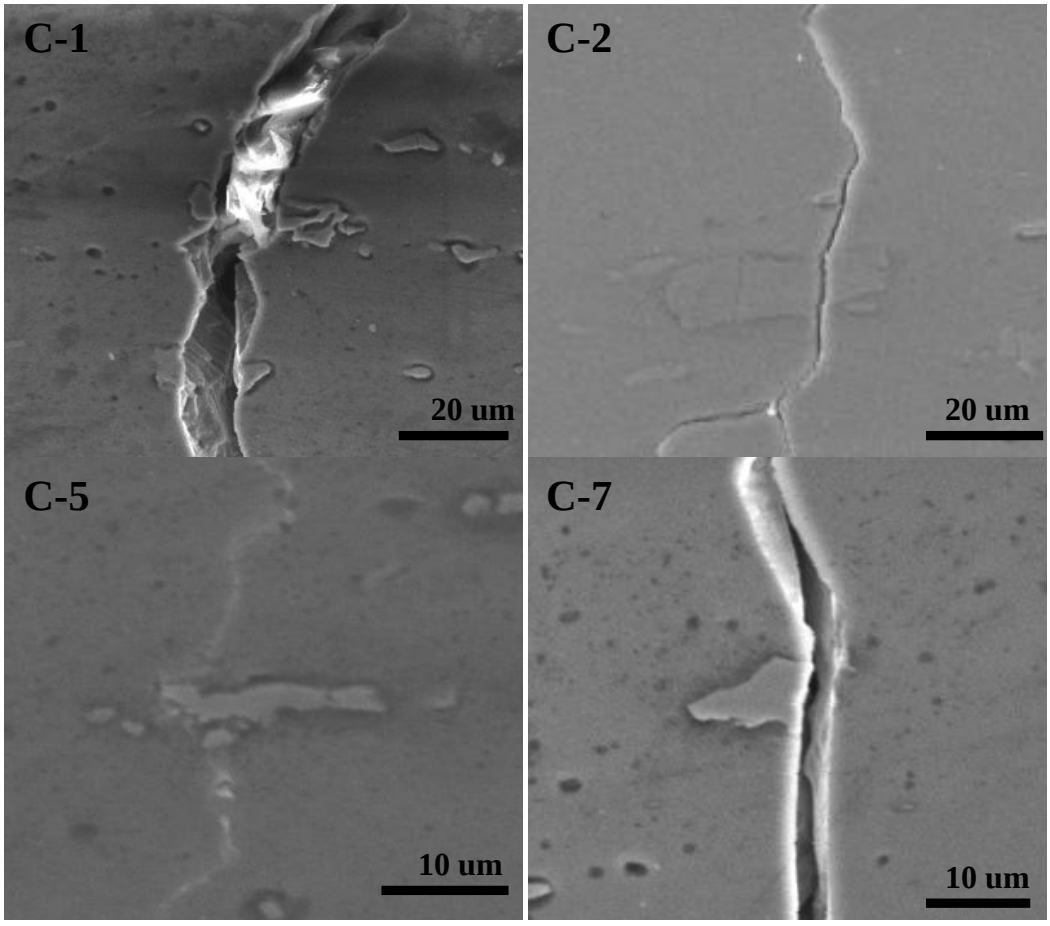

Figure 4.36: Typical iron bearing particles found on the crack path.

An attempt was made to acquire particle chemistry composition using the EDS technique, which uses detectors calibrated for use on flat surfaces. For the case of the cruciform samples, EDS analysis is performed on a curved surface due to the presence of the hole in the gage face. Great effort was made to obtain chemistry data at peak signal strengths of the detector. Even though the chemistry data are prone to errors they are still useful to evaluate trends and correlate chemical composition of particles to fatigue performance. Table 4.12 compares the average composition values of dogbones and cruciforms gathered by EDS.

Table 4.12: Comparison of particle chemical composition between dogbone and cruciform samples.

	at% Al	**at% Cu**	**at% Fe**	**at% Mn**	**at% Si**	**at% Mg**
Cruciform Fe particles	51	22	17	11	3	n/a
Cruciform soft particles	40	58	n/a	n/a	3	4
Dogbone Fe particles	59	14	15	9	5	2
Dogbone soft particles	54	43	n/a	n/a	n/a	5

Not surprisingly, some variance between the two sets of data is present. However, due to geometrical limitations and inherent inaccuracy of the EDS technique when it comes to quantification, the resulting data for dogbones and cruciforms is sufficiently close. Particle iron content for each cruciform was also averaged to investigate what sort of variance exists between individual samples. Moreover, since two plates were used for the manufacture of cruciforms, it was also desirable to see any differences in iron content between two material manufacturers. Individual cruciform iron content results are shown in Table 4.13.

Table 4.13: Average at% Fe content of particles in individual cruciforms.

	C-1	C-2	C-3	C-4	C-5	C-6	C-7
at% Fe content	19	20	19.0	16	13	15	14

Data in table 4.13 suggest on average lower iron content in cruciforms C-3 thru C-7 when compared to cruciforms C-1 and C-2. The result implies that the two plates do indeed posses varying content of iron despite the fact that iron is controlled in all the specifications for Al 2024-T351 plates. To see the impact of varying iron content on the fatigue properties, life till matrix fracture and total life are plotted vs. the iron content of particles for individual cruciforms, as shown in figure 4.37.

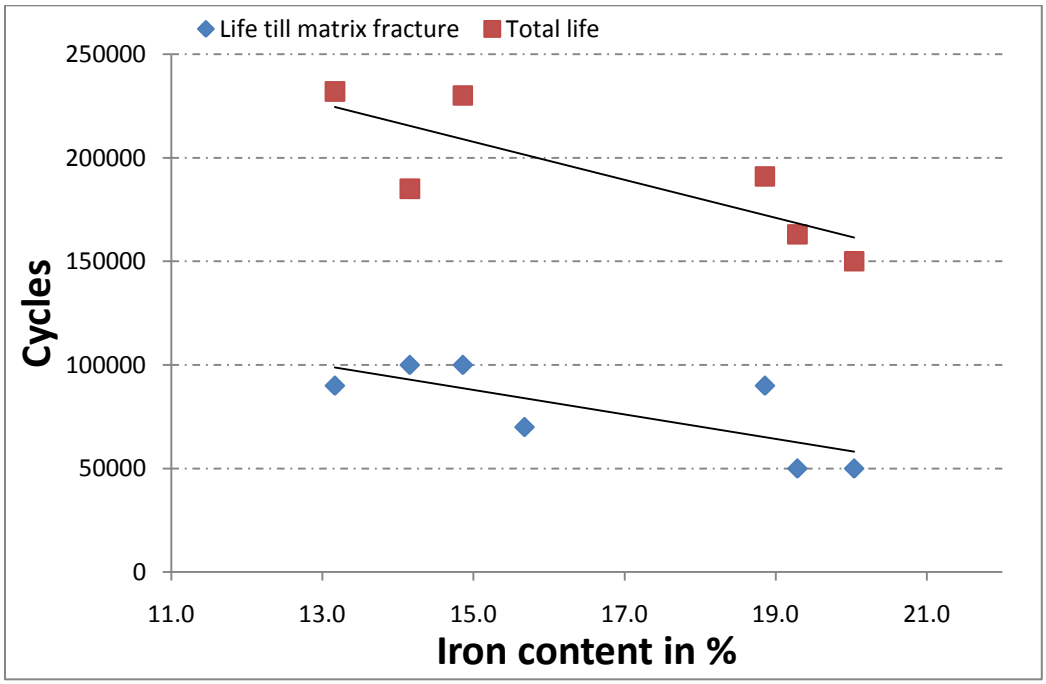

Figure 4.37: Effect of iron content on fatigue properties of cruciform samples.

Figure 4.37 shows a trend of decreasing life as iron content increases. Again, the iron content controls the size of the particles and larger particles generate bigger flaws that impact fatigue life in deleterious

fashion. Similar trend was observed for the dogbone samples for both the longitudinal and transverse specimens (Figures 4.19 and 4.20). Parallel trends have been reported in the open literature, which indubitably led to the creation of Al 2024 variants with lower iron contents such as Al 2124 and Al 2026 (Kung and Fine, 1979; Zhai, et. al., 2005).

4.2.3 Cruciform Fractography

Samples C-1 and C-3 were chosen for fractography analysis of the fracture surfaces. Samples were chosen based on the location of main cracks with respect to the rolled direction. Sample C-1 main cracks grew perpendicular (i.e., transverse direction) to the rolling axis and C-3 main cracks grew parallel to the rolling direction. Sample C-1 had a single identifiable crack nucleation site about 200 μm from the gage surface. There was at least one more nucleating location on the edge between the gage face and hole, but it could not be identified on the fracture surface. Figure 4.38 illustrates fracture topography and the crack initiating particle for sample C-1.

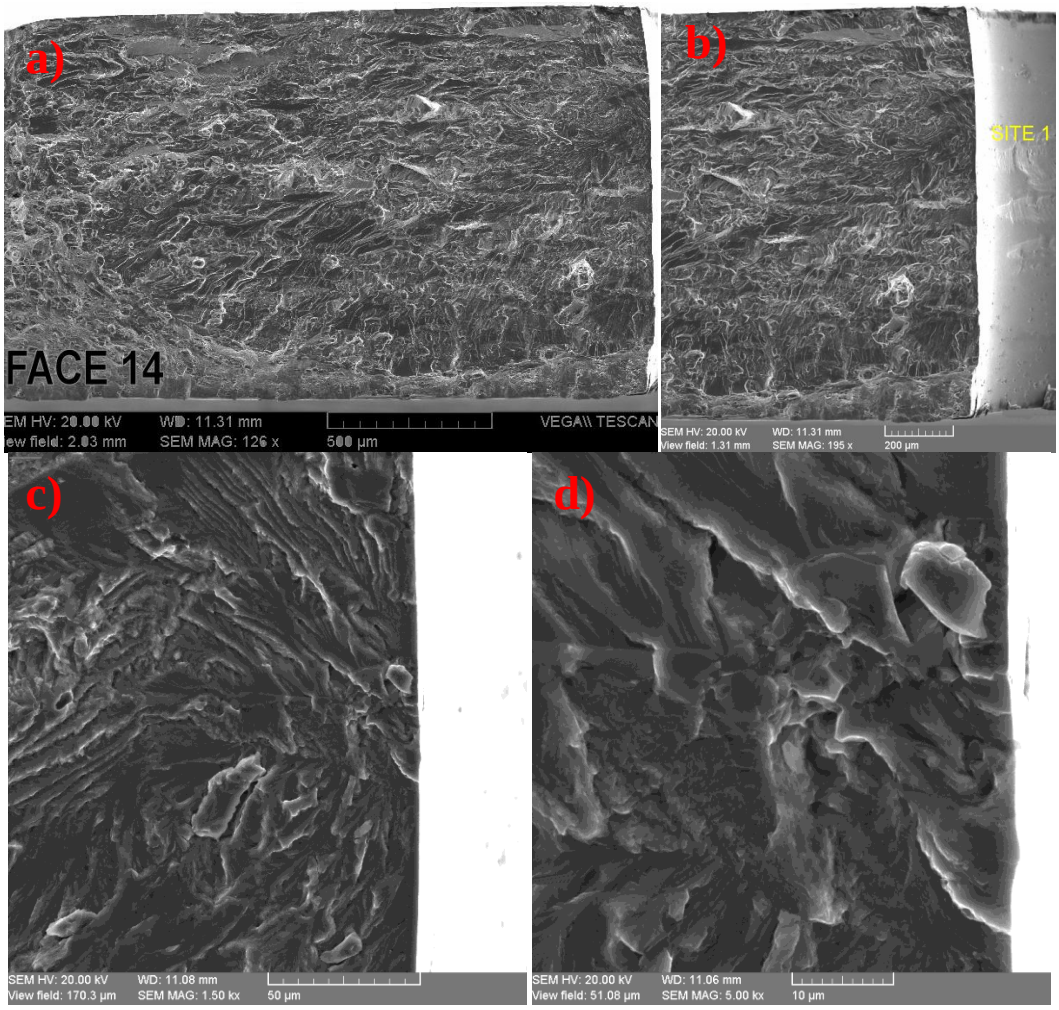

Figure 4.38: Fracture surface topography and crack initiating particle for sample C-1. Figures a and b show the fracture surface topography and figures c and d show the crack initiating particle.

Figure 4.38a closely resembles the fractographs of longitudinal samples in figure 4.24. The similarity between the fracture features can be attributed to the fact that the rolling direction is normal to the plane of the page for both longitudinal samples and C-1. There are a few instances of planar crack growth on the fracture surface. The length of planar growth is no doubt related to the grain size in the plane of the fracture surface. Assuming an elliptical grain geometry, a number of planar growth regions

were measured along the major axis parallel to the transverse direction. Average length of 289 μm was measured which is comparable to the longitudinal dogbone average of 260 μm. Planar crack growth measurements for the C-1 and dogbones correspond well to the grain measurements from EBSD scans which averaged around 314 μm. Due to environmental factors, the orientation of the C-1 fracture planes is most likely either the {100}/{110} oriented planes or plane normals between {1 0 0} and {1 1 0}. A similar conclusion was reached for the dogbones based on their fracture surface morphology and the standard stereographic triangle plot of the loading directions for the grains with crack initiation sites.

The main crack in sample C-3 grew parallel to the rolling direction. Fracture surface morphology was consistent with observations made on the fracture surfaces of transverse dogbone samples. Both C-3 and transverse dogbones exhibit long planar crack growth along preferentially oriented planes. Figure 4.39 shows the fracture surface profile of sample C-3.

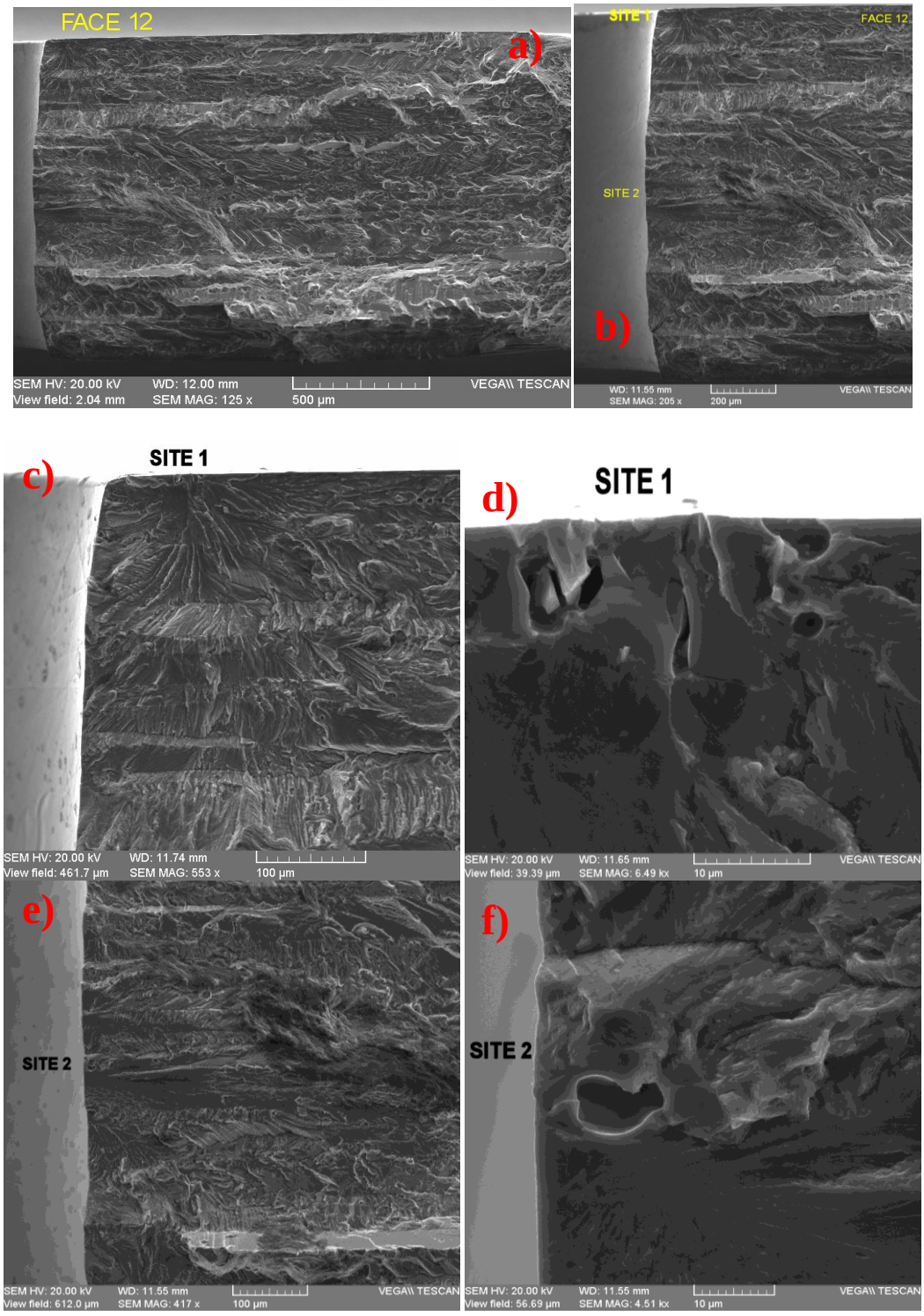

Figure 4.39: Fracture surface topography and crack initiating particles for sample C-3. Figures a and b show surface topography. Figures c,d and e,f show crack initiating particles.

As for the longitudinal samples, the length of planar fracture is congruent with the length of the elongated grains. For C-3, the average elliptical major axis length of planar fracture was about 513 μm, while it was 621 μm for the transverse dogbone samples. Measurements of grain major axis in the rolling direction from EBSD scans gives average grain length over 1 mm. The discrepancy between the fracture surface and EBSD map measurements is caused by the free surface of the cruciform and dogbone samples. The length of planar fracture is usually measured from the free surface where the grain abruptly stops due to machining. Looking at Figures 4.39 d and f, it appears that the particles themselves contain voids. It is unclear whether this is the result of cyclic testing or of thermo-mechanical processing, but the presence of voids within the particles will undoubtedly affect the load bearing properties of the particles in a negative fashion.

Stress intensity factors were calculated for the three crack nucleating locations based on figures 4.38c, 4.39c and 4.39e. Crack dimensions were obtained by measuring the length and depth of crack where the surface exhibited mainly flat growth with little to no faceting. Stress intensity calculations using weight functions along with the suggested crack dimensions are shown in Table 4.14.

Table 4.14: Stress intensity calculations for C-1 and C-3 crack at the instance when transition from stage 1 to stage 2 crack growth is believed to occur.

	a (um)	**c (um)**	**K (MPa.m$^{1/2}$)**
C-1 hole	90	90	7.6
C-3 gage face	68	68	6.6
C-3 hole	100	100	8.0

It should be noted that there is no clear defining feature on either the dogbone or cruciform fractographs that determines the end of stage 1 and the beginning of stage 2 crack regime. Rather, the outlines for the crack dimensions used in the calculations were driven by previous studies that concluded that the short crack growth regime ends when the crack is about 100 μm in length (Akiniwa and Tanaka, 1988; Newman and Edwards, 1988). Lack of fracture surface features that outline the short crack regime was also documented by Gupta and Agnew for 7000 series alloys tested in atmosphere (Gupta and Agnew, 2011). Calculations in Table 4.14 overestimate the actual stress intensity factor because constant stress was assumed across the crack face, which is not the actual case for the cruciforms since stresses decrease away from the hole. The calculated values are believed to be comparable to the actual values because finite element calculations of the stress field around the bore show small stress gradients for the length scale of the cracks used for the stress intensity calculations. Based on AGARD short crack study for 2024-T3, the crack growth data of the short crack begins to coincide with long crack data at approximately ΔK=5 MPa.m$^{1/2}$ (Newman and Edwards, 1988). Looking at the results in Table 4.14, it appears the crack

just recently made the shift from stage 1 to stage 2 crack growth behavior. Use of 2024-T3 data for the 2024-T351 discussion is acceptable due to similar crack growth rates observed for both alloys. Reported ΔK_{th} is 2.85 and 3.20 MPa.m$^{1/2}$ for Al 2024-T351 and 2024-T3, respectively (Wanhill, 1988). Moreover, it is evident that the K values in Table 4.14 are about twice as high as the reported ΔK_{th} values, which places the crack growth in the long crack regime. However, the variance in the crack growth rates in the AGARD study does not subside until about ΔK_{th}=5 MPa.m$^{1/2}$, which implies that the short crack effect is present even after the ΔK_{th} is surpassed.

4.2.4 Cruciform Crystallography Results

The EBSD maps allowed for determination of crystal directions parallel to the tensile axis in those grains where the crack initiated due to the fractured particles. Because numerous crystal directions were exposed to approximately the same stress amplitudes the outcome will be the fracture of the weakest microstructural site. Moreover, the EBSD also allowed for the examination of the overall and local texture properties of the Al 2024-T351 plate. Overall broad texture of the Al 2024-T351 shows a strong cubic texture along with a weak <111> texture in the rolling direction. Conversely the texture in the transverse direction shows a weak cubic texture and almost no <111> texture. Both orientations show no preference for {110} planes. Inverse pole figures for longitudinal and transverse directions can be seen in Figure 4.40.

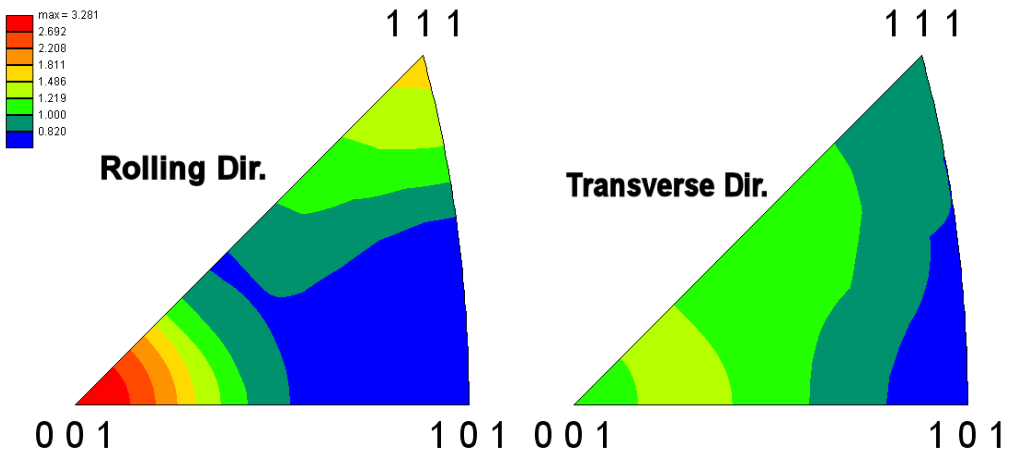

Figure 4.40: Overall texture plots for Al 2024-T351 plate.

Since small fatigue cracks are highly localized, and can be affected by the local crystallographic environment around the crack nucleation site, local texture information for the cruciforms was gathered for comparison with the texture for the overall plate. Figure 4.41 shows inverse pole figures for samples C-2 and C6.

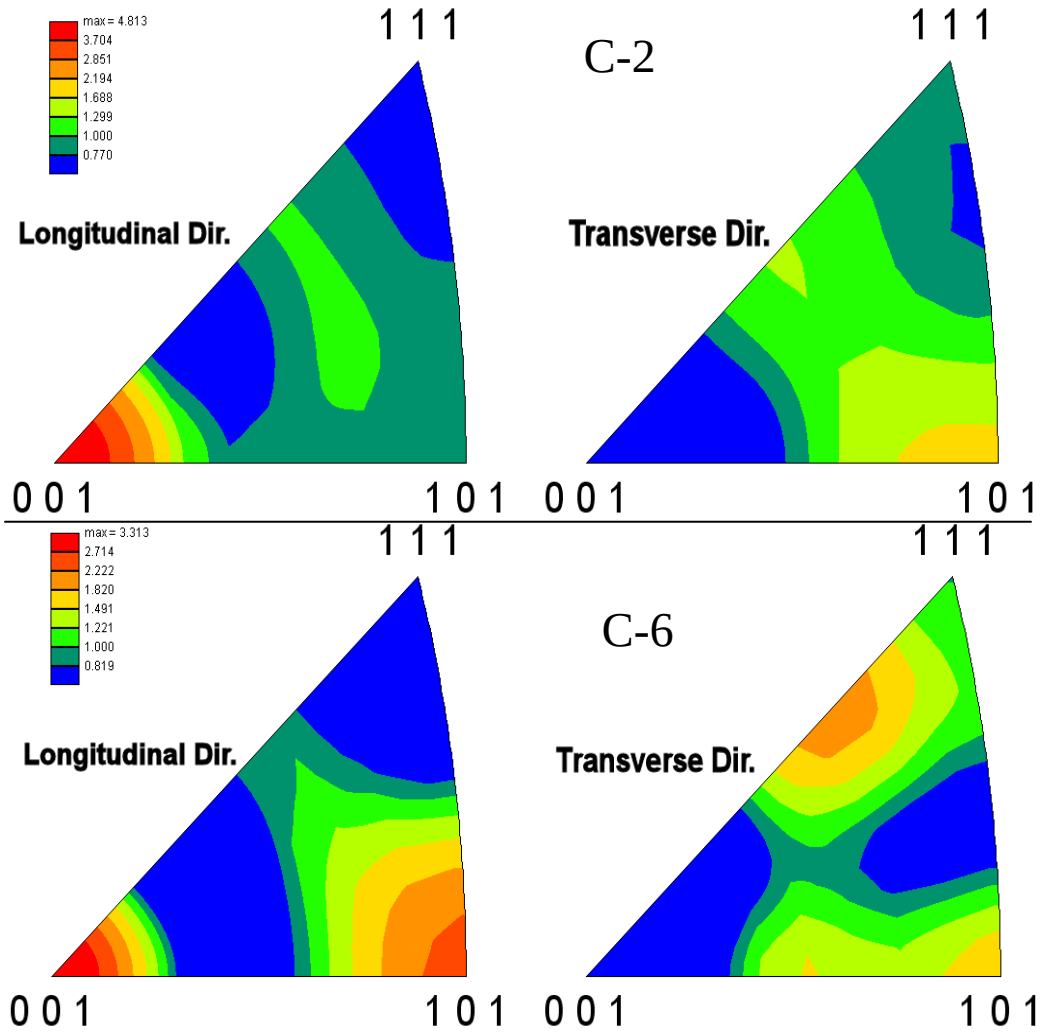

Figure 4.41: Local texture for cruciforms C-2 and C-6.

The plots in Figure 4.41 still show a strong cube texture along the longitudinal (rolling) direction but the trend between the {110} and {111} planes is reversed. Overall, inverse pole figures in Figure 4.38 show a moderate {111} texture in the longitudinal direction, the localized plots in figure 4.41 show very weak {111} texture and instead give a relatively high {110} texture. The results suggest that both the overall and local texture need to be examined in order to thoroughly understand the fracture properties of the material in the short crack regime.

Crystal directions parallel to the load direction for grains where cracks nucleated were plotted on a standard stereographic triangle including sample C-4. While cyclic testing was not completed for C-4 due to an overload, small cracks were present before the overload event. It is not clear if these cracks would have propagated to failure, but the gathered data did correspond well with the other data points gathered. Plot of the measured crystal directions can be seen in Figure 4.42 below.

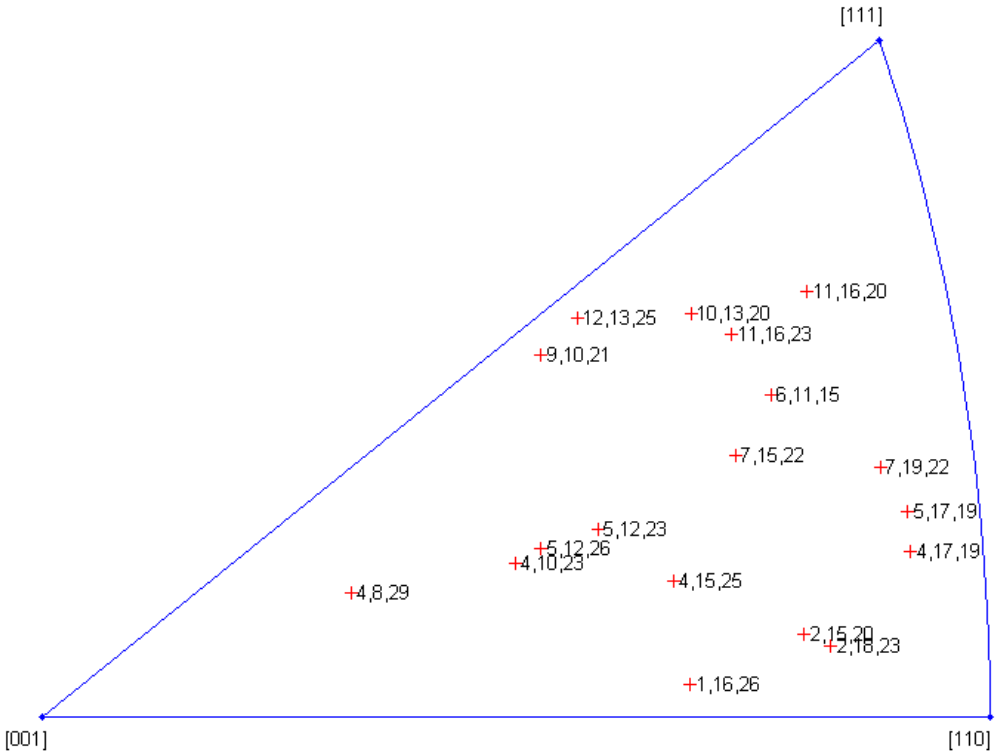

Figure 4.42: Cruciform crystal directions of fractured grains plotted on a standard triangle.

Despite the strong cubic texture of the plate no grains with crystal directions parallel to <100> were observed to contain crack initiation sites. The majority of the points are either near the <110> direction or correspond to high index axes. No double slip orientations seem to be

associated with fractured grains as was the case for the dogbone samples, where the grain orientations parallel to the load are strongly biased by the rolling texture of the samples. However, looking at Figure 4.42, directions [9 10 21] and [12 13 25] are very close to the edge of the triangle and are, therefore, close to double slip orientations. The grouping of the orientations in figure 4.42 closely resembles the standard stereographic triangle plots of fracture facet normals in figure 4.43 from studies done by Ro (2008) and Gupta and Agnew (2011).

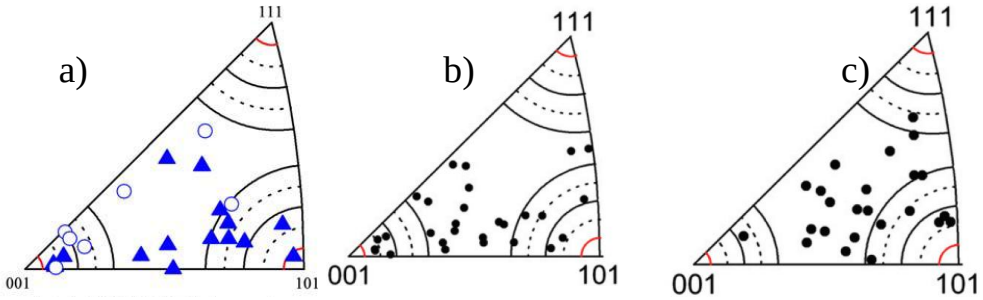

Figure 4.43: Results from literature reports on crack surface crystallography. Results plotted for Al 2024-T351 (a) from a study by Ro et. al., 2008. (b) Al 7050-T651 and (c) 7050-T7451 from a study by Gupta and Agnew, 2011.

The resulting pole groupings near <100>/<110> orientations and high index directions indicates Hydrogen embrittlement due to presence of moisture in air (Ro, 2007; Ro, 2008; Gupta and Agnew, 2011). Hydrogen embrittlement acts to effectively move fracture away from the {111} planes, which are the primary planes for fracture under ultra high vacuum conditions for fcc metals (Ro, 2007). Results gathered in figure 4.43a came from testing Al 2024-T351 in wet air, while results in figures 4.43 b and c were done in a cold dry environment for Al 7075-T651 and 7050-

T7451. The stark difference in the testing environments had no effect on the results in figure 4.43, which implies that environmental effects can only be neutralized in ultra high vacuum conditions (Gupta and Agnew, 2011). Therefore, similar fracture morphology would be expected for dogbone and cruciform samples used for this study in a “dry” air environment. While the data in figures 4.42 and 4.43 share a resemblance, the process for obtaining the crystal directions is not equivalent between this study and studies done by Ro (2008) and Gupta and Agnew (2011). In the previously mentioned studies, the actual facet normals were obtained from the fracture surfaces. For the present study, crystal directions of nucleated cracks parallel to the load were obtained on the cruciform gage surfaces. Therefore, actual facet normals were not measured. Similar comments were made regarding the crystallography data obtained for the dogbones. However, the similarity between the two data sets is significant and cannot be attributed to a random coincidence alone. A far more likely explanation is that at the instance of fracture the short crack growth follows favorably oriented crystal directions that happen to be parallel to the facet normals on the fracture surface.

Plots from Figure 4.43 show some crystal directions that near <100>,, a feature not present in Figure 4.42. However, both Figures 4.42 and 4.43 do map crystal directions near <110> and have a large fraction of high index crystal directions. Gupta and Agnew attribute the increased frequency of high index poles to distortion of {100} and {110} planes by

crack tip plasticity and inter-subgranular fracture due to trapped hydrogen in the newly formed crack surfaces (Gupta and Agnew, 2011).

In closing, cruciform fatigue lives seem to be influenced by the size of the particles as seen in Figures 4.29, 4.30. Cruciforms also, on average, experienced higher fatigue lives when compared to the dogbones, even though they were tested at stress levels comparable to those used for dogbones. The resulting increase in fatigue life (especially when compared to longitudinal samples) for the cruciforms could be attributed to the difference in the stress environment, sample geometry and macroscopic material anisotropy induced by rolling. Dogbones experience a nearly constant stress across the cross sectional area of the notch at the deepest point. On the other hand, cruciform samples posses a stress gradient in the gage area which can be seen in figures 4.35 e and f. Therefore, as the crack grows in the dogbone samples, the crack driving force can only increase as the cross sectional area is reduced. For the cruciforms samples the thickness of the gage area is constant and the crack driving force is being reduced as the crack front moves further from the hole. The reduced crack driving force effectively increases the fatigue life of the cruciforms. Like the longitudinal dogbones, cruciforms did experience multi-site crack initiation about the bore circumference. However, due to sample geometry and crack propagating directions, cracks were seldom seen to coalesce into larger cracks. More frequently, the nucleated cracks would grow parallel to each other, in most cases

coming to complete arrest and a few select carrying on till failure. In essence, the fracture process in cruciforms is closely related to transverse dogbone samples, where one main crack would nucleate and grow till failure. Moreover, lives till matrix fracture for cruciforms and transverse dogbones due to fractured particles are 78,500±22,000 and 65,000±24,000, respectively. The similarity in lives till matrix fracture is predominantly due to similar particle and grain geometries. Particle sizes for cruciforms and transverse dogbones can be seen in Table 4.15.

Table 4.15: Comparison of fractured crack nucleating particles for cruciform and transverse dogbone samples.

	Height (um)	**Width (um)**
Cruciforms	17.6±6.3	6.0±2.0
Transverse Dogbones	17.3±9.2	7.1±3.5

For the transverse sample average height calculation, a particle 65 um in length was omitted because it is seen as an extremely rare case not representative of the overall particle size distribution. Additionally, the grain morphology for cruciform samples on the bore surface would closely match to the grain geometry observed in the notches of transverse dogbone samples (Figure 4.15b). Similar fatigue response of transverse and cruciforms samples is due to a combination of similar particle and grain morphologies mainly due to macroscopic anisotropy and aided with cruciform geometry, (i.e., prevention of crack coalescence as seen in longitudinal dogbones). In fact, some transverse samples reached total lives of 150,000 and 197,000 cycles, which are fatigue lives one would expect to see for cruciform samples.

Moreover, analysis of the cruciforms revealed significant differences in plate morphology from different manufacturers that impacted the fatigue performance of the cruciform samples. Unlike the dogbone samples, which nucleated a matrix crack due to fractured and debonded particles, cruciform cracks only nucleated due to fractured particles. Both cruciform and dogbone samples posses planar crack growth evident in both longitudinal and transverse directions. For the transverse direction, fraction of planar growth was larger when compared to the longitudinal direction. The increase in grain size due to rolling would effectively guarantee larger instances of planar crack growth for the transverse orientation since the crack is growing parallel to the rolling direction. Analysis of crystal directions parallel to the load revealed pole groupings near the <110> direction and a high occurrence of high index crystal directions. Instance of high index plane fracture was attributed to plastic deformation of the crack tip and hydrogen embrittlement of the crack tip (Gupta and Agnew, 2011).

Rolling induced anisotropy affects both the particle and grain geometrical properties as well as the crystallographic texture. The influence exhibited by the rolling step acts to fundamentally change fatigue behavior for the different material directions. For particles, the induced elongation due to rolling can affect the fracture process in both a positive and negative manner. Longitudinal dogbones experienced higher instances of fractured iron bearing particles, which lead to multi-site crack

nucleation and subsequent reduction of fatigue life. Increase in particle fracture is attributed to the reduction of particle cross sectional area along with a more efficient load transfer at the particle/matrix interface due to particle orientation being parallel to the load axis. Increase in cross sectional area reduces the stress on the iron bearing particles and, therefore, a decreased frequency of particle fracture was observed in transverse dogbones. Moreover, because the particle is elongated parallel to the rolling axis, iron bearing particles deflect cracks, temporarily retarding their growth (Ref. Table 4.7 and figure 4.14). While the change in material directions yields a positive result for iron bearing particles, the same cannot be said about the softer copper-rich particles. Fracture of soft particles was almost nonexistent in longitudinal samples due to the inherent particle ductility. The increased surface area at the particle/matrix interface also insured a good mechanical bond for longitudinal samples, which prevented decohesion of the particle from the matrix. The same cannot be said for the transverse samples. Due to change in material direction, surface area at the particle/matrix interface is reduced increasing the frequency of observed decohesion incidents. Where longitudinal samples only nucleated cracks due to fractured particles, the transverse samples nucleated cracks by either fractured iron bearing particles or debonded softer Cu-rich particles. The scenario outline above shows how the global anisotropy due to rolling effectively changed material performance characteristics for the same plate.

Rolling induced anisotropy also played a significant role in the shape and size of grains present in the notches of longitudinal and transverse samples (Ref. figure 4.26). Larger grains in the longitudinal notches are more prone to bulk plasticity due to slip bands, which act to fracture particles sooner in fatigue life and also increase the crack growth rate of the short cracks (Lankford, 1982; Suresh, 1998; Gupta and Agnew; 2011). Smaller grains found in the notches of transverse sampled by default inhibit slip band formations and reduce bulk plasticity in individual grains. This acts to increase life till matrix fracture and reduces crack growth rates.

Cruciform samples propagated cracks along either longitudinal or transverse material directions. This implies that global anisotropy influenced crack growth even for cruciforms, where due to the design of the samples, failing cracks could have originated along directions different the primary plate directions. All the cruciforms tested contained some degree of crack propagation at off axes locations, but most of the time they would arrest completely. Reasons for this behavior are still unclear and further analysis needs to be carried out on the particle and grain morphologies at these locations.

Sample C-5 contained failing cracks in the longitudinal and 45 degrees to the rolling axis directions. It was determined through EBSD that both cracking locations shared similar crystal directions parallel to the load axis. This suggests that local anisotropy influenced the crack growth directions

by effectively propagating cracks along the weakest crystal directions. It was expected that since one crack grew along the longitudinal direction that the second crack would nucleate and grow on the opposing longitudinal direction as was the case for C-3 and C-6. However, this was not the case and examination of the opposing longitudinal directions found few fractured particles and no matrix crack growth. This implies that global anisotropy was not strong enough to overcome the local crystal orientations and crack simply initiated in the weakest spots where one of them was at the 45 degree diagonal. In all likelihood, crack nucleation and propagation is governed by both global and local anisotropy to varying degrees. Both phenomena compete to control the fatigue crack response and in most cases the crack nucleating sites are located where both local and global anisotropies are favorable for crack growth.

CHAPTER 5

CONCLUSIONS

A study has been carried out on Al 2024-T351 to quantify the effects of inherent material anisotropy, at the macroscopic level induced by rolling and at the local level produced by the presence of individual grains, on nucleation and propagation of short fatigue cracks. Uniaxial (dogbones) and biaxial (cruciforms) samples were used to obtain short crack data through cyclic testing, with geometry of samples chosen to study the effect of loading along different directions in the plane of the Al plate. Analysis of the data was performed using various analysis techniques that include but are not limited to scanning electron microscopy, optical microscopy and EDS/EBSD techniques. Based on the results gathered throughout the study, the following conclusions were reached.

- Testing of the dogbone samples revealed that uniaxial loading parallel to the transverse direction of the plate leads to an average fatigue life 30% higher when compared to their longitudinal counterparts, when tested at stresses equal to the corresponding yield strengths along each direction The primary reason for decreased fatigue life of longitudinal samples is the presence of multi-site cracking that effectively reduces the life of the sample due to the coalescence of a number of smaller cracks into the main failure-causing crack. Transverse samples

predominantly experienced only one crack initiation site. Crack nucleation took place by fractured particles only for the longitudinal samples where transverse samples experienced crack nucleation due to debonding as well. The presence of two crack nucleating mechanisms contributed to the increased variance in fatigue data of the transverse samples when compared to their longitudinal counterparts.

- Crack nucleation occurred only at the fractured iron bearing particles for the longitudinal samples. Conversely, cracks in the transverse samples were nucleated by either fractured iron bearing particles or debonded soft particles with high Cu content. Debonding of the softer particles suggest a weak mechanical bond in the particle/matrix interface perpendicular to the transverse direction. For the transverse samples, debonded particles nucleated cracks into the matrix earlier in fatigue life than their iron bearing counterparts. One possible reason for this outcome is the shape of the initial flaws created by either particle fracture or debonding, since the flaws created by the fractured particles were quite blunt at the particle matrix interface, which reduces the local crack driving force, compared to the sharp discontinuities created upon debonding of the softer particles.

- Trends in fatigue life versus particle size show a reducing life till matrix fracture as particle size increases for both longitudinal and transverse samples. In addition, particle iron content was measured to be 10-20% using EDS. The data indicated a decrease in fatigue life till matrix fracture as the iron content increased. During the examination, 63 and 41 fractured iron bearing particles were observed in longitudinal and transverse samples, respectively. The reduction in instance of fracture for the transverse samples is credited to the increased cross sectional area of particles in the transverse samples that acts to reduce the stress acting on the particle.
- The anisotropy in grain shape induced by rolling led to larger grains in the notch region of the longitudinal samples. Larger grains are more susceptible to dislocation slip, and this could be a contributing factor on the faster nucleation of cracks in the matrix from fractured particles in longitudinal samples when compared to the transverse samples. Additionally, increased damage due to plasticity in larger grains could serve to increase short crack growth, contributing to the reduced total fatigue life of the longitudinal samples.
- Fractographs of longitudinal and transverse samples revealed either quarter-elliptical or semi-elliptical crack shapes. Fracture surfaces for both sample orientations were comprised mainly of

faceted surfaces that suggest transgranular fracture. Instances of crystallographic fracture were also present for both sample orientations. Crystallographic fracture lengths were comparable to grain dimensions in their respective orientations with respect to the rolling axis. The fractured planes most likely belong to low index {100} or {110} planes, which are frequently observed to fracture in aluminum alloys tested in air. Plots of crystal directions parallel to the loading axis in the grains responsible for crack nucleation show planes near {110} and high index planes responsible for fracture. A few instances of double slip directions were also observed.

- Because plates from two different manufacturers were used, the cruciform samples experienced significant variance in fatigue performance. Cruciforms C-1 and C-2 were manufactured from the same plate (plate 1) and remaining cruciforms C-3 thru C-7 came from a different plate (plate 2). Fatigue lives of samples C-1 and C-2 were 25% lower when compared to the average fatigue lives of the remaining samples. Lower fatigue lives for samples C-1 and C-2 were credited to larger constituent particles and higher levels of iron in particle composition. Trends of life till matrix fracture and total fatigue lives versus particle size and iron content for cruciform samples are congruent with uniaxial sample results. Besides the difference in particle size

and iron content between the two plates, plate 1 had on average smaller grains when compared to plate 2. Due to the presence of constituent particles and the particle matrix interactions, both cruciforms and dogbone samples failed due to a combination of quasi-static and cyclic plasticity mechanisms.

- Fractography of cruciform samples show identical crack morphology and fracture surface topography as those observed on the uniaxial samples. However, unlike dogbone samples, all cruciforms cracks nucleated from iron-bearing fractured particles. The majority of cracks nucleated inside the bore near the gage face and grew across the thickness of the gage area before significant crack advance was observed across the gage face.
- Failure inducing cracks in cruciforms grew in both longitudinal and transverse directions with one instance of crack growth at 45 degrees (diagonal) to the longitudinal direction. The tendency of cracks to grow along main material directions indicates global anisotropy affects crack nucleation and growth. The instance of diagonal crack growth could be an example of local anisotropy dominance over the rolling induced anisotropy. It is believed that, in most cases, both local and global anisotropies govern the location of crack initiation. In the cruciform samples the majority of main cracks did not grow

exactly along the macroscopic material axes, rather they are rotated by some angle with respect to the L and T directions. This indicates that both local and global anisotropy factors must be favorable at the location of the nucleating crack.

- Crystal directions parallel to the load for grains that nucleated the main crack show a grouping of orientations near <110> planes and a high frequency of fracture for loading parallel to high index directions. This result was attributed to environmental effects in conjunction with crack tip plasticity that acts to distort the low index {110} and {100} planes.
- Due to the effects of anisotropy and the 3-D nature of crack propagation, any computer models developed for fatigue damage prediction purposes need to account for the 3-D nature of crack growth along with particle/matrix interactions and cyclic plasticity. Based on the fatigue performance of Al 2024-T351 in the longitudinal and transverse directions two models are recommended to aid in prediction of material response under cyclic loading. Due to multisite fracture observed for the longitudinal samples a continuous damage tolerance model is recommended because of its ability to better account for the continuous evolution of material damage due to growing and newly formed cracks. For the transverse direction, a fracture

mechanics model is more appropriate since only one crack is present and ultimately responsible for failure.

CHAPTER 6

FUTURE WORK

Based on the results gathered throughout this study, the following recommendations for future work are submitted.

In this study only 2 dogbones underwent EBSD mapping at the notch used for crack nucleation before cyclic testing. To get an actual statistical distribution of crystal directions susceptible to fracture under uniaxial load, additional samples need to undergo EBSD mapping in order to have a robust enough data set to compare to the cruciform results for any trends and dissimilarities.

Techniques for polishing dogbone and cruciform samples for EBSD quality scans have been well established throughout the experimental phase. The next step is to attempt to polish actual particles in the hopes of attaining crystal orientations within the particles that are susceptible to fracture and to study the effects, if any, of particle crystal orientations on fatigue crack nucleation of Al 2024-T351, particularly from the point of view of the average crystallographic orientations of the particles and the role that potential cleavage planes may play on their fracture under load. Early findings suggest that EBSD mapping of particles is possible because EBSD patterns were observable on some particles.

Since chemical composition of iron bearing particles has been well defined here by EDS analysis, and on other studies reported in the literature, the next step is to cast large scale billets of the reverse

engineered particle composition. The hope is to machine the billets into uniaxial test samples to acquire material properties of the particles. Previous studies have made attempts to obtain mechanical properties of the particles using micro- and nano-indentation measurements. However, estimations of mechanical properties via indentation tests are prone to large errors. By using actual uniaxial test coupons, reliable material properties will be obtained. These properties can then be used in future computer models for life predictions. Moreover, the true impact of iron content, which seems to play a role on the fatigue cracking behavior based on the EDS analysis performed here, can be studied by varying the iron content of the billets.

Throughout cyclic testing of cruciforms it became quite clear that crack nucleation and initial growth was a fully 3-D process. Therefore, it is proposed that some of the cruciforms go through serial sectioning in order to study cracking behavior in relation to the surrounding microstructure not only in one plane but through the entire thickness. Moreover, the acquired serial sections could be used to develop a 3-D computer model in hope of simulating the crack growth that was observed on the cruciform samples.

Numerous studies have been done where strain fields were studied ahead of long fatigue cracks. It is a well established fact that small fatigue cracks grow below the ΔK_{th} of long cracks. These results have raised many questions as to the validity of using the stress intensity parameter (K) in the short fatigue crack regime. In addition, researchers have

proposed that propagation of short fatigue crack is driven by the bulk plasticity in the grain surrounding the crack. Performing studies that measure strain fields around short fatigue cracks could shed some light on their fracture mechanisms and the validity of using linear elastic fracture mechanics (LEFM) in the short crack regime. Furthermore, results obtained from studying the strain fields around short cracks could be used to augment the current fracture models intended for the short crack regime. Experiments in the alloys used in this work will be benefit from the large grain size of the material, which will make it easier to perform appropriate experiments

REFERENCES

AMS standard, AMS 4037. *Aluminum Alloy, Sheet and Plate 4.4Cu - 1.5Mg - 0.60Mn (2024 -T3 Flat Sheet, -T351 Plate) Solution Heat Treated*. Aerospace Material Specification, 2003. Print.

AMS standard, AMS 4120. *Aluminum Alloy, Rolled or Cold Finished Bars, Rods, and Wire 4.4Cu - 1.5Mg - 0.60Mn (2024) Solution Heat Treated and Naturally Aged (T4) Solution Heat Treated, Cold Worked, and Naturally Aged (T351)*. Aerospace Material Specification, 2002. Print.

ASTM specification, ASTM E8-09. *Standard Test Methods for Tension Testing of Metallic Materials*. American Society of Testing Materials Standards, 2009. Print.

Akiniwa, Y., and K. Tanaka. "Statistical Characteristics of Propagation of Small Fatigue Cracks in Smooth Specimens of Aluminum Alloy 2024-T3." *Materials Science and Engineering* A104 (1988): 105-115. Print.

Bauccio, Michael. *ASM metals reference book* . 3rd ed. Materials Park, Ohio: ASM International, 1993. Print.

Bowles, C.Q., and J. Schijve. "The role of inclusions in fatigue crack initiation in an aluminum alloy." *International Journal of Fracture* 9 (1973): 171-179. Print.

Brockenbrough, J. R., R.J. Bucci, A.J. Hinkle, J. Liu, P.E. Magnusen, and S.M. Miyasato. "of microstructure on fatigue durability of aluminum aircraft alloys." *ONR Contract F33615-92-C-5915, US Office of Naval Research* (1993): Print.

Chen, D.L., and M.C. Chaturvedi. "Near-Threshold Fatigue Crack Growth Behavior of 2195 Aluminum-Lithium-Alloy Prediction of Crack Propagation Direction and Influence of Stress Ratio." *Metallurgical and Materials Transactions A* 31A (2000): 1531-1541. Print.

Cleland, W.E., and R. Prepost. "Technique for forming pressure windows from thin metal sheets." *Review of Scientific Instruments* 36 (1965): 1881-1883. Print.

De Graef, Marc, and Michael E. McHenry. *Structure of materials: an introduction to crystallography, diffraction and symmetry*. Cambridge: Cambridge University Press, 2007. Print.

DeBartolo, E.A., and B.M. Hillberry. "Effects of constituent particle clusters on fatigue behavior of 2024-T3 aluminum alloy." *International Journal of Fatigue* 20 (1998): 727-735. Print.

Donnelly, E., and D. Nelson. "A study of small crack growth in aluminum alloy 7075-T6." *International Journal of Fatigue* 24 (2002): 1175-1189. Print.

Flowes, G.R.. "Shock wave compression of hardened and annealed 2024 aluminum." *Journal of Applied Physics* 32 (1961): 1475-1487. Print.

Garrett, G.G., and J.F. Knott. "Crystallographic fatigue crack growth in aluminum alloys ." *Acta Metallurgica* 23.7 (1975): 841-848. Print.

Giuntoli, A., P.W. Bergstedt, and H.C. Turner. "Effects of aluminum alloy 4043 metal sprayed overlays on clad 2024-T3 aluminum alloy sheet on mechanical properties, corrosion properties and fatigue resistance on metals-coatings and finishes-metal spray coatings for aluminum." *General Dynamics, Pomona California, accession number AD0287620* (1959): Print.

Glinka, G. Stress and Fatigue-Fracture Design. "*Development of weight functions and computer integration procedures for calculating stress intensity factors around crack subjected to complex stress fields*."Ontario: Stress and Fatigue-Fracture Design, 1996. Progress Report No. 1.

Grandt, A.F. Jr., R. Perez, and D.E. Tritsch. "Cyclic growth and coalescence of multiple fatigue cracks." *Advances in Fracture Research, 6th International Conference on Fracture, New Delhi, India, December 1984,* Vol. 3. Pergamon Press. New York, NY, USA: 1571-1578. Print.

Grandt, A.F. Jr., A.B. Thakker, and D.E. Trisch. "An experimental and numerical investigation of the growth and coalescence of multiple fatigue cracks at notches." *Fracture Mechanics, Seventeenth Vol. ASTM STP 905. American Society for Testing and Materials,*

Philadelphia, PA, 1986 17 (1986): 239-252. Print.

Grosskreutz, J.C., and G.G. Shaw. "Mechanisms of fatigue in 1100-0 and 2024-T4 aluminum." *Air Force Materials Laboratory Technical Report AFML-TR-65-127, Wright-Patterson Air Force Base, Ohio, USA* (1965): 1-37. Print.

Grosskreutz, J.C., and G.G. Shaw. "Critical mechanisms in the development of fatigue cracks in 2024-T4 aluminum." *Proc. 2nd Int. Conf. on Fracture Brighton* (1969): 1-28. Print.

Guinier, Andrei, *X-ray diffraction in crystals, imperfect crystals, and amorphous bodies* . New York: Dover, 1994. Print.

Gupta, Vipul K., and Sean R. Agnew. "Fatigue crack surface crystallography near crack initiating particle clusters in precipitation hardened legacy and modern Al-Zn-Mg-Cu alloys." *International Journal of Fatigue* 33 (2011): 1159-1174. Print.

Hammouda, M.M., R.A. Smith, and K.J. Miller. "Elastic-Plastic frcture mechanics for initiation and propagation of notch fatigue cracks." *Fatigue and Fracture of Engineering Materials and Structures* 2.2 (1979): 139-154. Print.

Julian, Maureen M.. *Foundations of crystallography with computer applications*. Boca Raton: CRC Press, 2008. Print.

Kung, C.Y., and M.E. Fine. "Fatigue crack initiation and microcrack growth in 2024-T4 and 2124-T4 aluminum alloys." *Metallurgical transactions. A* 10A (1979): 603-610. Print.

Kusubov, A.S., and M. van Thiel. "Measurement of elastic and plastic unloading wave profile in 2024-T4 aluminum alloy." *Journal of Applied Physics* 40 (1969): 3776-3780. Print.

Lankford, J.. "The growth of small fatigue cracks in 7075-T6 aluminum." *Fatigue of Engineering Materials and Structures* 5 (1982): 233-248. Print.

Lankford, J.. "The influence of microstructure on the growth of small fatigue cracks." *Fatigue & Fracture of Engineering Materials & Structures* 8 (1985): 161-175. Print.

Laz, P.J., and B.M. Hillberry. "Fatigue life prediction from inclusion initiated cracks." *International Journal of Fatigue* 20 (1998): 263-270. Print.

Li, Jinxia. *The effect of microstructure and texture on high cycle fatigue properties of Al alloys*. Diss. University of Kentucky, 2007. Print.

Liao, Min, Guillaume Renaud, and Nick Bellinger. "Probabilistic Modeling of Short-Crack Growth in Airframe Aluminum Alloys." *Journal of Aircraft* 45 (2008): 1105-1111. Print.

Liao, Min. "Probabilistic modeling of fatigue related microstructural parameters in aluminum alloys." *Engineering Fracture Mechanics* 76 (2009): 668-680. Print.

Liao, Min. "Dislocation theory based short crack model and its application for aircraft aluminum alloys." *Engineering Fracture Mechanics* 77 (2010): 22-36. Print.

Liu, A.F., J.E. Allison, D.F. Dittmer, and J.R. Yamane. "Effect of biaxial stresses on crack growth." *Fracture Mechanics, ASTM STP 677, C.W. Smith, Ed., American Society for Testing and Materials* 1 (1979): 5-22. Print.

Magnusen, P.E., R.J. Bucci, A.J. Hinkle, J.R. Brockenbrough, and H.J. Konish. "Analysis and prediction of microstructural effects on long-term fatigue performance of an aluminum aerospace alloy." *International Journal of Fatigue* 19 (1997): 275-283. Print.

Maymon, G.. "Probabilistic crack growth behavior of aluminum 2024-T351 alloy using the “unified” approach." *International Journal of Fatigue* 27 (2005): 828-834. Print.

Maymon, G.. "A "unified" and a $(\Delta K^* K_{max})^{1/2}$ crack growth models for aluminum 2024-T351." *International Journal of Fatigue* 27 (2005): 629-638. Print.

Merati, Ali. "A study of nucleation and fatigue behavior of an aerospace aluminum alloy 2024-T3." *International Journal of Fatigue* 27 (2004): 33-44. Print.

Merati, Ali, and Graeme Eastaugh. "Determination of fatigue related discontinuity state of 7000 series of aerospace aluminum alloys."

Engineering Failure Analysis 14 (2007): 673-685. Print.

"MIL-HDBK-5H." *Metallic Materials and Elements for Aerospace Vehicle Structures*. Department of Defense, 1998. 67-149. Print.

Morris, W.L., O. Buck, and H.L. Marcus. "Fatigue crack initiation and early propagation in Al 2219-T851." *Metallurgical Transactions A* 7A (1976): 1161-1165. Print.

Murakami, Y.. *Stress Intensity Factor Handbook, vol. 1*. New York: Pergamon Press, 1987. Print.

Newman, J.C., and P.R. Edwards. "Short crack growth behavior in an aluminum alloy." *an AGARD Cooperative test programme. AGARD-R-767, North Atlantic Treaty Organization (NATO)*, (1988): Print.

Nix, K.J., and H.M. Flower. "The micromechanisms of fatigue crack growth in a commercial Al-Zn-Mg-Cu alloy ." *Acta Metallurgica* 30.8 (1982): 1549-1559. Print.

Patton, G., C. Rinaldi, Y. Brechet, G. Lormand, and R. Fougeres. "Study of fatigue damage in 7010 aluminum alloy." *Materials Science and Engineering* A254 (1998): 207-218. Print.

Payne, Joel, Greg Welsh, Robert J. Christ Jr., Jerrell Nardiello, and John M. Papazian. "Observations of fatigue crack initiation in 7075-T651." *International Journal of Fatigue* 32 (2010): 247-255. Print.

Pearson, S.. "Initiation of fatigue cracks in commercial aluminum alloys and the subsequent propagation of very short cracks." *Engineering Fracture Mechanics* 7 (1975): 235-247. Print.

Peralta, Pedro. *Scanning Electron Microscopy and Automated Orientation Mapping" Techniques for Materials Characterization*. January 2008, PowerPoint, Print.

Properties and selection: Nonferrous alloys and special-purpose materials. 10th ed. Metals Park, Ohio: ASM International, 1990. Print.

Ro, Yunjo, Sean R. Agnew, and Richard P. Gangloff. "Crystallography of

Fatigue Crack Propagation in Precipitation-Hardened Al-Cu-Mg/Li." *Metallurgical and Materials Transactions A* 38A (2007): 3042-3062. Print.

Ro, Yunjo, Sean R. Agnew, and Richard P. Gangloff. "Environmental Fatigue-Crack Surface Crystallography for Al-Zn-Cu-Mg-Mn/Zr." *Metallurgical and Materials Transactions A* 39A (2008): 1449-1465. Print.

Sands, Donald. *Introduction to crystallography* . New York: Dover, 1993. Print.

Schijve, J., and F.A. Jacobs. "Fatigue crack propagation in unnotched and notched aluminum alloy specimens." *NLR TR M2128, Natn. Aeronaut Res. Inst, Amsterdam* (1965): 1-40. Print.

Schwartz, Adam J., Mukul Kumar, and B. L. Adams. *Electron backscatter diffraction in materials science*. New York: Kluwer Academic, 2000. Print.

Staley, J.T.. "How Microstructure affects fatigue and fracture of aluminum alloys." *Symposium on Naval Structural Mechanics (10th; 1978; Washington),* (1978): 671-684. Print.

Suresh, S.. *Fatigue of materials*. 2nd ed. Cambridge: Cambridge University Press, 1998. Print.

Swanson, S.R.. "Systematic axial load fatigue tests using un-notched aluminum alloy 2024-T4 extruded bar specimens." *Toronto Univ (Ontario) Inst for aerospace studies, Accession number AD0258552* (1960): Print.

Tanaka, K., and T. Mura. "A theory of fatigue crack initiation at inclusions." *Metallurgical Transactions A* 13A (1982): 117-123. Print.

Tanaka, K., Y. Akinawa, Y. Kakai, and R.P. Wei. "Modeling of small fatigue crack growth interacting with grain boundary." *Engineering Fracture Mechanics* 24.6 (1986): 803-819. Print.

Tanaka, K., M. Kinefuchi, and T. Yokomaku. "Modeling of statistical characteristics of the propagation of small fatigue cracks." *In: Miller K.J., de los Rois E.R., editors. Short fatigue cracks, ESIS* vol. 13.

London: Mechanical Engineering Publications (1992): 351-368. Print.

Teale, Rikki Lynn. *Effects of microstructural and mechanical length scales on stage II fatigue crack growth on aluminum 2024*. MS thesis, Arizona State University, 2009. Print.

Wanhill, R.J.H.. "Low Stress Intnesity Fatigue Crack Growth in 2024-T3 and T351." *Engineering Fracture Mechanics* 30.2 (1988): 233-260. Print.

Weiland, H., J. Nardiello, S. Zaefferer, S. Cheong, J. Papazian, and Dierk Raabe. "Microstructural aspects of crack nucleation during cyclic loading of AA7075-T651." *Engineering Fracture Mechanics* 76 (2009): 709-714. Print.

Wu, X.J., W. Wallace, M.D. Raizenne, and A.K. Koul. "The orientation dependance of fatigue-crack growth in 8090 Al-Li plate." *Metallurgical and Materials Transactions A* 25A (1994): 575-588. Print.

Xue, Y., H. El Kadiri, M.F. Horstemeyer, J.B. Jordon, and H. Weiland. "Micromechanisms of multistage fatigue crack growth in a high-strength aluminum alloy." *Acta Materalia* 55 (2007): 1975-1984. Print.

Yokobori, T., H. Kuribayashi, and T. Takechi. "Studies on the initiation and propagation of fatigue crack in tempered martensitic high strength steel by plastic replication method and scanning electron microscope." *Rep. of Inst. for Strength and Fracture of Mater* 7 (1971): Print.

Yuanbin, Zhang, Xu Jianhui, and Zhai Tongguang. "Distributions of pore size and fatigue weak link strength in an A713 sand cast aluminum alloy." *Materials Science and Engineering A* 527 (2010): 3639-3644. Print.

Zabett, A., and A. Plumtree. "Microstructural effects on the small fatigue crack behavior of an aluminum alloy plate." *Fatigue & Fracture of Engineering Materials & Structures* 18 (1995): 801-809. Print.

Zhai, T., A.J. Wilkinson, and J.W. Martin. "A crystallographic mechanism

for fatigue cracks propagation through grain boundaries." *Acta Materalia* 48 (2000): 4917-4927. Print.

Zhai, T., X.P. Jiang, J.X. Li, M.D. Garratt, and G.H. Bray. "The grain boundary geometry for optimum resistance to growth of short fatigue cracks in high strength Al-alloys." *International Journal of Fatigue* 27 (2005): 1202-1209. Print.

Zhai, T.. "Strength Distribution of Fatigue Crack Initiation Sites in an Al-Li Alloy." *Metallurgical and Materials Transactions A* 37A (2006): 3139-3147. Print.

Zhang, Yuanbin, Jianhui Xu, and Tongguang Zhai. "Distributions of pore size and fatigue weak link strength in an A713 sand cast aluminum alloy." *Materials Science and Engineering A* 527 (2010): 3639-3644. Print.

Zheng, Z.Q., B. Cai, T. Zhai, and S.C. Li. "The behavior of fatigue crack initiation and propagation in AA2524-T34 alloy." *Materials Science and Engineering A* 528 (2011): 2017-2022. Print.

Zurek, A.K., M.R. James, and W.L. Morris. "The effect of grain size on fatigue growth of short cracks." *Metallurgical Transactions A* 14A (1983): 1697-1705. Print